5-2017

Characterization of Plastic Deformation Evolution in Single Crystal and Nanocrystalline Cu During Shock by Atomistic Simulations

Mehrdad Mirzaei Sichani
University of Arkansas, Fayetteville

Characterization of Plastic Deformation Evolution in Single Crystal and Nanocrystalline Cu During Shock by Atomistic Simulations

A dissertation submitted in partial fulfillment
of the requirements for the degree of
Doctor of Philosophy in Engineering

by

Mehrdad Mirzaei Sichani
Azad University
Bachelor of Science in Mechanical Engineering, 2005
Shiraz University
Master of Science in Mechanical Engineering, 2008

May 2017
University of Arkansas

This dissertation is approved for recommendation to the Graduate Council.

Dr. Douglas E. Spearot
Dissertation Director

Dr. Paul Millett
Committee Member

Dr. Min Zou
Committee Member

Dr. Arun Nair
Committee Member

Dr. Salvador Barraza-Lopez
Committee Member

Abstract

The objective of this dissertation is to characterize the evolution of plastic deformation mechanisms in single crystal and nanocrystalline Cu models during shock by atomistic simulations. Molecular dynamics (MD) simulations are performed for a range of particle velocities from 0.5 to 1.7 km/s and initial temperatures of 5, 300 and 600 K for single crystal models as well as particle velocities from 1.5 to 3.4 km/s for nanocrystalline models with grain diameters of 6, 11, 16 and 26 nm. For single crystal models, four different shock directions are selected, <100>, <110>, <111> and <321>, and dislocation density behind the shock wave front generally increases with increasing particle velocity for all shock orientations. Plastic relaxation for shock in the <110>, <111> and <321> directions is primarily due to a reduction in the Shockley partial dislocation density. In contrast, plastic relaxation is limited for shock in the <100> orientation. This is partially due to the emergence of sessile stair-rod dislocations with Burgers vectors of 1/3<100> and 1/6<110> due to the reaction of Shockley partial dislocations with twin boundaries and stacking fault intersections. For <100> shock, FCC Cu is uniaxially compressed towards the BCC structure behind the shock wave front; this process is more favorable at higher shock pressures and temperatures. For particle velocities above 0.9 km/s, regions of HCP crystal structure nucleate from uniaxially compressed Cu. Free energy calculations proves that the nucleation and growth of these HCP clusters are an artifact of the embedded-atom interatomic potential. In addition, simulated x-ray diffraction line profiles are created for <100> shock models of single crystal Cu at the Hugoniot state. Generally, peak broadening in the x-ray diffraction line profiles increases with increasing particle velocity. For nanocrystalline models, the compression of the FCC lattice towards the BCC structure is more apparent at particle velocity of 2.4 km/s, and at this particle velocity, the atomic percentage of BCC structure increases with increasing grain size. The observation of BCC structure strongly

depends on grain orientation; grains with <100> directions closely aligned with the shock loading direction show a higher percentage of BCC structure.

Dedication

To My Family

&

The Best Friends

Table of Contents

List of Figures

List of Tables

List of Published Papers

Chapter 3 Mehrdad M. Sichani and Douglas E. Spearot (2016) A Molecular Dynamics Study of Dislocation Density Generation and Plastic Relaxation during Shock of Single Crystal Cu, Journal of Applied Physics, **120** 045902.

Chapter 5 Mehrdad M. Sichani and Douglas E. Spearot (2015) A Molecular Dynamics Study of the Role of Grain Size and Orientation on Compression of Nanocrystalline Cu during Shock, Computational Materials Science, **108** 226-232.

Chapter 6 A part of Chapter 6 is extracted from the research paper (the detail is below) which was collaborative with Shawn P. Coleman, but this part was done by the author of this dissertation.
Shawn P. Coleman, Mehrdad M. Sichani and Douglas E. Spearot (2014) A Computational Algorithm to Produce Virtual X-ray and Electron Diffraction Patterns from Atomistic Simulations, JOM, **66** 408-416.

Chapter 1: Introduction

1.1 Motivation

Shock in solid materials includes a dynamic change in the state of stress, and sometimes mechanical properties, usually due to a high velocity collision of two or more bodies, resulting high strain rates inside the material. Shock in solid materials appears in several situations, including high velocity impacts of air planes and automobiles [1], explosive welding in metals [2], penetration of armor [3,4] and asteroid collisions [5,6]. Under these high strain rates, there are some unique deformation behaviors, which are completely different than those under low strain rates. For example, Bringa et al. [7] reported an enhanced strength of nanocrystalline Cu behind the shock wave front, which is up to twice the strength of nanocrystalline Cu subjected to low strain rates. In addition, several researchers used shock waves in solid materials to obtain equation of state at extreme conditions of high temperatures and pressures [8–10].

The motivation for this research is to understand the plastic behavior of solid FCC metallic materials subjected to shock. There are a tremendous amount of experimental [11–14], numerical [15–18] and analytical [11,19–21] studies of plastic deformation in shocked metallic materials. However, only a few of these studies [22–24] explored the plastic deformation evolution of microstructure behind the shock wave front quantitatively. To provide more quantitative insights, this research uses atomistic simulations to characterize the evolution of plastic deformation mechanisms, including dislocation density and phase transformation, behind the shock wave front of single crystal and nanocrystalline Cu. This quantitative analysis helps us to understand the nature of plastic deformations in shocked metallic FCC materials with nanosecond (ns) time scale and nanometer (nm) length scale resolution.

Non-equilibrium molecular dynamics (NEMD) simulation is a powerful tool to study martensitic (diffusionless) phase transformations and dislocation generation in shocked single crystal [25,26] and nanocrystalline [27,28] metallic materials with nm length scale and ns time scale resolution. The time scale and length scale of MD simulations are perfectly appropriate to analyze the plastic deformation phenomena at the atomic level, including dislocation nucleation/propagation, twinning, stacking faults and phase transformations quantitatively, which is challenging in experimental studies with longer time scale and larger length scales. Thus, NEMD simulations with the aid of computational characterization methods, such as the centrosymmetry parameter [29], the common neighbor analysis (CNA) [30] and the dislocation extraction algorithm (DXA) [31] are necessary to predict the plastic behavior of metallic materials during shock.

1.2 Shock in Solid Materials

Several experimental techniques are used to induce shock waves inside solid materials, including plate impact [32,33] and pulsed laser loading [34,35]. The plate impact is a traditional method to produce strain rates up to 10^6 1/s. However, to reach the strain rates up to 10^{10} 1/s, the pulsed laser loading method is performed to create shock waves in solid materials. Figures 1.1 and 1.2 show schematics of typical experimental setups for plate impact and pulsed laser loading, respectively. Basically, a plate impact set up includes a projectile (or piston) to hit the target material (Figure 1.1) and induce a shock wave inside the target. Instead, laser beams are used to create shock waves inside the target in pulsed laser loading setups, which is shown in Figure 1.2.

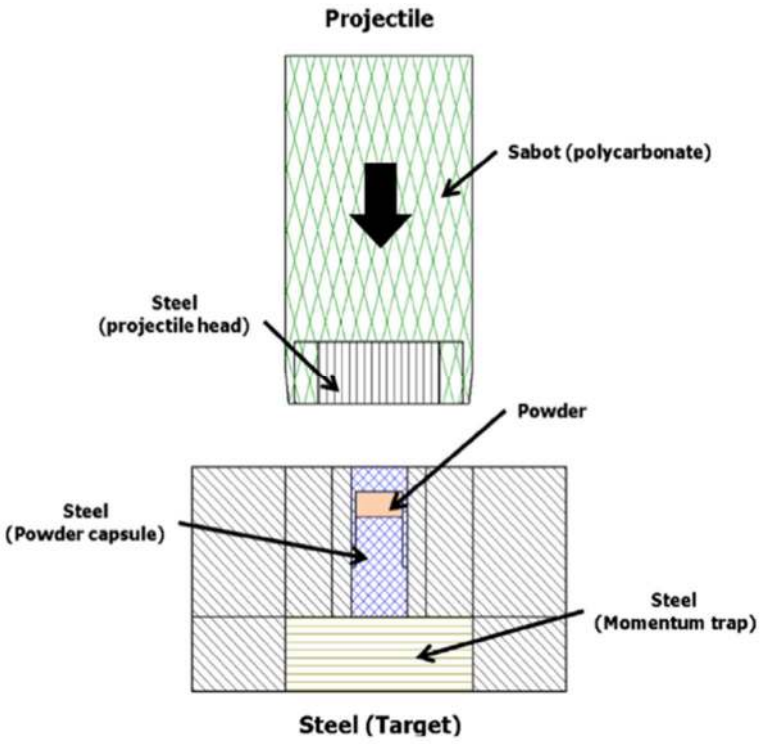

Figure 1.1: Schematic of experimental shock setup for plate impact [32].

Even though these experimental methods are powerful tools to investigate the macroscopic mechanical properties, such as the dynamic strength of shocked materials [32], the spall strength [36], the shock Hugoniot [8], etc., evaluating the microscopic mechanical properties and deformation mechanisms is challenging at high strain rates (and thus short time scales). For example, to calculate the dislocation density behind the shock wave front, experimental researchers have to recover the shocked sample, which results in the relaxation of a fraction of dislocations [22]. MD simulation is an excellent tool to characterize the microscopic mechanical properties of solid materials subjected to shock in atomic level and strain rates well above 10^6 1/s.

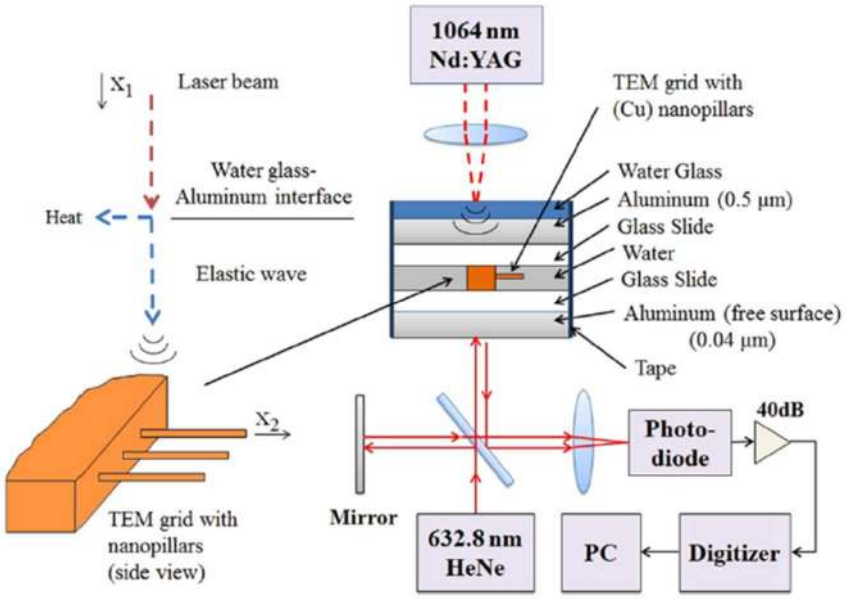

Figure 1.2: Schematic of experimental shock setup for pulsed laser loading [35].

When a metallic material is subjected to shock above a certain shock strength, dislocations and other defects nucleate and propagate inside the compressed material. Holian and Lomdahl [15] investigated plasticity in <100> shock of single crystals using MD simulations and Lennard-Jones interatomic potentials. They observed the nucleation of Shockley partial dislocations on all {111} close-packed planes, leading to the formation of stacking faults with an intersecting pattern, which is shown in Figure 1.3. They reported that the nucleation of Shockley partial dislocations and formation of stacking faults is not influenced by the periodic boundary conditions in MD simulations, above a certain critical size. They also obtained the Hugoniot curve (the relationship between the shock velocity and the particle velocity) for a range of particle velocities above the Hugoniot elastic limit (HEL), above which generation of dislocations and other defects is observed.

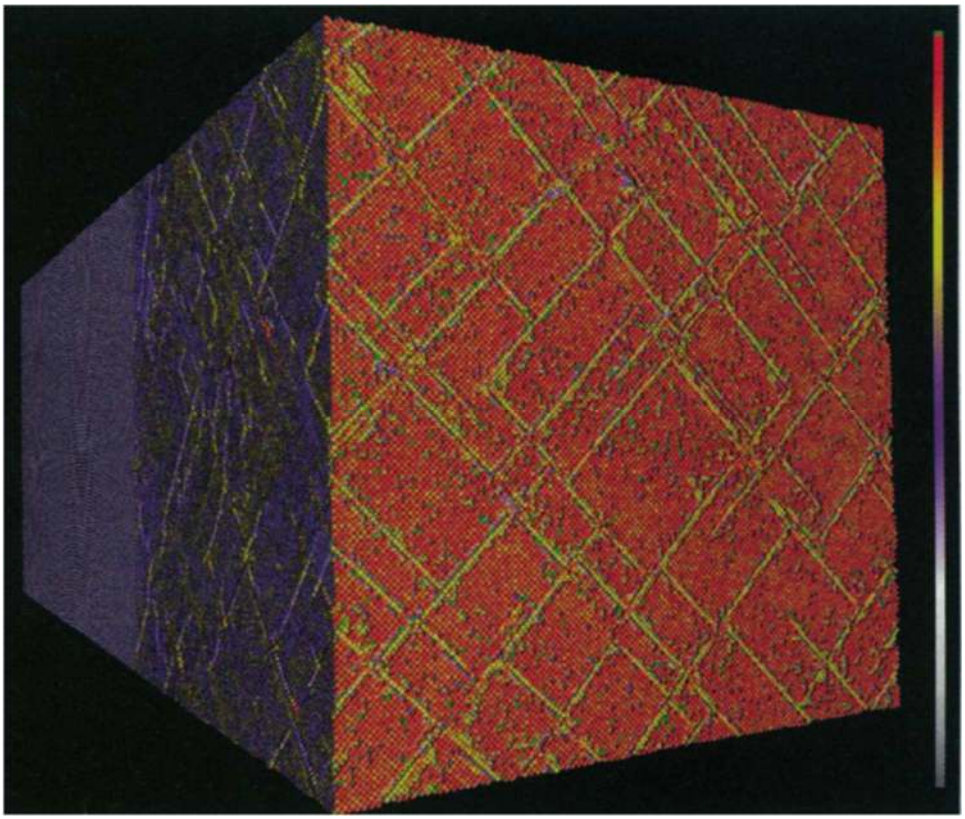

Figure 1.3: Formation of stacking faults with intersecting pattern for a FCC single crystal during <100> shock colored by potential energy [15].

To explore the role of crystallographic orientation of FCC single crystals on plastic deformation, Germann et al. [16,26], using MD simulations, investigated shock wave propagation in <100>, <110> and <111> orientations of FCC crystals, and reported elastic precursor in <110> and <111> shock loading directions. In addition, they reported Shockley partial dislocation loops and perfect dislocation loops for shock in <100> and <111> directions, respectively. In <110> shock loading, they also observed a shuffle-type martensitic transformation near the impact surface. Regarding the conditions for propagation of Shockley partial dislocation loops behind the shock wave front during <100> shock of FCC single crystals,

Tanguy et al. [37,38] found that loops are nucleated by thermal fluctuations, and obtained a critical loop size above which the loop can expand.

Dislocation density calculation is required to quantify plastic deformation behind the shock wave front. Several experimental [13,39] and analytical [11,40] studies have been conducted to obtain dislocation density behind the shock wave front of metallic materials along specific crystallographic directions. However, there are some experimental challenges regarding accurate calculation of dislocation density behind the shock wave front. For example, Bringa et al. [22] reported that a fraction of the dislocations will be relaxed due to the tension waves at the free surfaces and during the recovery process. Therefore, simulations are necessary to obtain more accurate dislocation density magnitudes behind the shock wave front. Bringa et al. [22] used extremely large MD simulations (up to 352 million atoms) and employed a centrosymmetry-based method to calculate dislocation density behind the <100> shock wave front of single crystal Cu. They performed simulations at a single particle velocity of 0.75 km/s for two samples with preexisting dislocation sources (one sample with zero rise time loading and another with ramp loading) to calculate dislocation density behind the shock front.

Shehadeh et al. [23], using multiscale dislocation dynamics plasticity (MDDP) simulations, calculated dislocation density behind the shock wave front of single crystal Cu in <100>, <110> and <111> directions including preexisting dislocation sources (heterogeneous nucleation). They reported dislocation density magnitudes for these three shock loading direction at a peak shock pressure of 5 GPa and extended the range of shock pressure up to 100 GPa only for <100> shock. In another study, Shehadeh et al. [24], using MDDP simulations, calculated dislocation density behind the <100> shock wave front of single crystal Cu including homogeneous

dislocation sources. They reported dislocation density magnitudes for the pressure range between 30 and 70 GPa and compared their results with multimillion atom MD simulation data, where the dislocation densities were calculated by the centrosymmetry-based method developed by Bringa et al. [22]. Figure 1.4 compares the dislocation density values based on MD and DD simulations and analytical calculations for <100> shock of single crystal Cu. However, the dependence of dislocation density behind the shock wave front of FCC single crystals on particle velocity and lattice orientation within the time scales and length scales of MD simulations has not been explored yet, which is one of the objectives of this dissertation.

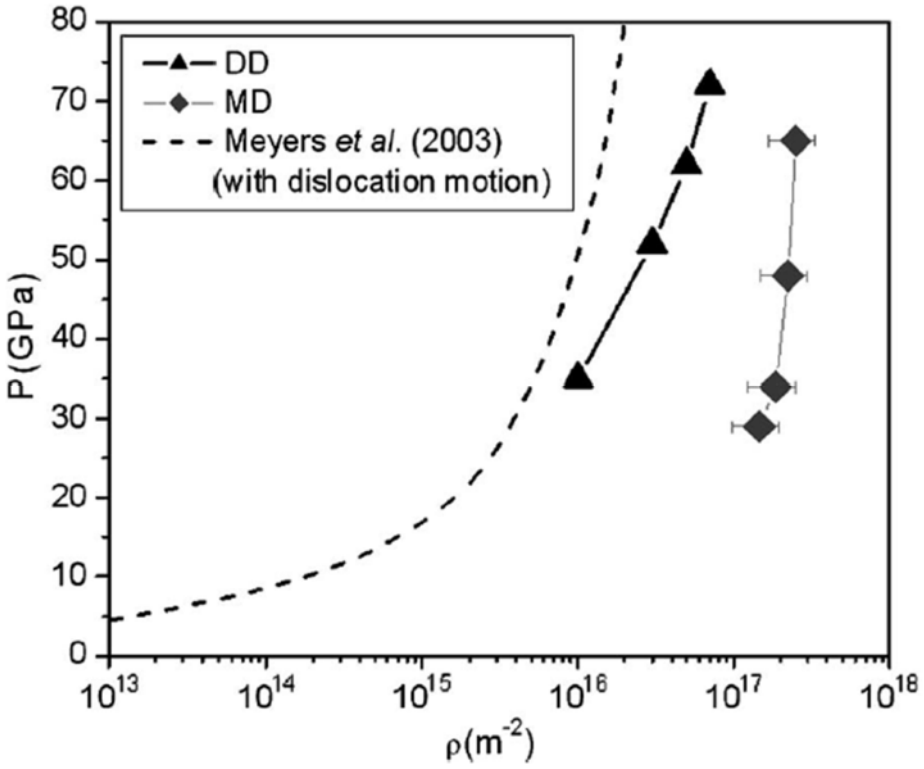

Figure 1.4: Dislocation density values based on MD and DD simulations and analytical calculations for <100> shock of single crystal Cu [24].

The terms “Hugoniot state” and “Hugoniot curve” are used above and extensively used to describe shock studies throughout this dissertation; thus, clear definitions for the application of these terms are necessary. After the propagation of the leading edge of a shock wave through a sample, the temperature and pressure within the sample evolve to reach equilibrium values. The Hugoniot state represents the thermal and mechanical equilibrium of a sample subjected to shock [41]. The evolution of the temperature and pressure of a nanocrystalline Cu model subjected to shock reaching to the Hugoniot state will be shown in Chapter 5. The Hugoniot curve is the relationship between the shock wave velocity (u_s) and particle velocity (u_p). After applying the conservation of mass, momentum and energy at the shock front, the relationship between the shock wave velocity and the particle velocity is obtained, $u_s = u_p/\varepsilon$, where ε is the volumetric compressive strain [42]. For the strong shocks, when the plastic wave overdrives the elastic wave, the Hugoniot curve is typically in the form of $u_s = u_0 + s_1 u_p$, where s_1 is a constant and u_0 is the bulk speed of sound [42]. More details regarding the calculation and validation of the Hugoniot curve via atomistic simulations for shock of single crystal Cu in <100>, <110>, <111> and <321> shock loading directions will be presented in Chapter 3. In addition, the term “Hugoniot curve” sometimes is used to represent the relationship between the temperature and pressure of sample at the Hugoniot state, which will be shown in Chapter 5 for several shocked nanocrystalline Cu models.

There are two plastic regimes behind the shock wave front of metallic materials: (1) nucleation/propagation of dislocations and other defects and (2) plastic relaxation as the system reaches the hydrostatic state of stress. Some experiments, using time-resolved x-ray diffraction method, have been conducted to investigate the lattice response behind the shock wave front of single crystals [43,44]. For example, Loveridge-Smith et al. [43] reported a fast plastic relaxation

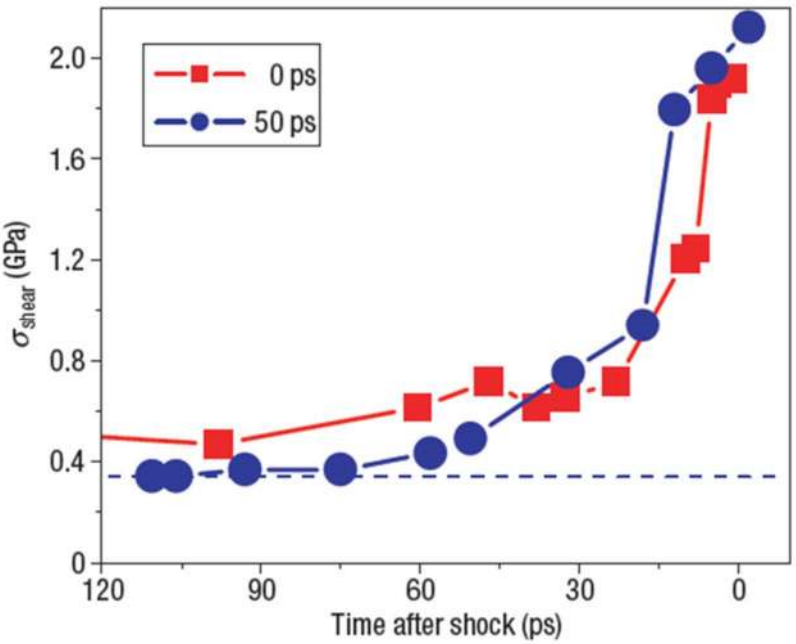

Figure 1.5: Plastic relaxation regime for a single crystal Cu during <100> shock [22]. The shear stress reaches a nonzero asymptotic value less than 100 ps. Red points are associated with zero time loading condition, and blue points are associated with ramp loading condition.

for Cu, which took less than 100 ps. Using simulated x-ray diffraction method based on MD simulations, Rosolankova [45] reported a predominant uniaxial compression (1D) behind the shock wave front of FCC single crystals. To resolve this dilemma, Bringa et al. [22], using extremely large MD simulations (up to 352 million atoms), performed <100> shock simulations for single crystal Cu. These large simulations provided sufficient time for plastic relaxation behind the shock front. They found the mobile dislocation density behind the shock front initially increases; then, during the plastic relaxation regime, both the mobile dislocation density and the dislocation velocity decrease as the system approximately reaches the hydrostatic state of stress (the Hugoniot equilibrium state). They reported the plastic relaxation regime takes less than 100

ps, which was in agreement with the MDDP simulation result [24]. Figure 1.5 shows the evolution of shear stress for this reported plastic relaxation regime [22]. The approach developed by Bringa et al. [22] to study the plastic relaxation regime needs a very large model to provide a sufficient time for plastic relaxation. In addition, they only studied the plastic relaxation regime in <100> shock at a single particle velocity of 0.75 km/s. The characterization of the plastic relaxation regime behind the shock front of single crystal Cu in <100>, <110>, <111> and <321> directions and for particle velocities range from the HEL to 1.5 km/s is another objective of this dissertation. Furthermore, to avoid extremely large MD simulations, an absorbing wall boundary condition [46] is used in this work.

Beside MD studies of dislocation nucleation/propagation and plastic relaxation behind the shock wave front of metallic materials, there are several studies to investigate solid-liquid [47–49] and martensitic (diffusionless) [17,18,27] phase transformation behind the shock front. An example of solid-liquid phase transformation is work reported by He et al. [41]. They studied bulk and dynamic local melting of shocked nanocrystalline Cu with hexagonal shaped grains. They reported that even though the Hugoniot state and the bulk melting are independent of shock loading direction, the local melting is an anisotropic phenomenon due to mechanisms including premelting, superheating, supercooling and recrystallization. As an another example, Levitas and Ravelo [50] proposed virtual melting as a relaxation mechanism during a state of high shear stresses to explain observations of melting in shocked Cu samples at temperatures below the expected melting temperature at a given shock pressure.

MD simulation method is a powerful tool to study martensitic phase transformation in shocked single crystal [17,18,25] and nanocrystalline [27,28,51] metallic materials with nm

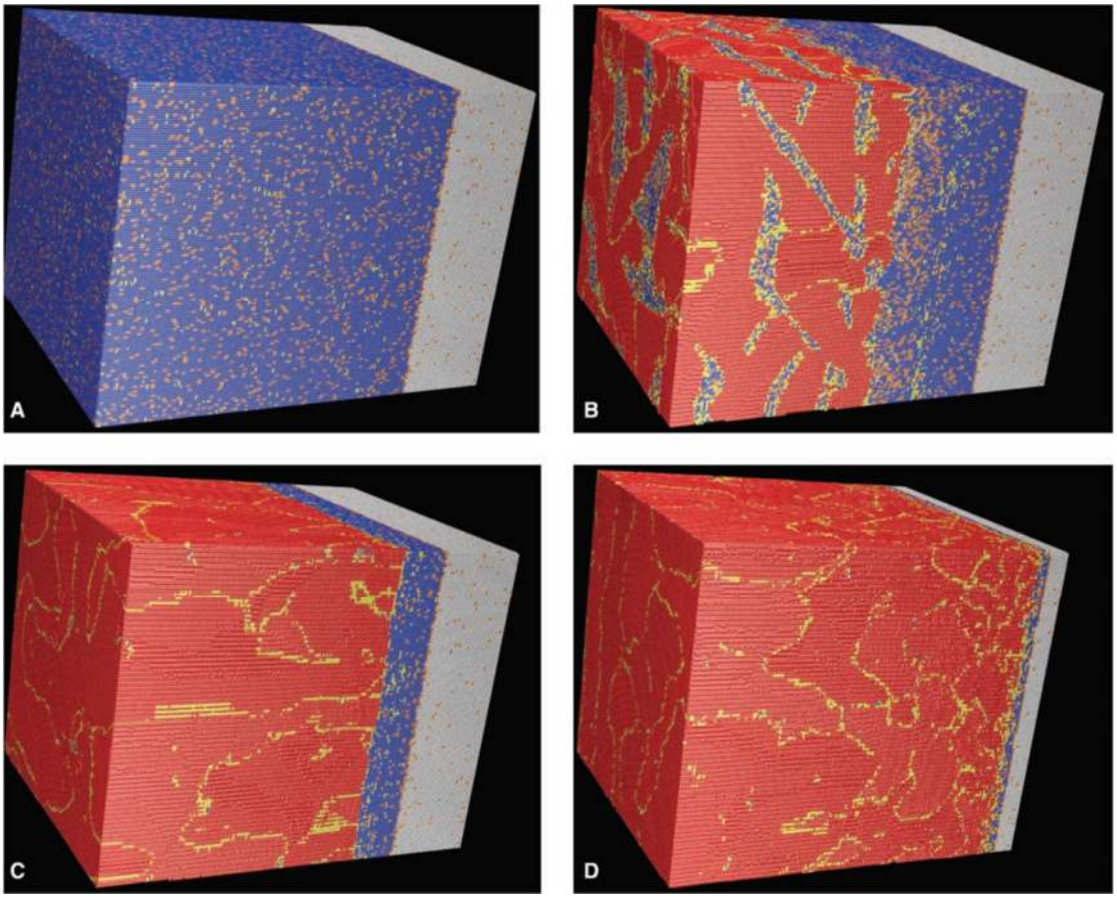

Figure 1.6: Martensitic phase transformation for a single crystal Fe subjected to <100> shock at 8.76 ps after loading [25]. Figures (A)-(D) are associated with particle velocities of 362, 471, 689 and 1087 m/s, respectively. Atoms are colored by the CNA method. Gray, blue and red colors are associated with unshocked BCC, uniaxially compressed BCC and the transformed close-packed grains, respectively.

length scale and ns time scale resolution. For example, Kadau et al. [25] observed BCC to HCP phase transformation of Fe single crystal during shock. For shock above a certain strength, they reported nucleation of HCP clusters within the BCC Fe lattice, leading to the formation of a phase transformation wave behind the elastic precursor wave for lower particle velocities, and an overdriven phase transformation wave for greater particle velocities, which is shown in Figure 1.6. In a later work, to explore the role of lattice orientation on phase transformation of shocked

single crystal Fe, Kadau et al. [18] performed shock simulations in <100>, <110> and <111> directions. They reported that the BCC to HCP/FCC (closed-pack material) phase transformation during <100> shock is a shuffle dominant mechanism. On the other hand, the phase transformation during <110> and <111> shock includes a large shear contribution. Gunkelmann et al. [28] investigated the BCC to HCP phase transformation in nanocrystalline Fe during shock, and reported dislocation generation at grain boundaries before the phase transformation.

Recently, Bolesta and Fomin [52] reported a FCC to BCC phase transformation behind the shock wave front of nanocrystalline Cu. They reported that for the range of grain diameters from 2 to 12 nm, grain size does not significantly influence the shock Hugoniot curve. For shock pressures between 100 and 200 GPa, they reported a FCC to BCC phase transformation behind the shock front via an approach based on the structure factor equation, which is shown in Figure 1.7. Upon unloading of the shock, the BCC structure reverted back to a FCC lattice below 1150 K and 66 GPa, forming a cellular stacking fault structure. However, Bolesta and Fomin did not explore the role of grain size, grain orientation and particle velocity on the uniaxial compression of FCC lattice towards the BCC structure behind the shock front of nanocrystalline Cu, which will be studied in this dissertation. In addition, the assessment of embedded-atom (EAM) interatomic potential and adaptive common neighbor analysis [53] to predict and identify crystal structures emerging behind the <100> shock front of single crystal Cu will be discussed in this dissertation as well.

X-ray diffraction (XRD) is a powerful technique to characterize plastic deformations in solid materials. Several experimental studies have been done to characterize macroscopic properties of shocked solid materials using XRD method, including phase transformation [54–56] and strength of materials subjected to shock loading [14,32,57]. However, there are very few studies that

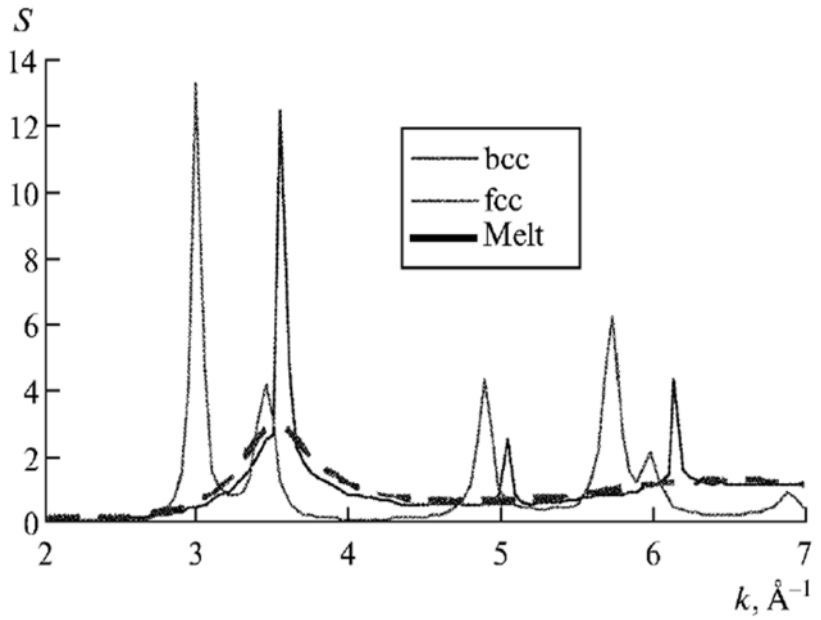

Figure 1.7: Identification of BCC structure for a nanocrystalline Cu sample during shock using a structure factor approach [52].

quantify microscopic plastic properties of shocked solid materials using XRD method, including calculation of dislocation density [32,39], microstrain [58] and polycrystalline grain size [32,56]. For example, Turneaure et al. [58] used a real-time x-ray diffraction method to obtain microstructural information for <100> shock in single crystal Al up to 7.1 GPa pressure using plate impact loading. Figure 1.8 shows a schematic of this experimental x-ray diffraction characterization. They used Williamson-Hall [59] and Profile Synthesis [60] methods to analyze the x-ray diffraction line profile and determine the microstrain behind the shock front. In addition, Ahn et al. [32] obtained the grain size and dislocation density of shocked ultrafine copper after analyzing the x-ray diffraction line profile by Convolution Multiple Whole Profile (CMWP) method [61].

On the other hand, Rosolankova et al. [62] calculated dislocation density behind the <100> shock wave front of single crystal Cu using simulated x-ray diffraction method based on a large MD simulation done by Bringa et al. [22]. There were two preexisting prismatic sources of

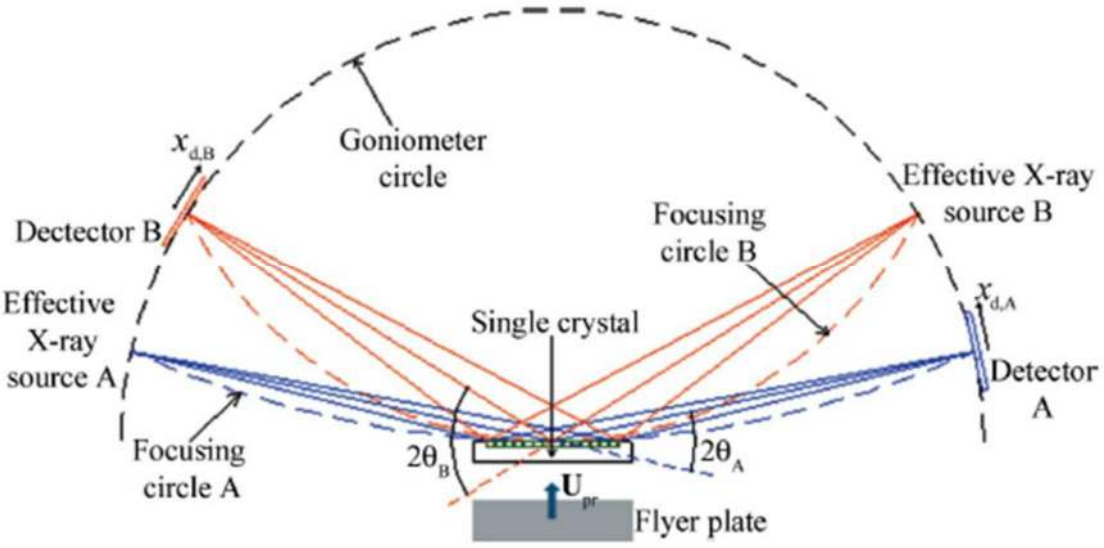

Figure 1.8: Schematic illustration of experimental x-ray diffraction characterization during <100> shock of single crystal Al [58].

dislocation (heterogeneous dislocation nucleation) in their MD model. They performed a single particle velocity of 0.75 km/s (above the HEL) with 50 ps ramp loading time to create shock wave in a MD model with 256 million atoms. To calculate the dislocation density with analyzing the simulated x-ray diffraction data, they compared the results from the second and the fourth diffraction orders. The dislocation density values computed by Rosolankova et al. [62] are shown in Figure 1.9. However, they calculated dislocation density behind the shock front only at 0.75 km/s particle velocity, and they did not calculate the twin boundary density. Another objective of this dissertation is to perform simulated (virtual) [63] x-ray diffraction simulations for <100> shock of single crystal Cu at several particle velocities and initial temperatures at the Hugoniot state. Analysis of these data by Convolution Multiple Whole Profile method can predict the dislocation density and the planar defect densities behind the shock front. While XRD plots will

be provided in this work, the complete analysis of this data for contributions of dislocation density, twin density and temperature effects is beyond the scope of this dissertation.

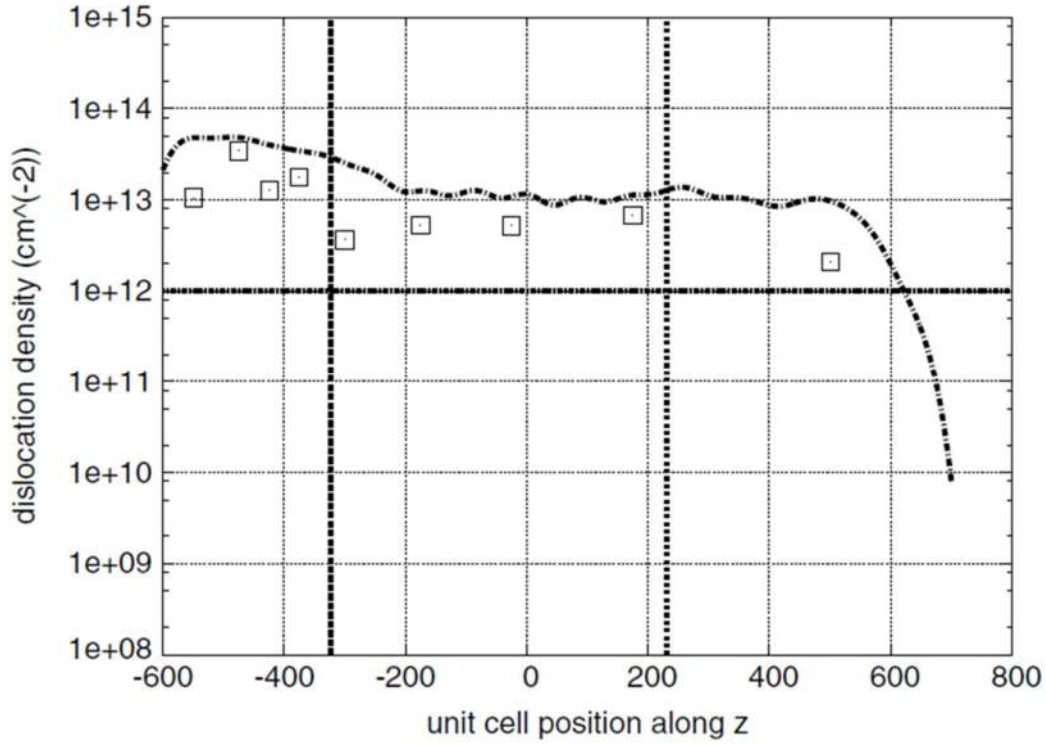

Figure 1.9: Dislocation density values for a single crystal Cu during <100> shock obtained by the simulated x-ray diffraction method [62]. Positions of the prismatic loops are indicated by the dashed vertical lines.

1.3 Dissertation Structure

Because a portion of this research has been published previously in peer-reviewed journals, this dissertation is formed in the "Published Papers" format, and every published paper will be presented as a unique chapter; this format is in line with the University of Arkansas Graduate School. Chapter 2 contains a background on the atomistic simulations (molecular dynamics and molecular statics) and embedded-atom (EAM) interatomic potential which is used in this study.

Chapter 2 also includes a brief explanation of traditional characterization tools in atomistic simulations as well as the simulated (virtual) diffraction method.

Chapter 3 presents the dependency of dislocation density generation and plastic relaxation in single crystal Cu during shock on particle velocity and shock orientation using molecular dynamics simulations. Four different shock directions are selected: <100>, <110>, <111> and <321> to study the role lattice orientation on dislocation density generation and plastic relaxation. Simulations are performed for particle velocities between the HEL for each orientation up to a maximum of 1.5 km/s. Dislocation densities are calculated via the DXA method, which is potentially more accurate and inclusive than the centrosymmetry-based approach used in prior work [22].

In Chapter 4, the ability of the embedded-atom method (EAM) interatomic potential to predict defects and phase transformations behind the shock front of single crystal Cu in <100> direction will be assessed. In addition, the capability of the CNA method with adaptive cut off distance to identify crystal structures behind the <100> shock front will be evaluated. Shock simulations are performed for particle velocities from 0.5 to 1.7 km/s, and initial temperatures of 5, 300 and 600 K. To explain the observation of different Cu crystal structures that dynamically form during shock and remain at the Hugoniot state, free energy calculations are also employed.

Chapter 5 presents how the uniaxially compressed FCC Cu towards the BCC structure in nanocrystalline Cu depends on particle velocity, grain size and grain orientation using molecular dynamics simulations. Particle velocities from 1.0 to 3.4 km/s (40 to 256 GPa pressures) are applied and uniaxial compression of FCC Cu towards the BCC structures is observed for

pressures between 100 to 200 GPa. Four different grain diameters (6, 11, 16 and 26 nm) are selected to study the influence of grain size on the Hugoniot state and uniaxial compression.

Chapter 6 includes simulated x-ray diffraction (XRD) and selected area electron diffraction (SAED) results for nanocrystalline Cu with grain diameters of 5, 10 and 15 nm based on molecular statics data at 0 K temperature. Williamson-Hall analysis is performed to analyze the x-ray diffraction line profiles and predict the nanocrystalline grain diameter and microstrain. To extend the diffraction results for shock simulations, the simulated x-ray diffraction is performed for MD results of <100> shock of single crystal Cu at particle velocities between 0.7 to 1.0 km/s and initial temperatures of 5, 300 and 600 K at the Hugoniot state. Results show that there is a peak broadening in x-ray diffraction line profile due to emergence of defects (dislocations, stacking faults and twins) behind the shock front of single crystal Cu. To explore the influence of particle velocity and initial temperature on dislocation density and planar defect densities (stacking fault and twinning) behind the <100> shock front, Convolution Multiple Whole Profile method can be used to analyze the preliminary diffraction data, but this is beyond the scope of this dissertation.

Lastly, Chapter 7 summarizes the conclusions and makes recommendations for future research. Specifically, this includes recommendation for extension of shock simulations for nanocrystalline Cu models and determination of the role of grain size, grain orientation and structure of grain boundaries on dislocation generation and plastic relaxation behind the shock front.

References

[1] M. Itoh, M. Katayama, and R. Rainsberger, "Computer Simulation of a Boeing 747 Passenger Jet Crashing into a Reinforced Concrete Wall," *Mater. Sci. Forum*, vol. 465–466, pp. 73–78, 2004.

[2] M. Acarer, B. Gülenç, and F. Findik, "Investigation of explosive welding parameters and their effects on microhardness and shear strength," *Mater. Des.*, vol. 24, no. 8, pp. 659–664, Dec. 2003.

[3] W. L. Cheng and S. Itoh, "High Velocity Impact of Steel Fragment on Thick Aluminum Target," *Mater. Sci. Forum*, vol. 465–466, pp. 49–54, 2004.

[4] K. Siva Kumar, D. J. Singh, and T. Balakrishna Bhat, "Studies on Aluminum Armour Plates Impacted by Deformable and Non-Deformable Projectiles," *Mater. Sci. Forum*, vol. 465–466, pp. 79–84, 2004.

[5] E. P. Turtle and E. Pierazzo, "Thickness of a Europan Ice Shell from Impact Crater Simulations," *Science*, vol. 294, no. 5545, pp. 1326–1328, Nov. 2001.

[6] J. D. Slavin, A. P. Jones, and A. G. G. M. Tielens, "Shock Processing of Large Grains in the Interstellar Medium," *Astrophys. J.*, vol. 614, no. 2, pp. 796–806, Oct. 2004.

[7] E. M. Bringa, A. Caro, Y. Wang, M. Victoria, J. M. McNaney, B. A. Remington, R. F. Smith, B. R. Torralva, and H. Van Swygenhoven, "Ultrahigh Strength in Nanocrystalline Materials Under Shock Loading," *Science*, vol. 309, no. 5742, pp. 1838–1841, Sep. 2005.

[8] A. C. Mitchell and W. J. Nellis, "Shock compression of aluminum, copper, and tantalum," *J. Appl. Phys.*, vol. 52, no. 5, pp. 3363–3374, 1981.

[9] W. J. Nellis, J. A. Moriarty, A. C. Mitchell, M. Ross, R. G. Dandrea, N. W. Ashcroft, N. C. Holmes, and G. R. Gathers, "Metals physics at ultrahigh pressure: Aluminum, copper, and lead as prototypes," *Phys. Rev. Lett.*, vol. 60, no. 14, pp. 1414–1417, Apr. 1988.

[10] W. J. Nellis, A. C. Mitchell, and D. A. Young, "Equation-of-state measurements for aluminum, copper, and tantalum in the pressure range 80–440 GPa (0.8–4.4 Mbar)," *J. Appl. Phys.*, vol. 93, no. 1, pp. 304–310, Jan. 2003.

[11] M. A. Meyers, F. Gregori, B. K. Kad, M. S. Schneider, D. H. Kalantar, B. A. Remington, G. Ravichandran, T. Boehly, and J. S. Wark, "Laser-induced shock compression of monocrystalline copper: characterization and analysis," *Acta Mater.*, vol. 51, no. 5, pp. 1211–1228, Mar. 2003.

[12] A. M. Podurets, V. A. Raevskii, V. G. Khanzhin, A. I. Lebedev, O. N. Aprelkov, V. V. Igonin, I. N. Kondrokhina, A. N. Balandina, M. I. Tkachenko, J. Petit, and M. A. Zocher, "Twin structures in copper after shock and Shockless high-rate loading," *Combust. Explos. Shock Waves*, vol. 47, no. 5, pp. 606–614, 2011.

[13] M. S. Schneider, B. K. Kad, M. A. Meyers, F. Gregori, D. Kalantar, and B. A. Remington,

"Laser-induced shock compression of copper: Orientation and pressure decay effects," *Metall. Mater. Trans. A*, vol. 35, no. 9, pp. 2633–2646, 2004.

[14] W. J. Murphy, A. Higginbotham, G. Kimminau, B. Barbrel, E. M. Bringa, J. Hawreliak, R. Kodama, M. Koenig, W. McBarron, M. A. Meyers, B. Nagler, N. Ozaki, N. Park, B. Remington, S. Rothman, S. M. Vinko, T. Whitcher, and J. S. Wark, "The strength of single crystal copper under uniaxial shock compression at 100 GPa," *J. Phys. Condens. Matter*, vol. 22, no. 6, p. 65404, Feb. 2010.

[15] B. L. Holian and P. S. Lomdahl, "Plasticity Induced by Shock Waves in Nonequilibrium Molecular-Dynamics Simulations," *Science*, vol. 280, no. 5372, pp. 2085–2088, Jun. 1998.

[16] T. C. Germann, B. L. Holian, P. S. Lomdahl, and R. Ravelo, "Orientation Dependence in Molecular Dynamics Simulations of Shocked Single Crystals," *Phys. Rev. Lett.*, vol. 84, no. 23, pp. 5351–5354, Jun. 2000.

[17] K. Kadau, F. J. Cherne, R. Ravelo, and T. C. Germann, "Shock-induced phase transformations in gallium single crystals by atomistic methods," *Phys. Rev. B*, vol. 88, no. 14, p. 144108, Oct. 2013.

[18] K. Kadau, T. C. Germann, P. S. Lomdahl, and B. L. Holian, "Atomistic simulations of shock-induced transformations and their orientation dependence in bcc Fe single crystals," *Phys. Rev. B*, vol. 72, no. 6, p. 64120, Aug. 2005.

[19] G. A. Malygin, S. L. Ogarkov, and A. V Andriyash, "A dislocation kinetic model of the formation and propagation of intense shock waves in crystals," *Phys. Solid State*, vol. 55, no. 4, pp. 787–795, Apr. 2013.

[20] J. Petit and J. L. Dequiedt, "Constitutive relations for copper under shock wave loading: Twinning activation," *Mech. Mater.*, vol. 38, no. 3, pp. 173–185, Mar. 2006.

[21] J. D. Clayton, "Analysis of shock compression of strong single crystals with logarithmic thermoelastic-plastic theory," *Int. J. Eng. Sci.*, vol. 79, pp. 1–20, Jun. 2014.

[22] E. M. Bringa, K. Rosolankova, R. E. Rudd, B. A. Remington, J. S. Wark, M. Duchaineau, D. H. Kalantar, J. Hawreliak, and J. Belak, "Shock deformation of face-centred-cubic metals on subnanosecond timescales," *Nat. Mater.*, vol. 5, no. 10, pp. 805–809, Oct. 2006.

[23] M. A. Shehadeh, H. M. Zbib, and T. D. De La Rubia, "Multiscale dislocation dynamics simulations of shock compression in copper single crystal," *Int. J. Plast.*, vol. 21, no. 12, pp. 2369–2390, 2005.

[24] M. A. Shehadeh, E. M. Bringa, H. M. Zbib, J. M. McNaney, and B. A. Remington, "Simulation of shock-induced plasticity including homogeneous and heterogeneous dislocation nucleations," *Appl. Phys. Lett.*, vol. 89, no. 17, p. 171918, 2006.

[25] K. Kadau, T. C. Germann, P. S. Lomdahl, and B. L. Holian, "Microscopic View of Structural Phase Transitions Induced by Shock Waves," *Science*, vol. 296, no. 5573, pp.

1681–1684, May 2002.

[26] T. C. Germann, B. L. Holian, P. S. Lomdahl, D. Tanguy, M. Mareschal, and R. Ravelo, “Dislocation structure behind a shock front in fcc perfect crystals: Atomistic simulation results,” *Metall. Mater. Trans. A*, vol. 35, no. 9, pp. 2609–2615, 2004.

[27] N. Gunkelmann, E. M. Bringa, K. Kang, G. J. Ackland, C. J. Ruestes, and H. M. Urbassek, “Polycrystalline iron under compression: Plasticity and phase transitions,” *Phys. Rev. B*, vol. 86, no. 14, p. 144111, Oct. 2012.

[28] N. Gunkelmann, E. M. Bringa, D. R. Tramontina, C. J. Ruestes, M. J. Suggit, A. Higginbotham, J. S. Wark, and H. M. Urbassek, “Shock waves in polycrystalline iron: Plasticity and phase transitions,” *Phys. Rev. B*, vol. 89, no. 14, p. 140102, 2014.

[29] C. L. Kelchner, S. J. Plimpton, and J. C. Hamilton, “Dislocation nucleation and defect structure during surface indentation,” *Phys. Rev. B*, vol. 58, no. 17, pp. 11085–11088, Nov. 1998.

[30] J. D. Honeycutt and H. C. Andersen, “Molecular dynamics study of melting and freezing of small Lennard-Jones clusters,” *J. Phys. Chem.*, vol. 91, no. 19, pp. 4950–4963, Sep. 1987.

[31] A. Stukowski and K. Albe, “Extracting dislocations and non-dislocation crystal defects from atomistic simulation data,” *Model. Simul. Mater. Sci. Eng.*, vol. 18, no. 8, p. 85001, 2010.

[32] D.-H. Ahn, W. Kim, M. Kang, L. J. Park, S. Lee, and H. S. Kim, “Plastic deformation and microstructural evolution during the shock consolidation of ultrafine copper powders,” *Mater. Sci. Eng. A*, vol. 625, pp. 230–244, Feb. 2015.

[33] R. I. Barabash, G. E. Ice, M. Kumar, J. Ilavsky, and J. Belak, “Polychromatic microdiffraction analysis of defect self-organization in shock deformed single crystals,” *Int. J. Plast.*, vol. 25, no. 11, pp. 2081–2093, Nov. 2009.

[34] Y. Xiong, T. He, F. Ren, P. Li, L. Chen, and A. A. Volinsky, “Microstructure Evolution and Microhardness of Ultrafine-grained High Carbon Steel during Multiple Laser Shock Processing,” *J. Iron Steel Res. Int.*, vol. 22, no. 1, pp. 55–59, Jan. 2015.

[35] H. A. Colorado, A. Navarro, S. V. Prikhodko, J. M. Yang, N. Ghoniem, and V. Gupta, “Ultrahigh strain-rate bending of copper nanopillars with laser-generated shock waves,” *J. Appl. Phys.*, vol. 114, no. 23, p. 233510, Dec. 2013.

[36] G. T. Gray, N. K. Bourne, V. Livescu, C. P. Trujillo, S. MacDonald, and P. Withers, “The influence of shock-loading path on the spallation response of Ta,” *J. Phys. Conf. Ser.*, vol. 500, no. 11, p. 112031, May 2014.

[37] D. Tanguy, M. Mareschal, P. S. Lomdahl, T. C. Germann, B. L. Holian, and R. Ravelo, “Dislocation nucleation induced by a shock wave in a perfect crystal: Molecular dynamics simulations and elastic calculations,” *Phys. Rev. B*, vol. 68, no. 14, p. 144111, Oct. 2003.

[38] D. Tanguy, M. Mareschal, T. C. Germann, B. L. Holian, P. S. Lomdahl, and R. Ravelo, "Plasticity induced by a shock wave: large scale molecular dynamics simulations," *Mater. Sci. Eng. A*, vol. 387–389, no. 1–2 SPEC. ISS., pp. 262–265, Dec. 2004.

[39] A. M. Podurets, M. I. Tkachenko, O. N. Ignatova, A. I. Lebedev, V. V. Igonin, and V. A. Raevskii, "Dislocation density in copper and tantalum subjected to shock compression depending on loading parameters and original microstructure," *Phys. Met. Metallogr.*, vol. 114, no. 5, pp. 440–447, May 2013.

[40] L. E. Murr, *Shock Waves and High-Strain-Rate Phenomena in Metals*. New York, 1981.

[41] A. M. He, S. Q. Duan, J. L. Shao, P. Wang, and S. N. Luo, "Local and bulk melting of shocked columnar nanocrystalline Cu: Dynamics, anisotropy, premelting, superheating, supercooling, and re-crystallization.," *J. Chem. Phys.*, vol. 139, no. 7, p. 74502, Aug. 2013.

[42] E. M. Bringa, J. U. Cazamias, P. Erhart, J. Stölken, N. Tanushev, B. D. Wirth, R. E. Rudd, and M. J. Caturla, "Atomistic shock Hugoniot simulation of single-crystal copper," *J. Appl. Phys.*, vol. 96, no. 7, p. 3793, 2004.

[43] A. Loveridge-Smith, A. Allen, J. Belak, T. Boehly, A. Hauer, B. Holian, D. Kalantar, G. Kyrala, R. W. Lee, P. Lomdahl, M. A. Meyers, D. Paisley, S. Pollaine, B. Remington, D. C. Swift, S. Weber, and J. S. Wark, "Anomalous elastic response of silicon to uniaxial shock compression on nanosecond time scales," *Phys. Rev. Lett.*, vol. 86, no. 11, pp. 2349–2352, 2001.

[44] P. A. Rigg and Y. M. Gupta, "Multiple x-ray diffraction to determine transverse and longitudinal lattice deformation in shocked lithium fluoride," *Phys. Rev. B*, vol. 63, no. 9, p. 94112, Feb. 2001.

[45] K. Rosolankova, *Shock Compression of Condensed Matter*. New York, 2003.

[46] A. Bolesta, L. Zheng, D. Thompson, and T. Sewell, "Molecular dynamics simulations of shock waves using the absorbing boundary condition: A case study of methane," *Phys. Rev. B*, vol. 76, no. 22, p. 224108, Dec. 2007.

[47] F. J. Cherne, M. I. Baskes, T. C. Germann, R. J. Ravelo, and K. Kadau, "Shock Hugoniot and Melt Curve for a Modified Embedded Atom Method Model of Gallium," *AIP Conference Proceedings*, vol. 706. pp. 281–284, 2004.

[48] K. Kadau, T. C. Germann, P. S. Lomdahl, and B. L. Holian, "Atomistic simulations of shock-induced melting in Fe," *AIP Conference Proceedings*, vol. 845. pp. 236–239, 2006.

[49] A. M. He, P. Wang, J. L. Shao, S. Q. Duan, F. P. Zhao, and S. N. Luo, "Solid-liquid phase transitions in single crystal Cu under shock and release conditions," *J. Appl. Phys.*, vol. 115, no. 14, p. 143503, Apr. 2014.

[50] V. I. Levitas and R. Ravelo, "Virtual melting as a new mechanism of stress relaxation under high strain rate loading.," *Proc. Natl. Acad. Sci. U. S. A.*, vol. 109, no. 33, pp.

13204–7, Aug. 2012.

[51] N. Gunkelmann, D. R. Tramontina, E. M. Bringa, and H. M. Urbassek, “Interplay of plasticity and phase transformation in shock wave propagation in nanocrystalline iron,” *New J. Phys.*, vol. 16, no. 9, p. 93032, Sep. 2014.

[52] A. V. Bolesta and V. M. Fomin, “Phase transition behind a shock front in polycrystalline copper,” *Dokl. Phys.*, vol. 59, no. 6, pp. 249–253, Jul. 2014.

[53] A. Stukowski, “Structure identification methods for atomistic simulations of crystalline materials,” *Model. Simul. Mater. Sci. Eng.*, vol. 20, no. 4, p. 45021, Jun. 2012.

[54] D. J. Funk, C. A. Meserole, D. E. Hof, G. L. Fisher, J. Roberts, A. J. Taylor, H. J. Lee, J. Workman, and Q. McCulloch, “An Ultrafast X-Ray Diffraction Apparatus for the Study of Shock Waves,” in *AIP Conference Proceedings*, 2004, vol. 706, no. May 2015, pp. 1155–1158.

[55] J. Hawreliak, M. Butterfield, H. Davies, B. El-Dasher, A. Higginbotham, D. Kalantar, G. Kimminau, J. McNaney, D. Milathianaki, W. Murphy, B. Nagler, N. Park, B. Remington, L. Thorton, T. Whitcher, J. Wark, and H. Lorenzana, “IN-SITU PROBING OF LATTICE RESPONSE IN SHOCK COMPRESSED MATERIALS USING X-RAY DIFFRACTION,” in *AIP Conference Proceedings*, 2008, vol. 955, pp. 1327–1332.

[56] J. A. Hawreliak, D. H. Kalantar, J. S. Stölken, B. A. Remington, H. E. Lorenzana, and J. S. Wark, “High-pressure nanocrystalline structure of a shock-compressed single crystal of iron,” *Phys. Rev. B*, vol. 78, no. 22, p. 220101, Dec. 2008.

[57] A. J. Comley, B. R. Maddox, R. E. Rudd, S. T. Prisbrey, J. A. Hawreliak, D. A. Orlikowski, S. C. Peterson, J. H. Satcher, A. J. Elsholz, H.-S. Park, B. A. Remington, N. Bazin, J. M. Foster, P. Graham, N. Park, P. A. Rosen, S. R. Rothman, A. Higginbotham, M. Suggit, and J. S. Wark, “Strength of Shock-Loaded Single-Crystal Tantalum [100] Determined using In Situ Broadband X-Ray Laue Diffraction,” *Phys. Rev. Lett.*, vol. 110, no. 11, p. 115501, Mar. 2013.

[58] S. J. Turneaure and Y. M. Gupta, “Real-time microstructure of shock-compressed single crystals from X-ray diffraction line profiles,” *J. Appl. Crystallogr.*, vol. 44, no. 3, pp. 574–584, Jun. 2011.

[59] G. K. Williamson and W. H. Hall, “X-ray line broadening from filed aluminium and wolfram,” *Acta Metall.*, vol. 1, no. 1, pp. 22–31, Jan. 1953.

[60] P. Scardi, M. Leoni, and Y. H. Dong, “Whole diffraction pattern-fitting of polycrystalline fcc materials based on microstructure,” *Eur. Phys. J. B*, vol. 18, no. 1, pp. 23–30, Nov. 2000.

[61] G. Ribárik, J. Gubicza, and T. Ungár, “Correlation between strength and microstructure of ball-milled Al–Mg alloys determined by X-ray diffraction,” *Mater. Sci. Eng. A*, vol. 387–389, no. 1–2 SPEC. ISS., pp. 343–347, Dec. 2004.

[62] K. Rosolankova, J. S. Wark, E. M. Bringa, and J. Hawreliak, “Measuring stacking fault densities in shock-compressed FCC crystals using in situ x-ray diffraction,” *J. Phys. Condens. Matter*, vol. 18, no. 29, pp. 6749–6757, Jul. 2006.

[63] S. P. Coleman, D. E. Spearot, and L. Capolungo, “Virtual diffraction analysis of Ni [0 1 0] symmetric tilt grain boundaries,” *Model. Simul. Mater. Sci. Eng.*, vol. 21, no. 5, p. 55020, Jul. 2013.

Chapter 2: Background

2.1 Atomistic Simulations

The atomistic simulation method, including molecular dynamics (MD) and molecular statics (MS), is a well-known computational technique to predict physical and chemical properties of materials at the atomic level. In this research, the molecular dynamics simulation method is used to model the propagation of shock waves in single crystal and nanocrystalline Cu to understand plasticity mechanisms, including dislocation generation/relaxation and phase transformations behind the shock front. In addition, a part of this research (Chapter 6) utilizes molecular statics simulations to obtain the configuration of atoms corresponding to the minimum energy level for nanocrystalline Cu models. In the MD and MS methods, each atom is considered as a single point mass, including both the nucleus and the electrons around the atom. This means that the electronic structure rules are not directly included in the MD and MS simulations. Instead, first principal simulation methods use these electronic structure rules to provide data that is used to derive an interatomic potential to describe the interactions between atoms. The accuracy of atomistic simulations strongly depends on the choice of interatomic potential, which depends on the type of material and the physical (or chemical) conditions of simulated phenomena.

The force on each atom, $\mathbf{F_i}$, is calculated via the spatial gradient of the interatomic potential function U_i:

$$\mathbf{F_i} = -\nabla U_i \tag{2.1}$$

where U_i is a function of the atomic positions of the neighbor atoms to i. For most interatomic potentials, there is a distance associated with minimum potential energy at which atoms are at the

equilibrium state and do not exert repulsive/attractive force on each other. If the distance between the interacted atoms becomes greater than the equilibrium distance, atoms tend to exert an attractive force. On the other hand, if the distance between the interacted atoms is smaller than the equilibrium distance, atoms interact via a repulsive force. Figure 2.1 shows a schematic of the potential energy between two atoms as a function of interatomic distance [1] for a simple Lennard-Jones interatomic potential. In addition, there is a cutoff distance which is defined for the interatomic potential, and only within this cutoff distance, atoms can influence each other by repulsive/attractive forces. The summation of all acting forces on a specific atom, results in the total force for that atom. More details regarding interatomic potentials and the specific interatomic potential chosen to model shock simulations of single crystal and nanocrystalline Cu are in Section 2.1.3.

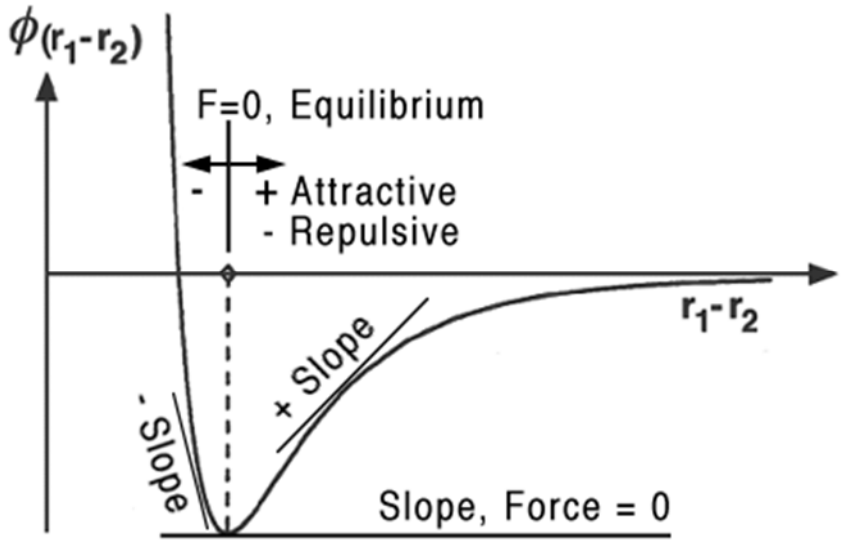

Figure 2.1: Schematic of the potential energy between two atoms as a function of interatomic distance [1] for a simple Lennard-Jones interatomic potential.

Several boundary conditions are applied in this research to provide appropriate constraints for shock simulations, including periodic boundary conditions [2], the momentum mirror technique [3] and absorbing wall boundary condition [4]. The periodic boundary conditions are commonly used in atomistic simulations to mimic infinite systems while modeling a finite collection of atoms. Atoms under the periodic boundary conditions can migrate from one side of the atomistic simulation box to the opposite side. By applying periodic boundary conditions in the atomistic shock simulations, mimicking an infinite system, the plastic deformation mechanisms can be compared by those obtained from the shock experiments.

The momentum mirror technique is one of the most common methods to generate shock waves in atomistic shock simulations. Shock is induced by impacting the sample with an infinitely massive piston moving at velocity u_p; all atoms which are contacting the piston are reflected back by a flat momentum mirror. Conversely, shock can be created by assigning each atom a velocity of $-u_p$in the shock loading direction, impacting the sample with a stationary infinite mass wall. To study the plastic deformation mechanisms of shocked single crystal and nanocrystalline Cu for longer times, allowing the system to reach the Hugoniot equilibrium state, the absorbing wall boundary condition is applied for the shock simulations in this research. After passing the shock wave through the sample and at the precise time it reaches the end of the sample, the absorbing wall boundary condition is applied at the end of the sample to prevent the tension wave at the rear surface. If a stationary infinite mass wall is used to induce the shock wave, the absorbing wall boundary condition will be a stationary infinite mass wall. Instead, if a moving infinite mass wall with a velocity of u_p creates the shock wave, the absorbing wall

boundary condition will be a moving infinite mass wall with a velocity of u_p. Figure 2.2 shows a schematic illustration of the absorbing wall boundary condition.

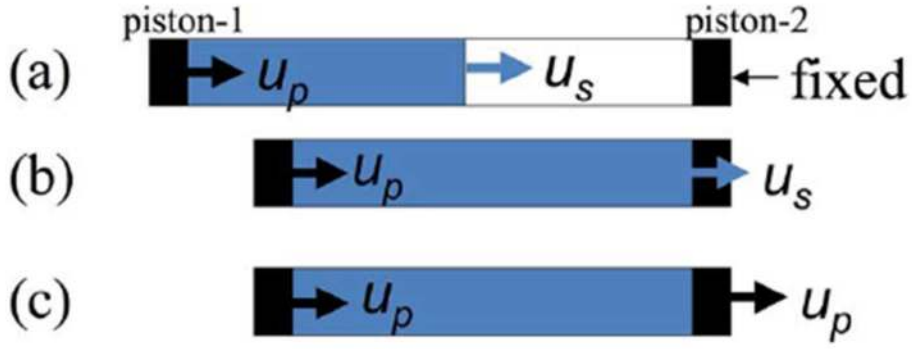

Figure 2.2: Schematic illustration of the absorbing wall boundary condition for a case with moving infinite mass wall [4].

2.1.1 Molecular Dynamics

MD simulations include a set of equations of motion based on Newton's second law of motion to calculate positions, $\mathbf{r_i}$ and velocities $\dot{\mathbf{r}}_\mathbf{i}$ using acceleration $\ddot{\mathbf{r}}_\mathbf{i}$ (computed from the forces $\mathbf{F_i}$) for each atom over time. To start an integration algorithm, the initial values of these quantities are required for the N atoms within the simulation. The initial crystal structure of the simulated material determines the initial positions $\mathbf{r_i}$. For a desired initial temperature of T, the Gaussian velocity distribution is computed via the equipartition equation [5],

$$\frac{1}{2}\sum_{i=1}^{N} m_i|\dot{\mathbf{r}}_\mathbf{i}|^2 = \frac{3}{2}Nk_BT \tag{2.2}$$

where m_i is the atomic mass and k_B is the Boltzmann constant. The calculation of forces $\mathbf{F_i}$ through Eq. (2.1) provides the acceleration for each atom, $\ddot{\mathbf{r}}_\mathbf{i}$, with Newton's second law of motion.

$$\mathbf{F_i} = m_i \ddot{\mathbf{r}}_\mathbf{i} \tag{2.3}$$

Totally, there are 6N parameters (3N atom positions and 3N atom velocities) that needs to be determined over time by the integration algorithm in an iterative manner using the initial values for atom positions $\mathbf{r_i}$, velocities $\dot{\mathbf{r}}_\mathbf{i}$ and acceleration $\ddot{\mathbf{r}}_\mathbf{i}$.

There are two types of molecular dynamics simulations: (1) equilibrium and (2) non-equilibrium. In the equilibrium molecular dynamics method, the system is energetically isolated from the surrounding environment [6], or in contact with a constant temperature or pressure bath. In the latter case, constraints are employed to control the thermodynamic properties such as pressure and temperature so that the system stays in thermodynamic equilibrium state with the external bath. However, in the non-equilibrium molecular dynamics (NEMD), the system interacts dynamically with the surrounding environment via thermal or physical constraints [6], and there is no goal to reach the system towards a thermodynamically equilibrium state.

For the shock simulations in this research, NEMD is utilized under the constraints that the total energy (kinetic plus potential energy) of the system is conserved. LAMMPS software [7], which is used in this research, utilizes the velocity-Verlet method as an integration algorithm for the microcanonical NVE ensemble. The velocity-Verlet method computes the atomic positions and velocities at time $t + \Delta t$ from the previous values at time t via the equations [8]:

$$\dot{\mathbf{r}}_\mathbf{i}\left(t+\frac{\Delta t}{2}\right)=\dot{\mathbf{r}}_\mathbf{i}(t)+\frac{\Delta t}{2}\ddot{\mathbf{r}}_\mathbf{i}(t) \tag{2.4}$$

$$\mathbf{r}_\mathbf{i}(t+\Delta t)=\mathbf{r}_\mathbf{i}(t)+\dot{\mathbf{r}}_\mathbf{i}\left(t+\frac{\Delta t}{2}\right)\Delta t \tag{2.5}$$

$$\mathbf{F}_\mathbf{i}=-\nabla U_i(r_i{}^N(t+\Delta t)) \tag{2.6}$$

$$\dot{\mathbf{r}}_\mathbf{i}(t+\Delta t)=\dot{\mathbf{r}}_\mathbf{i}\left(t+\frac{\Delta t}{2}\right)+\frac{1}{2}\ddot{\mathbf{r}}_\mathbf{i}(t+\Delta t)\Delta t \tag{2.7}$$

where Δt is the timestep. For all simulations in this research, the duration of the timestep is set to 1 femtosecond to accurately capture the atomic vibrations during the shock simulations.

In the equilibrium molecular dynamics, to include thermodynamic boundary conditions such as temperature and pressure control [9–13], modified version of Newton's second law of motion can be used. For example, to reach a desired pressure and temperature of models before the shock simulation, equilibrium molecular dynamics using the isothermal-isobaric ensemble (NPT) is performed in this research. The NPT ensemble conserves the number of atoms, the pressure and the temperature of system during simulation. LAMMPS utilizes equations developed by Shinoda et al. [14] for NPT ensemble, which are based on the Nose-Hoover thermostat approach [11]. In the Nose-Hoover thermostat approach, an additional frictional term, ζ, is included in Newton's second law of motion to move the system towards a desired temperature of, T_0, by using the equations,

$$\mathbf{F}_\mathbf{i}=m_i\ddot{\mathbf{r}}_\mathbf{i}+\zeta m_i\dot{\mathbf{r}}_\mathbf{i} \tag{2.8}$$

$$\zeta = v_T^2\left(\frac{T}{T_0} - 1\right) \tag{2.9}$$

where v_T is the thermostat rate. The Nose-Hoover thermostat approach can reach the system to a desired temperature of T_0 by scaling the atomic velocities. The details regarding the modification of the velocity-Verlet integration algorithm for NPT ensemble based on the Nose-Hoover thermostat approach can be found in [12].

2.1.2 Molecular Statics

The objective of molecular statics simulations is to determine a minimum energy configuration of atoms within the simulation at 0 K temperature. The molecular statics simulations include iterative algorithms to search for atomic positions, $\mathbf{r_N}$, that minimize the potential energy of the simulation system. The role of these iterative algorithms is to change the atomic positions along a specific search direction, and obtain a lower potential energy for the simulation system,

$$\mathbf{r_N}^{(k+1)} = \begin{cases} \mathbf{r_N}^{(0)} & \text{if } k = 0 \\ \mathbf{r_N}^{(k)} + \alpha^{(k)}\mathbf{d}^{(k)} & \text{if } k > 0 \end{cases} \tag{2.10}$$

where k is the iteration number, $\alpha^{(k)}$ is the step size and $\mathbf{d}^{(k)}$ is the search direction. The search direction utilizes the forces acting on the atoms using Eq. (2.1), $\mathbf{F} = -\nabla U_i(\mathbf{r_N})$, to capture a direction with the greatest decrease of potential energy function. The search directions are calculated via,

$$\mathbf{d}^{(k+1)} = \begin{cases} \mathbf{F}^{(0)} & \text{if } k = 0 \\ \mathbf{F}^{(k+1)} + \beta^{(k+1)}\mathbf{d}^{(k)} & \text{if } k > 0 \end{cases} \tag{2.11}$$

where $\beta^{(k)}$ is an update parameter to scale the search direction from the previous step.

There are two approaches in the molecular statics simulations to update the search directions: (1) steepest decent and (2) conjugate gradient. The steepest decent approach does not include an input from the previous search direction and $\beta^{(k)} = 0$. This means the search directions follow normal to the contour lines of the potential energy surface. Because the potential energy surfaces are complicated for most atomistic simulations, the molecular statics method using steepest decent approach does not converge quickly. Instead, the conjugate gradient approach includes an update parameter $\beta^{(k)}$, and uses information from the previous search direction. LAMMPS utilizes an update parameter for the conjugate gradient approach developed by Polak and Ribiere [15].

$$\beta^{(k+1)} = \frac{\mathbf{F}^{(k+1)^T}\left(\mathbf{F}^{(k+1)} - \mathbf{F}^{(k)}\right)}{\mathbf{F}^{(k)^T}\mathbf{F}^{(k)}} \tag{2.12}$$

2.1.3 Interatomic Potentials

For all atomistic simulations, choosing a reliable interatomic potential, U_i, to obtain realistic results is necessary. There are several types of interatomic potentials depending on specific material and phenomenon of interest, and they include unique terms to describe individual atomic interactions,

$$U_i = \sum E_{Interaction} \tag{2.13}$$

and this summation is over neighbors to atom i. The simplest form of interatomic potentials contain the pair-wise interaction of atoms, E_{Pair} , based only on the interatomic distance r_{ij} between atom i and atom j. For example, Buckingham [16] developed an interatomic potential based on the pair-wise interaction of atoms for several ideal gasses,

$$E_{Pair} = Aexp\left(\frac{-r_{ij}}{\rho}\right) - \frac{C}{r_{ij}^6} \tag{2.14}$$

where A is the energy coefficient, ρ is the distance parameter and C optimizes the forces between atomic nuclei and electron clouds for a particular material. However, simple interatomic potentials based only on pair-wise atomic interactions sometimes are unable to describe more complicated aspects of material behaviors. For example, in metallic materials, they do not contain a term to represent the influence of the metallic bonds on the interatomic potential.

Instead, the embedded-atom method (EAM) [17] is a more inclusive interatomic potential to represent metallic behaviors, particularly in transition metals. The embedded-atom method formula includes two terms to describe the atomic interactions: (1) pair potential and (2) embedding energy. The latter term represents the energy atom i experiences when it is embedded in the electron sea provided by its neighbor atoms. The total potential energy for atom i based on the embedded-atom method is [18]:

$$U_i = \frac{1}{2}\sum_{j\neq i} V(r_{ij}) + F(\overline{\rho_i}) \tag{2.15}$$

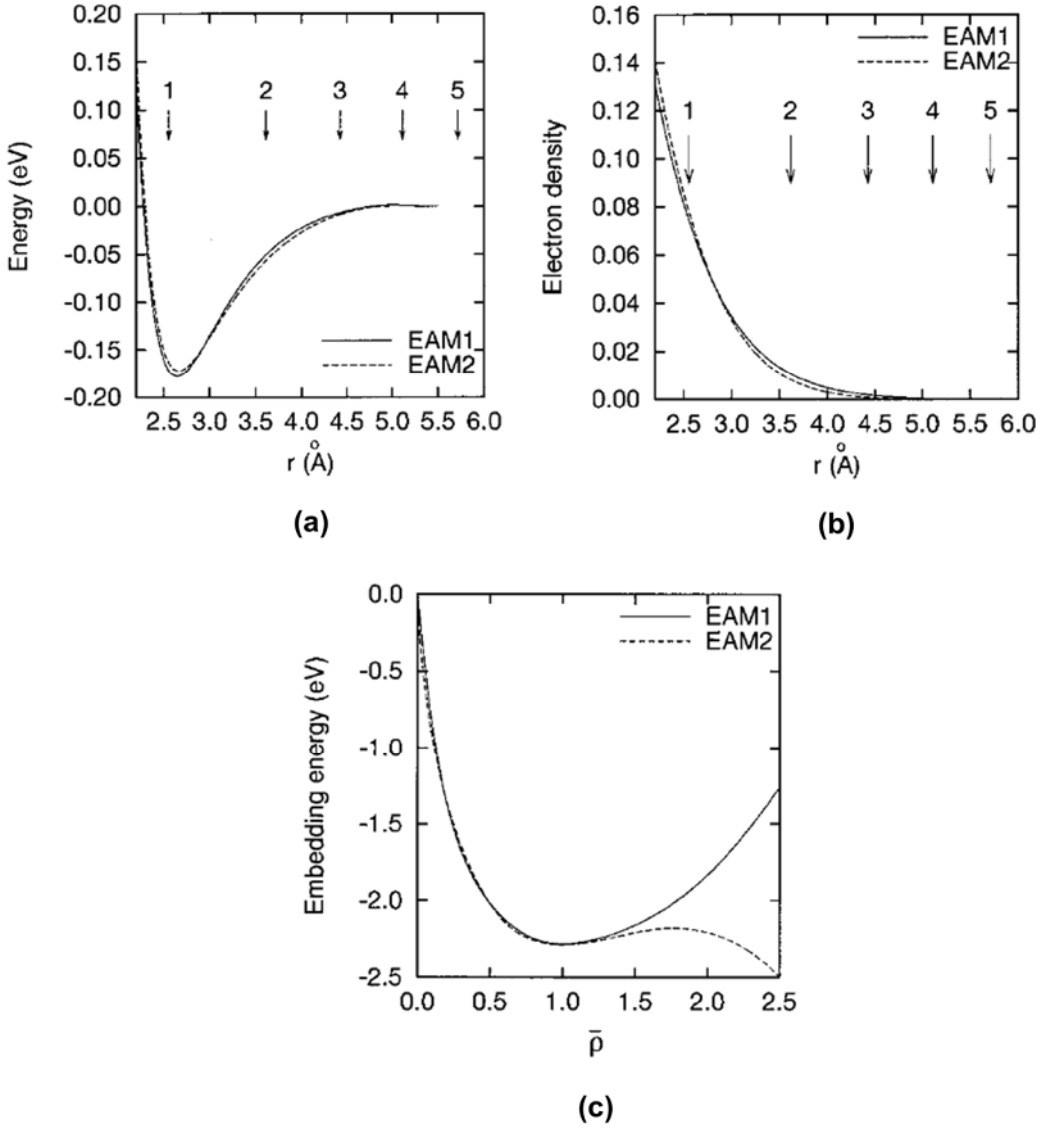

Figure 2.3: Potential functions for the interatomic potentials for Cu developed by Mishin et al. [18]: (a) pair interaction function, (b) electron density function and (c) embedding function. The arrows show coordination radii in FCC lattice.

where $V(r_{ij})$ is a pair potential as a function of interatomic distance r_{ij} between atoms i and j, and F is the embedding energy as a function of the host electron density $\overline{\rho_i}$ induced by all other atoms in the simulation system. The host electron density is given by,

$$\overline{\rho_i} = \sum_{j \neq i} \rho(r_{ij}) \tag{2.16}$$

where $\rho(r_{ij})$ is the electron density function. Figure 2.3 shows pair interaction function, electron density function and embedding function for the interatomic potentials for Cu developed by Mishin et al. [18].

In this research, the embedded-atom method (EAM) potential for Cu developed by Mishin et al. [18] is used (EAM1 in Figure 2.3) as the interatomic potential. This interatomic potential is fit specifically to the unstable and intrinsic stacking fault energies and has been proven in prior work [19] to provide an accurate prediction of dislocation nucleation and dislocation core structures. In addition, this interatomic potential has been shown in prior shock studies to accurately capture the Hugoniot curve [20], dislocation generation/relaxation in single crystal Cu [21] and uniaxial compression of FCC Cu towards the BCC structure in nanocrystalline Cu [22].The ability of this interatomic potential to predict crystal structures behind the shock front at high shock pressures will be evaluated in Chapter 4.

2.2 Characterization Methods in Atomistic Simulations

2.2.1 Centrosymmetry Parameter

Kelchner et al. [23] developed the centrosymmetry parameter to identify dislocation nucleation during indentation of FCC Au. In centrosymmetric materials, such as FCC and BCC materials, the lattice consists of atoms with bond pair vectors that are equal in magnitude and

opposite in direction. Centrosymmetry is a per-atom parameter and measures the distortion of the local environment around atoms in a crystal via,

$$P = \sum_{i=1,6} |\mathbf{R_i} + \mathbf{R_{i+6}}|^2 \tag{2.17}$$

where $\mathbf{R_i}$ and $\mathbf{R_{i+6}}$ are bond vectors associated with the six pairs of opposite nearest neighbors in FCC lattice. For a perfect centrosymmetric crystal, bond pairs inside the material are equal in magnitude and in opposite direction, resulting in no distortion in the centrosymmetry parameter $(P = 0)$. On the other hand, atoms located within the distorted regions due to crystal defects and atoms at the free surfaces have a positive centrosymmetry value $(P > 0)$. Even though the concept of the centrosymmetry parameter is easy, it is only useful for centrosymmetric materials. Figure 2.4 shows the formation of stacking faults due to the nucleation of Shockley partial dislocations of FCC single crystals during <100> shock using the centrosymmetry parameter [24]. For <100> shock in a FCC single crystal, the nucleation of Shockley partial dislocations is connected by stacking faults on all {111} close-packed planes, resulting an intersecting pattern for the network of stacking faults, which is shown in Figure 2.4. The atomic planes associated with these stacking faults have centrosymmetry values greater than zero (Figure 2.4).

2.2.2 Common Neighbor Analysis

The common neighbor analysis (CNA)) was developed by Honeycutt and Andersen [25], and is a computational tool to recognize crystal structures in solid materials. To determine the local crystal structure, the CNA algorithm searches the nearest neighbors for atom i within a cutoff

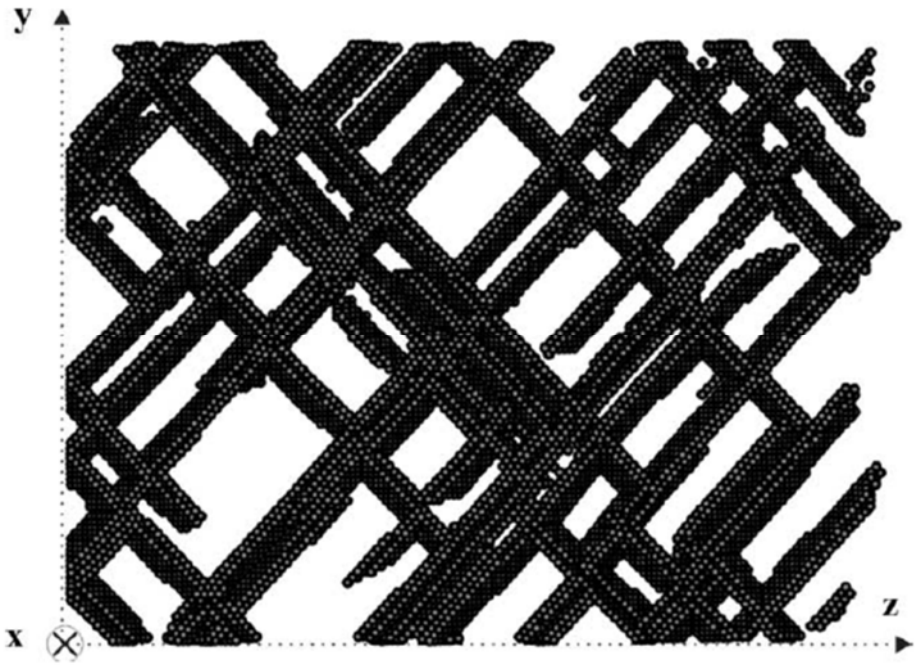

Figure 2.4: Formation of stacking faults due to the nucleation of Shockley partial dislocations of FCC single crystals during <100> shock [24]. This illustration is colored by the centrosymmetry parameter, and all atoms with $(P = 0)$ are deleted.

distance. In addition, it searches the common nearest neighbors between atom i and atom j. Then, the CNA algorithm relates atoms with the same numbers of the nearest neighbors and the common nearest neighbors and same bonding information together as an individual structure. Based on these collected information, the CNA method can identify several structures, including FCC, BCC and HCP crystal structures within the simulation system. For atomistic simulations including several phases, choosing an accurate cutoff distance is challenging; thus, the CNA method with an adaptive cutoff distance [26] will be more suitable. More details related to original version of CNA and adaptive CNA can be found in [25,26]. Figure 2.5 shows dislocation activity and phase transformation for a nanocrystalline Fe model during shock using the CNA method [27]. For shock in a Fe microstructure above a certain strain, the BCC lattice

can transform to the FCC/HCP (close-packed) structures combined with crystal defects. The CNA in Figure 2.5 identifies these close-packed structures as well as the distorted structures associated with defects and grain boundaries.

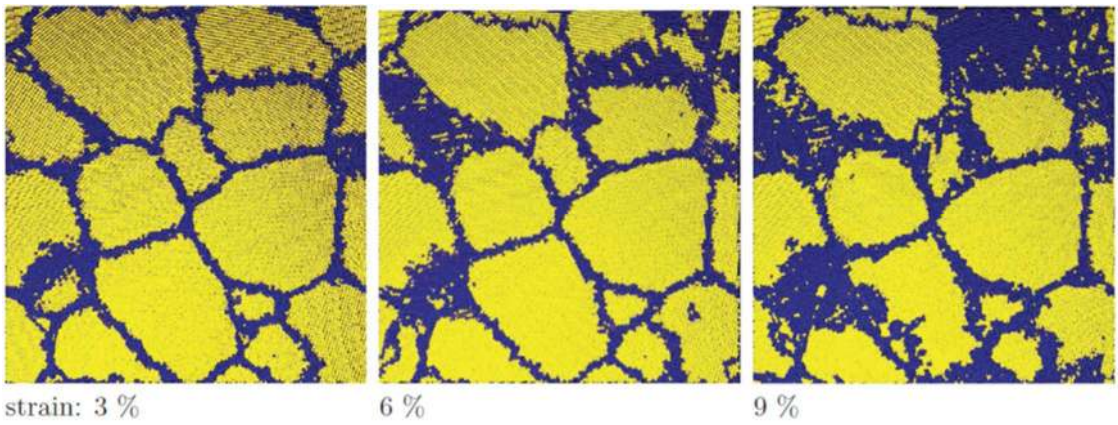

Figure 2.5: Dislocation activity and phase transformation for a nanocrystalline Fe model during shock subjected to different uniaxial strains [27]. Yellow: BCC; blue: other structures, including close-packed structures, grain boundaries and defects identified via the CNA method.

In this research, to identify the atomic fraction of crystal structures behind the shock wave front, the CNA method with an adaptive cutoff distance in OVITO [28] is used. It is important to note that the CNA method may identify an atom as belonging to a given crystal structure even if that atom is under deformation; the effect of this on crystal structure prediction behind the shock wave front will be evaluated in Chapter 4.

2.2.3 Dislocation Extraction Algorithm

The dislocation extraction algorithm (DXA) was developed by Stukowski and Albe [29] to determine the network of dislocation lines within an atomistic simulation. The dislocation

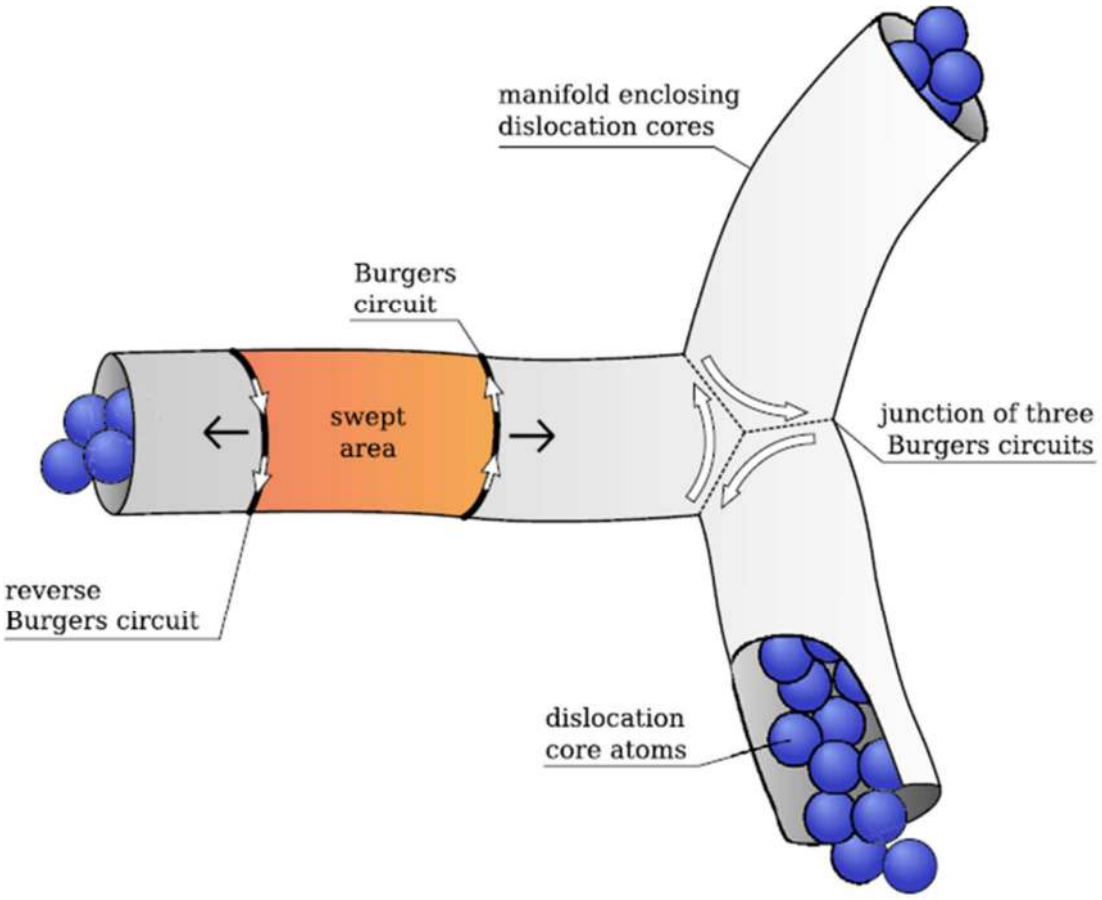

Figure 2.6: Schematic illustration of the DXA method [29].

network extracted by this method satisfies the Burgers vector conservation rule at each node. The DXA method provides the Burgers vector for each dislocation core segment allowing for an analysis of different dislocation types. In addition, the DXA method identifies all other defects, such as grain boundaries and surfaces, as triangulated surfaces. The process of this algorithm includes three steps. Initially, the CNA is used to identify the crystalline atoms and the disordered atoms influenced by defects. Then, a closed manifold is constructed to separate the crystalline atoms from the disordered atoms. Finally, a Burgers circuit is generated for each dislocation segment to obtain the dislocation line and the Burgers vector. The advantage of this

method is the identification of Burgers vector for each extracted dislocation segment. However, the DXA method does not work perfectly for models that include several crystal structures simultaneously, which is the disadvantage of this method. Figure 2.6 shows a schematic illustration of the DXA method.

2.2.4 Simulated (Virtual) Diffraction

The simulated (virtual) diffraction method was developed and implemented in LAMMPS by Coleman et al. [30]. This method is a powerful computational technique to characterize the atomic structure of materials without a priori knowledge of the microstructure. The simulated diffraction method starts with the definition of Bragg's Law:

$$\lambda = 2d\sin(\theta) \tag{2.18}$$

where λ is the x-ray or electron wavelength, d is the distance between two parallel planes in crystal and θ is the angle between incident ray and parallel planes which is shown in Figure 2.7.

The simulated diffraction method creates a three dimensional meshed region of the reciprocal space to calculate the intensity of each point in the reciprocal space. The mesh of reciprocal space is built with the grid size equal to $c_n|\mathbf{A_n}|^{-1}$ along each reciprocal lattice axis of $\mathbf{B_n}$ (n=1,2 and 3). Each reciprocal lattice axis of $\mathbf{B_n}$ is associated with the real space axis $\mathbf{A_n}$. The parameters c_n can control the grid size in reciprocal space and can increase or decrease the resolution of reciprocal space points that is illustrated in Figure 2.8.

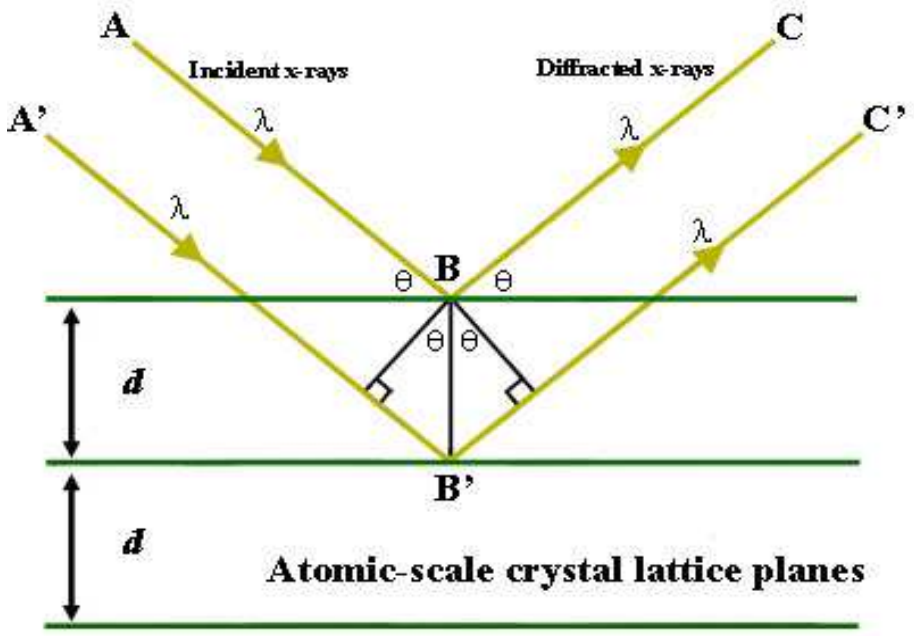

Figure 2.7: Schematic of parallel atomic planes and Bragg's Law [31].

In x-ray diffraction and electron diffraction, each reciprocal space point corresponds to vector **K**, that describes the difference between incident and diffracted wave vectors $\mathbf{K_I}$ and $\mathbf{K_D}$, respectively [30],

$$\mathbf{K} = \mathbf{K_D} - \mathbf{K_I} = \xi\mathbf{B_1} + \eta\mathbf{B_2} + \zeta\mathbf{B_3} \tag{2.19}$$

where ξ, η and ζ can be any real numbers. Based on Bragg's Law in Eq. (2.18), incident wavelength λ, diffraction angle θ and vector **K** are related to each other.

$$\frac{\sin(\theta)}{\lambda} = \frac{|\mathbf{K}|}{2} \tag{2.20}$$

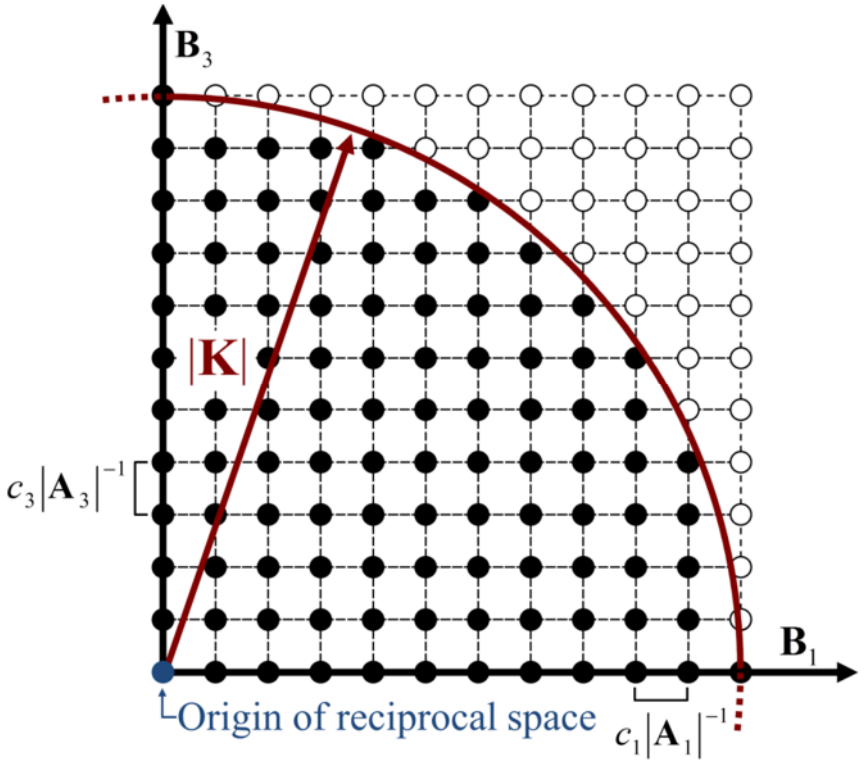

Figure 2.8: Schematic illustration of reciprocal space points [30].

At certain points in reciprocal space, Bragg's law is satisfied ($\mathbf{K} = \mathbf{K_B}$), and the value of vector **K** is related to the interplanar distances d_{hkl} corresponding to {hkl} planes [30].

$$\frac{1}{d_{hkl}} = |\mathbf{K_B}| \tag{2.21}$$

At these points, constructive diffracted waves can be produced.

The density of each reciprocal space point is calculated in different ways for x-ray and electron diffraction. However, both methods need to calculate the structure factor F(K) based on the atomic positions $\mathbf{r_i}$ [30],

$$F(\mathbf{K}) = \sum_{i=1}^{\#atoms} f_i(\theta)\exp(2\pi i \mathbf{K}.\mathbf{r_i}) \tag{2.22}$$

where f_i is the atomic scattering factor, and relates the amplitude of the diffracted wave from each atom with the amplitude of the diffracted wave from electrons of that atom. f_i is a function of diffraction angle θ, wavelength of incident wave λ and atom type.

At each diffraction angle, f_i can be calculated from analytical equations for each type of atoms. For electron diffraction, the scattering factor is approximated via the summation of five Gaussian functions in the form of [30]:

$$f_i\left(\frac{\sin(\theta)}{\lambda}\right) = \sum_{j}^{5} a_j \exp\left(-b_j \frac{\sin^2(\theta)}{\lambda^2}\right) \tag{2.23}$$

For x-ray diffraction, the scattering factor is approximated by the summation of four Gaussian functions in the form of [30]:

$$f_i\left(\frac{\sin(\theta)}{\lambda}\right) = \sum_{j}^{4} a_j \exp\left(-b_j \frac{\sin^2(\theta)}{\lambda^2}\right) + c \tag{2.24}$$

For electron diffraction, the intensity of each point in reciprocal space $I_e(\mathbf{K})$ is calculated by product of the structure factor to its complex conjugate $F^*(\mathbf{K})$, and normalized by the number of atoms N in real space [30].

$$I_e(\mathbf{K}) = \frac{F(\mathbf{K})F^*(\mathbf{K})}{N} \tag{2.25}$$

To calculate the intensity for each reciprocal space points in x-ray diffraction method $I_x(\mathbf{K})$, Lorentz-Polarization factor $Lp(\theta)$ must be applied to control the distribution of reciprocal lattice points and change in intensity when non polarized incident radiation is used. The Lorentz-Polarization factor is calculated by Eq. (2.26),

$$Lp(\theta) = \frac{1 + \cos^2(2\theta)}{\cos(\theta)\sin^2(\theta)} \tag{2.26}$$

and the intensities of reciprocal space points in x-ray diffraction are calculated by Eq. (2.27) [30].

$$I_x(\mathbf{K}) = Lp(\theta)\frac{F(\mathbf{K})F^*(\mathbf{K})}{N} \tag{2.27}$$

The virtual diffraction method does not need a priori knowledge of the microstructure, which is the advantage of this method.

References

[1] "http://www.sv.vt.edu/classes/MSE2094_NoteBook/MolecDyn/lj.html." .

[2] M. Born and T. von Karman, "On vibrations in space lattices," *Phys. Zeitschrift*, vol. 13, p. 297–3.9, 1912.

[3] B. L. Holian and P. S. Lomdahl, "Plasticity Induced by Shock Waves in Nonequilibrium Molecular-Dynamics Simulations," *Science*, vol. 280, no. 5372, pp. 2085–2088, Jun. 1998.

[4] A. Bolesta, L. Zheng, D. Thompson, and T. Sewell, "Molecular dynamics simulations of shock waves using the absorbing boundary condition: A case study of methane," *Phys. Rev. B*, vol. 76, no. 22, p. 224108, Dec. 2007.

[5] A. Kundt and E. Warburg, “Über Reibung und Wärmeleitung verdünnter Gase,” *Ann. Phys.*, pp. 525–550, 1875.

[6] D. E. Spearot, *Atomistic Calculations of Nanoscale Interface Behavior in FCC Metals*. 2005.

[7] S. Plimpton, “Fast Parallel Algorithms for Short-Range Molecular Dynamics,” *J. Comp. Phys.*, vol. 117, no. 1, pp. 1–19, 1995.

[8] W. C. Swope, H. C. Andersen, P. H. Berens, and K. R. Wilson, “A computer simulation method for the calculation of equilibrium constants for the formation of physical clusters of molecules: Application to small water clusters,” *J. Chem. Phys.*, vol. 76, no. 1, pp. 637–649, Jan. 1982.

[9] H. C. Andersen, “Molecular dynamics simulations at constant pressure and/or temperature,” *J. Chem. Phys.*, vol. 72, no. 4, pp. 2384–2393, Feb. 1980.

[10] H. J. C. Berendsen, J. P. M. Postma, W. F. van Gunsteren, A. DiNola, and J. R. Haak, “Molecular dynamics with coupling to an external bath,” *J. Chem. Phys.*, vol. 81, no. 8, pp. 3684–3690, Oct. 1984.

[11] W. Hoover, “Canonical dynamics: Equilibrium phase-space distributions,” *Phys. Rev. A*, vol. 31, pp. 1695–1697, 1985.

[12] S. Melchionna, G. Ciccotti, and B. L. Holian, “Hoover NPT dynamics for systems varying in shape and size,” *Mol. Phys.*, vol. 78, pp. 533–544, 1993.

[13] S. Nosé, “A molecular dynamics method for simulations in the canonical ensemble,” *Mol. Phys.*, vol. 52, pp. 255–268, 1984.

[14] W. Shinoda, M. Shiga, and M. Mikami, “Rapid estimation of elastic constants by molecular dynamics simulation under constant stress,” *Phys. Rev. B*, vol. 69, p. 134103, 2004.

[15] E. Polak and G. Ribière, “Note sur la convergence de méthodes de directions conjuguées,” *Rev. Française d’Informatique Rech. Oper.*, vol. 43, pp. 35–43, 1969.

[16] R. Buckingham, “The classical equation of state of gaseous helium , neon and argon,” *Proc. R. Soc. London Ser. A, Math. Phys. Sci.*, vol. 168, pp. 264–283, 1938.

[17] M. S. Daw and M. I. Baskes, “Embedded-atom method: Derivation and application to impurities, surfaces, and other defects in metals,” *Phys. Rev. B*, vol. 29, no. 12, pp. 6443–6453, Jun. 1984.

[18] Y. M. Mishin, M. Mehl, D. Papaconstantopoulos, A. F. Voter, and J. Kress, “Structural stability and lattice defects in copper: Ab initio, tight-binding, and embedded-atom calculations,” *Phys. Rev. B*, vol. 63, no. 22, p. 224106, May 2001.

[19] M. A. Tschopp, D. E. Spearot, and D. L. McDowell, “Atomistic simulations of homogeneous dislocation nucleation in single crystal copper,” *Model. Simul. Mater. Sci.*

Eng., vol. 15, no. 7, pp. 693–709, Oct. 2007.

[20] E. M. Bringa, J. U. Cazamias, P. Erhart, J. Stölken, N. Tanushev, B. D. Wirth, R. E. Rudd, and M. J. Caturla, "Atomistic shock Hugoniot simulation of single-crystal copper," *J. Appl. Phys.*, vol. 96, no. 7, p. 3793, 2004.

[21] E. M. Bringa, K. Rosolankova, R. E. Rudd, B. A. Remington, J. S. Wark, M. Duchaineau, D. H. Kalantar, J. Hawreliak, and J. Belak, "Shock deformation of face-centred-cubic metals on subnanosecond timescales," *Nat. Mater.*, vol. 5, no. 10, pp. 805–809, Oct. 2006.

[22] A. V. Bolesta and V. M. Fomin, "Phase transition behind a shock front in polycrystalline copper," *Dokl. Phys.*, vol. 59, no. 6, pp. 249–253, Jul. 2014.

[23] C. L. Kelchner, S. J. Plimpton, and J. C. Hamilton, "Dislocation nucleation and defect structure during surface indentation," *Phys. Rev. B*, vol. 58, no. 17, pp. 11085–11088, Nov. 1998.

[24] D. Tanguy, M. Mareschal, T. C. Germann, B. L. Holian, P. S. Lomdahl, and R. Ravelo, "Plasticity induced by a shock wave: large scale molecular dynamics simulations," *Mater. Sci. Eng. A*, vol. 387–389, no. 1–2 SPEC. ISS., pp. 262–265, Dec. 2004.

[25] J. D. Honeycutt and H. C. Andersen, "Molecular dynamics study of melting and freezing of small Lennard-Jones clusters," *J. Phys. Chem.*, vol. 91, no. 19, pp. 4950–4963, Sep. 1987.

[26] A. Stukowski, "Structure identification methods for atomistic simulations of crystalline materials," *Model. Simul. Mater. Sci. Eng.*, vol. 20, no. 4, p. 45021, Jun. 2012.

[27] N. Gunkelmann, E. M. Bringa, K. Kang, G. J. Ackland, C. J. Ruestes, and H. M. Urbassek, "Polycrystalline iron under compression: Plasticity and phase transitions," *Phys. Rev. B*, vol. 86, no. 14, p. 144111, Oct. 2012.

[28] A. Stukowski, "Visualization and analysis of atomistic simulation data with OVITO–the Open Visualization Tool," *Model. Simul. Mater. Sci. Eng.*, vol. 18, no. 1, p. 15012, Jan. 2010.

[29] A. Stukowski and K. Albe, "Extracting dislocations and non-dislocation crystal defects from atomistic simulation data," *Model. Simul. Mater. Sci. Eng.*, vol. 18, no. 8, p. 85001, 2010.

[30] S. P. Coleman, D. E. Spearot, and L. Capolungo, "Virtual diffraction analysis of Ni [0 1 0] symmetric tilt grain boundaries," *Model. Simul. Mater. Sci. Eng.*, vol. 21, no. 5, p. 55020, Jul. 2013.

[31] N. Eby, *Principles of Environmental Geochemistry*. 2004.

Chapter 3: A Molecular Dynamics Study of Dislocation Density Generation and Plastic Relaxation during Shock of Single Crystal Cu

Mehrdad M. Sichani[1] and Douglas E. Spearot[2]

[1] Department of Mechanical Engineering, University of Arkansas, Fayetteville, Arkansas 72701

[2] Department of Mechanical & Aerospace Engineering, University of Florida, Gainesville, Florida 32611

Abstract

The molecular dynamics simulation method is used to investigate the dependence of crystal orientation and shock wave strength on dislocation density evolution in single crystal Cu. Four different shock directions <100>, <110>, <111> and <321> are selected to study the role of crystal orientation on dislocation generation immediately behind the shock front and plastic relaxation as the system reaches the hydrostatic state. Dislocation density evolution is analyzed for particle velocities between the Hugoniot elastic limit (u_{pHEL}) for each orientation up to a maximum of 1.5 km/s. Generally, dislocation density increases with increasing particle velocity for all shock orientations. Plastic relaxation for shock in the <110>, <111> and <321> directions is primarily due to a reduction in the Shockley partial dislocation density. In addition, plastic anisotropy between these orientations is less apparent at particle velocities above 1.1 km/s. In contrast, plastic relaxation is limited for shock in the <100> orientation. This is partially due to the emergence of sessile stair-rod dislocations with Burgers vectors of 1/3<100> and 1/6<110>. The nucleation of 1/6<110> dislocations at lower particle velocities is mainly due to the reaction between Shockley partial dislocations and twin boundaries. On the other hand, for the particle velocities above 1.1 km/s, the nucleation of 1/3<100> dislocations is predominantly due to

reaction between Shockley partial dislocations at stacking fault intersections. Both mechanisms promote greater dislocation densities after relaxation for shock pressures above 34 GPa compared to the other three shock orientations.

3.1 Introduction

When a metallic material is subjected to shock loading above the Hugoniot elastic limit (HEL), many deformation phenomena may occur behind the shock front, including dislocation nucleation [1–4], twinning [5–8], and phase transformations [9–12]. If a shock wave propagates into a perfect single crystal (without preexisting defects and ignoring free surface irregularities) with strength greater than the HEL, defects will nucleate homogeneously resulting in a plastic shock wave [13], and the stress necessary for plastic flow can be considered as an upper limit for polycrystalline samples with the same composition.

Non-equilibrium molecular dynamics (NEMD) simulation is a powerful tool to study the nucleation and propagation of defects in shocked materials with nm length scale and ns time scale resolution [13–15]. For example, Holian and Lomdahl [13] studied plasticity in FCC single crystals subjected to shock in the <100> direction using the Lennard-Jones interatomic potential. They observed nucleation of Shockley partial dislocations connected by stacking faults on all {111} close-packed planes. To explore the orientation dependence of plastic deformation in FCC single crystals, Germann et al. [14,15] studied shock wave propagation in the <100>, <110> and <111> directions and observed elastic precursor waves for shock loading in <111> and <110>. Furthermore, they reported Shockley partial dislocation loops and perfect dislocation loops behind the shock front after shock in the <100> and <111> directions, respectively. To add more

details regarding the dislocation nucleation process behind the shock front in FCC single crystals, Tanguy et al. [16,17] explored the conditions for emission of Shockley partial dislocation loops during shock loading in the <100> direction. They found that loops are nucleated by thermal fluctuations and determined a critical loop diameter above which the loop expands.

Calculation of dislocation density in shocked FCC single crystals is necessary to further quantify the role of lattice orientation and particle velocity on plastic deformation. Several studies have reported dislocation densities during shock loading along specific crystallographic directions in FCC single crystals via analytical [18] and experimental methods [5,19]. Determining an accurate dislocation density during shock experimentally is challenging because a fraction of the dislocations will be relaxed due to the tension waves at the free surfaces and during the recovery process [20]; therefore, simulations are required to give more insights. Bringa et al. [20] performed multimillion atom MD simulations and used a centrosymmetry-based method to calculate dislocation density to study <100> shock in single crystal Cu. They reported dislocation density results at a single particle velocity of 0.75 km/s (slightly above the HEL) for two samples with preexisting dislocation sources (one sample with ramp loading and another with zero rise-time loading). Shehadeh et al. [21] performed multiscale dislocation dynamics plasticity (MDDP) simulations to calculate dislocation density in single crystal Cu during shock in the <100>, <110> and <111> directions including the effects of preexisting dislocation sources (heterogeneous nucleation). They compared the calculated dislocation densities for the three shock directions at a peak pressure of 5 GPa and extended the range of pressure to 100 GPa only for the <100> shock direction. In later work, Shehadeh et al. [22] calculated dislocation density in FCC single crystal Cu during shock in the <100> direction

using the MDDP including effects of homogeneous dislocation nucleation. They explored the pressure range between 30 and 70 GPa and compared their results with multimillion atom MD simulations, where dislocation density behind the shock front was computed with the centrosymmetry-based approach developed by Bringa et al. [20].

There are two important aspects of plastic evolution in shocked metallic materials: (1) the rate of increase in dislocation density immediately behind the shock wave front and (2) the plastic relaxation rate as the system reaches the hydrostatic state. Several experimental researchers have used *in situ* time-resolved x-ray diffraction to study the lattice response behind the shock front in single crystal Si [23], Cu [23] and LiF [24]. For example, Loveridge-Smith et al. [23] reported a fast plastic relaxation to a hydrostatic state for Cu. However, calculated x-ray diffraction profiles based on MD simulations of FCC single crystals during shock revealed a dominant lattice compression in the shock direction (1D) [25]. To resolve this disagreement, Bringa et al. [20] created an extremely long MD model (using 352 million atoms) and subjected it to a shock loading. The extended length allowed sufficient time for plastic relaxation behind the shock front. They found that plastic strain (governed by the Orowan equation, $d\varepsilon_p/dt = \rho_m v_d b$ [26]) initially increases with increasing mobile dislocation density in the dislocation generation regime. Then, it decreases with decrease in both the mobile dislocation density and the dislocation velocity in the plastic relaxation regime. They calculated the plastic strain rate during shock at several times and reported that the system achieves the hydrostatic state in less than 100 ps after the impact in agreement with the MDDP results [22]. In addition, they compared this result with the evolution of the shear stress and observed that the shear stress reaches a nonzero asymptotic value within 100 ps, implying the hydrostatic state. Then, they confirmed the result by calculating the lattice compression at several times using a simulated x-

ray diffraction method. The approach developed by Bringa et al. [20] to study the plastic relaxation requires a very large sample to allow sufficient time for plastic relaxation. In addition, they studied only <100> shock loading and considered only a particle velocity of 0.75 km/s.

The objective of the present work is to determine how dislocation density generation and plastic relaxation in single crystal Cu during shock depend on particle velocity and shock orientation using molecular dynamics simulations. Four different shock directions are selected <100>, <110>, <111> and <321> to study the role of crystal orientation on dislocation density generation and plastic relaxation. Simulations are performed for particle velocities between the Hugoniot elastic limit (u_{pHEL}) for each orientation up to a maximum of 1.5 km/s. Dislocation densities are calculated via the dislocation extraction method (DXA) [27] which is potentially more accurate than the centrosymmetry-based approach used in prior work [20]. Furthermore, the DXA method provides the Burgers vector for each dislocation core segment allowing for an analysis of different dislocation types during shock. An absorbing wall boundary condition is used to provide a sufficient time for the plastic relaxation while avoiding extremely large simulation sizes.

3.2 Methodology

The molecular dynamics method within LAMMPS [28] is used to simulate shock wave propagation and the Hugoniot state (the equilibrium state behind the shock front) in single crystal Cu. The embedded-atom method (EAM) potential for Cu developed by Mishin et al. [29] is used as the interatomic potential. This interatomic potential is fit specifically to the unstable and intrinsic stacking fault energies and has been proven in prior work [30] to provide an accurate prediction of dislocation nucleation and dislocation core structures. Plastic deformation

generation during shock and subsequent relaxation behind the shock front to Hugoniot equilibrium are studied for four different shock orientations: <100>, <110>, <111> and <321>. These four directions are selected because a one-dimensional Schmid Factor analysis implies that they will each deform with a different number of activated slip systems immediately behind the shock front (when the stress state is primarily uniaxial). Table 3.1 presents information related to the simulation cell size for each shock model. The length of the model in the X- and Y-directions is large enough to avoid the influence of the periodic boundary conditions on dislocation generation behind the shock front, following recommendations from prior research [14].

Table 3.1: Physical dimensions and number of atoms for each shock orientation. Shock is applied along the Z-direction of the model.

Shock direction	Number of atoms	X length (nm)	Y length (nm)	Z length (nm)
<100>	4,320,000	21.69	21.69	108.45
<110>	4,233,600	21.69	21.47	107.36
<111>	4,112,640	21.47	21.25	106.44
<321>	5,107,200	23.79	23.43	108.21

Initially, the model is equilibrated to a desired temperature and pressure of 300 K and 1 bar using the constant pressure-temperature (NPT) method and 3D periodic boundary conditions. The two ends of the model in the Z-direction are restricted to be atomically flat planes. Once temperature and pressure equilibrium is achieved, the periodic boundary condition in the Z-direction is removed, exposing free surfaces in this direction. Shock is induced in the Z-direction using the momentum mirror technique [13] under periodic boundary conditions in the X- and Y-directions. Specifically, shock is created by assigning each atom a particle velocity of $-u_p$ in the

Z-direction, impacting the sample with a stationary infinite mass wall. The shock wave is generated in the opposite direction at the interface between the sample and the wall. Because the particle velocity for each atom in the model is applied instantaneously, the rise-time is essentially zero, resulting in a spontaneous peak pressure behind the shock front. At the precise time, the elastic shock wave reaches the opposite end of the sample, and an absorbing wall boundary condition [31] is activated. The simulation continues until convergence in the relaxed dislocation density is attained; as will be shown in the results section, this requires 80 ps, 140 ps, 120 ps and 140 ps for the shock directions of <100>, <110>, <111> and <321>, respectively. After this time, there is no significant change in the state of stress or the dislocation density. The equations of motion are integrated with the velocity-Verlet method with a time step of 1 fs for all simulations.

To study dislocation activity quantitatively, the DXA method [27] in OVITO [32] is used. This method allows for a detailed analysis of dislocation content, including dislocation density differentiated by dislocation character and the Burgers vector of each dislocation segment. This detail enables a critical analysis of the role of lattice orientation on dislocation density evolution during shock and relaxation to the Hugoniot state. All calculations in the present work are repeated three times with different initial Gaussian distributions of atomic velocity (each corresponding to an average 300 K temperature). Mean values of computed shock properties, such as dislocation density, are presented in the results with a description of error based on normalized standard deviation.

3.3 Results and Discussion

Figure 3.1 shows the relationship between the elastic shock wave velocity (u_s) and the particle velocity (u_p) for four different shock orientations and for particle velocities between u_{pHEL} and 1.5 km/s. There is considerable anisotropy of the elastic shock wave velocity as a function of particle velocity for these four shock directions. The highest magnitudes of the elastic shock wave velocity are for the <110> shock orientation because <110> is the close-packed direction in a FCC material and plane-plane collisions result in the fastest shock wave propagation among the orientations, in agreement with Bringa et al. [33]. In contrast, the slowest magnitudes of the elastic shock wave velocity correspond to the <100> shock orientation, with a nearly linear variation of the elastic shock wave velocity as a function of particle velocity.

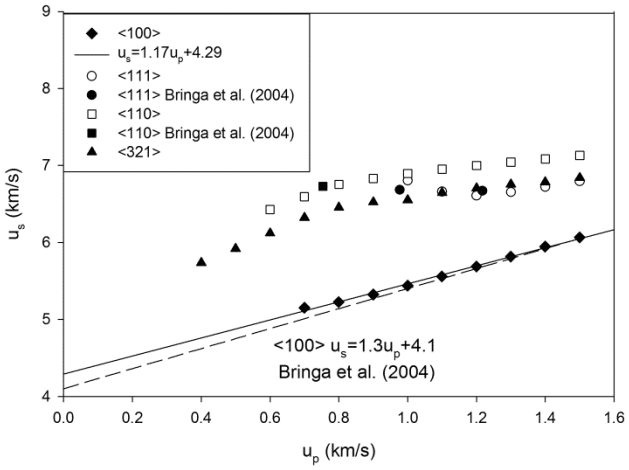

Figure 3.1: Relationship between the elastic shock wave velocity and the particle velocity for four different shock orientations. The results are validated with a previous MD study [33].

Bringa et al. [33] showed for high particle velocities in which the plastic wave overdrives the elastic wave, there is a linear relationship for the Hugoniot curve ($u_s = s_1 u_p + u_0$), where s_1 is a

constant that ranges between 0.5 and 2.5, and $u_0 \approx c_0$ is the bulk speed of sound. For the <100> shock orientation, where the plastic wave is always overdriven, a linear fitting of MD simulation data in this work gives, $u_s = (1.17 \mp 0.03)u_p + (4.29 \mp 0.03)$. When $u_p \to 0$, $u_s \to c_{0L} = 4.3$ km/s [33] (the longitudinal speed of sound in the <100> shock orientation for Cu) in a close agreement with the intercept of the Hugoniot curve in the <100> shock simulations. Note, for uniaxial shock compression of solids, the transverse (shear) component of the sound wave is negligible and the bulk speed of sound can be approximated only by the longitudinal speed of sound, as shown by Holian and Lomdahl [13]. They reported that for shock loading of FCC materials in the <100> direction using a L-J potential, $c_0 = 1.01c_{0L}$. Validating the MD simulation results, the equation for the Hugoniot curve for the <100> shock orientation is in agreement with Bringa et al. [33] using the same interatomic potential ($u_s = (1.3 \mp 0.1)u_p + (4.1 \mp 0.1)$) for the interval $u_p(1,1.5)$ km/s and experiments on polycrystalline Cu [34] ($u_s = (1.5 \mp 0.025)u_p + (3.933 \mp 0.042)$) for particle velocities less than 4.0 km/s. Furthermore, the magnitudes of the elastic shock wave velocity in the <110> and <111> shock orientations are in a reasonable agreement with single data points from a prior MD study [33]. The data for the <321> shock orientation is added to the literature. For each data point, the standard deviation error in the elastic shock wave velocities based upon the independent MD simulations is less than 0.2%.

When a metallic material is subjected to shock above the HEL, dislocations and other defects are nucleated resulting in a plastic wave which propagates through the sample. The HEL is an anisotropic phenomenon in perfect single crystals, and is observed at particle velocities between 0.9-1.0 km/s, 0.5-0.6 km/s, 0.6-0.7 km/s and 0.3-0.4 km/s for the <111>, <110>, <100> and <321> shock orientations, respectively, in the present work. The difference between u_{pHEL}

values for these shock orientations can be justified partially by the Schmid Factor for each orientation, which is 0.272, 0.408, 0.408, and 0.466 for the <111>, <110>, <100> and <321> shock orientations, respectively. However, it is important to note that Schmid Factor alone is not sufficient as a means to predict dislocation nucleation stress in metallic materials when homogeneous nucleation is the dominant mechanism. Ogata et al. [35] showed that stresses normal to the slip plane play a strong role in the magnitude of the dislocation nucleation stress; this was also explored by Spearot et al. [30,36,37] who studied homogeneous dislocation nucleation in single crystals and heterogeneous dislocation nucleation from grain boundaries in FCC metals. Summarizing, stresses normal to the slip plane and stresses within the slip plane perpendicular to the slip direction must also be considered along with the Schmid Factor.

Germann et al. [14] reported the magnitudes of strain at the HEL using a L-J interatomic potential as approximately 15% for a shock loading in the <100> and <111> orientations, and 10% for shock loading in the <110> orientation. These strain magnitudes are close to13.42%, 14.64% and 9.3% for a shock loading in the <100>, <111> and <110> orientations, respectively, in the present work. Furthermore, the u_{pHEL} computed in this work for the <100> and <111> orientations are in a good agreement with previous MD studies with the same EAM potential for a shock in <100> [33] and <111> [38] orientations.

Figure 3.2 shows the difference between the elastic shock wave velocity (u_s) and the plastic shock wave velocity (u_{sp}) as a function of particle velocity between the u_{pHEL} up to a maximum of 1.5 km/s for four shock orientations. An elastic precursor is observed ahead of the plastic wave for shock in the <110>, <111> and <321> orientations in the range of particle velocities studied. The presence of an elastic precursor in the <110> and <111> orientations was reported in previous MD studies using both L-J [14] and EAM interatomic potentials for Cu [33]. For

example, Germann et al. [14] reported that thermally activated dislocation nucleation occurs at a measurable distance behind the shock wave front, resulting in shear stress relief and propagation of plastic flow toward the shock wave front. The presence of the elastic precursor is due to this activation or induction time [14]. Conversely, the plastic wave overdrives the elastic wave for shock loading in the <100> orientation [14,33]. Germann et al. [14] reported that the plastic wave initiates from the elastic shock wave front for shock in the <100> direction, which is in agreement with another MD study [16], and moves as Shockley partial dislocations both toward the piston and with the elastic shock wave front. The nucleation and movement of Shockley partial dislocations provides an immediate relief of shear stress behind the shock wave front [14].

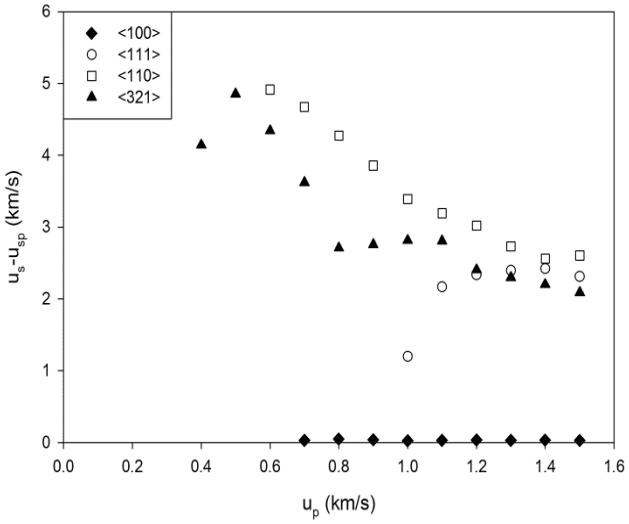

Figure 3.2: Difference between the elastic wave speed and plastic wave speed as a function of particle velocity for four different shock orientations.

Separation between elastic and plastic waves decreases with increasing particle velocity for shock in the <110> and <321> orientations. However, this separation increases with increasing the particle velocity for shock in the <111> orientation until a particle velocity of 1.4 km/s. Interestingly, the separation between the elastic and plastic waves during shock loading in the

<111>, <110> and <321> orientations converges for particle velocities above 1.1 km/s. This is consistent with the observation of less plastic anisotropy for higher particle velocities by Bringa et al. [33]. They reported that the plastic wave speed depends on the bulk modulus, the shear modulus and the plastic modulus (hardening rate), the latter of which depends on loading direction. At higher particle velocities, the hardening response saturates [33], and thus there is less plastic anisotropy. The magnitudes of the plastic shock wave velocity for a shock in the <111>, <110> and <100> orientations are in agreement with available MD data [33] and the data for the <321> is added to the literature. The standard deviation error for most data points in Figure 3.2 is less than 4.0%, with the exception of the first particle velocity above the HEL for each shock orientation, for which the identification of the plastic front is challenging (during the embryonic dislocation nucleation process), and for particle velocities of 0.6 km/s and 0.7 km/s in the <321> shock orientation. For the <321> shock orientation, a sharp increase in the plastic shock wave velocity is observed for particle velocities between 0.5 and 0.8 km/s due to transitions in the plastic deformation process, to be discussed later.

Before the discussion of dislocation density generation and plastic relaxation behind the shock wave front, it is helpful to review the concept of perfect dislocations and Shockley partial dislocations in FCC materials. Dislocations are line defects in crystalline materials, which play a key role in plastic deformations. In FCC materials, dislocation motion occurs on the {111} close-packed planes in the <110> close-packed directions. Figure 3.3(a) schematically shows a perfect edge dislocation in a FCC lattice due to the addition of two atomic half-planes perpendicular to the {111} slip plane [39]. Because the displacement of atoms by a perfect dislocation moves them to identical sites, the motion of perfect dislocations does not change the ABCABC stacking

sequence of atomic planes in <111> direction. Thus, the motion of perfect dislocations in the FCC lattice does not create a stacking fault.

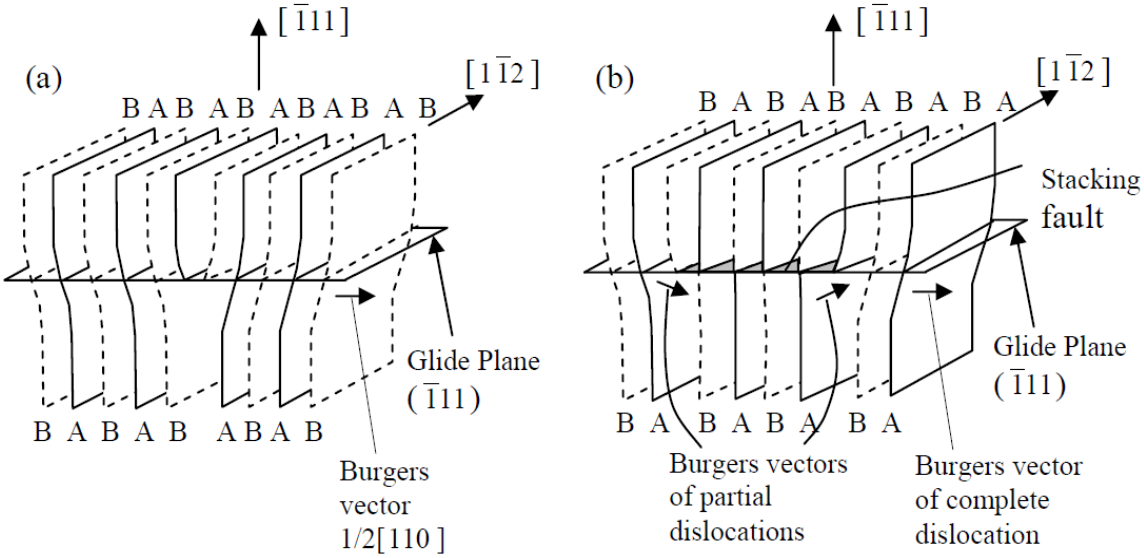

Figure 3.3: Schematic illustration of (a) a perfect dislocation and (b) Shockley partial dislocation in a FCC lattice [39].

Typically, the formation of perfect dislocations in FCC materials is energetically unfavorable and they dissociate into two Shockley partial dislocations, which is shown in Figure 3.3(b). Because the displacement of atoms by Shockley partial dislocations is not a lattice vector (the Burger's vector is of <112> type), a stacking fault is created between the two Shockley partial dislocations (Figure 3.3(b)). This stacking fault in the FCC lattice is identified as HCP structure due to the disordered stacking sequence of {111} planes.

Figure 3.4 shows stacking faults due to the propagation of Shockley partial dislocations on {111} planes at particle velocities immediately above the HEL for four different shock

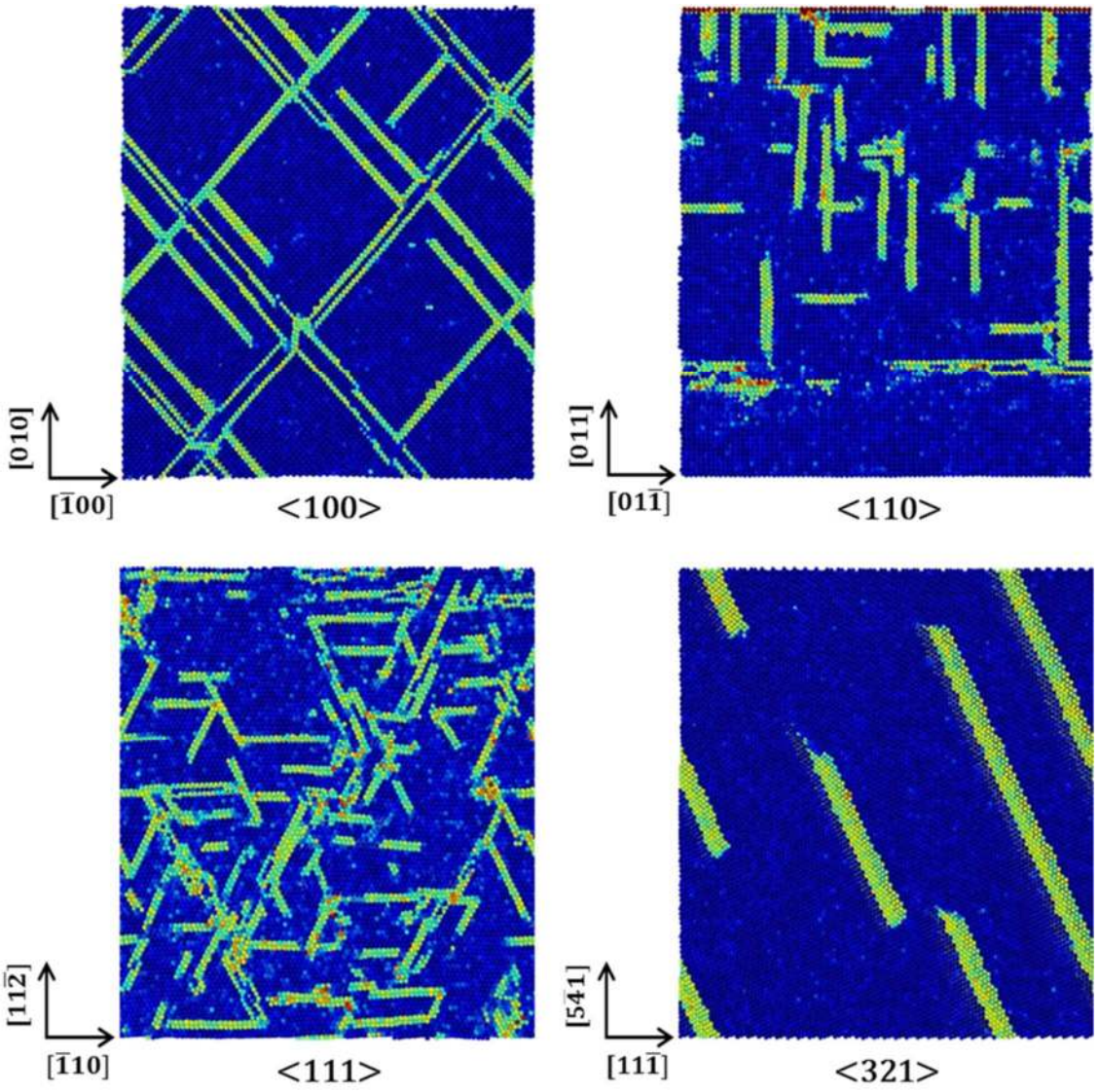

Figure 3.4: Stacking fault patterns colored by the centrosymmetry parameter for four different shock orientations at particle velocities right above the HEL. The viewing axis is parallel to the shock direction for shock in the <100>, <111> and <321> orientations. The viewing axis is the [100] direction for shock in the <110> orientation, which is perpendicular to the shock orientation.

orientations, using the centrosymmetry parameter [40]. The viewing axis for shock in the <111>, <100> and <321> orientations is parallel to the shock direction. Conversely, the viewing axis for shock in the <110> orientation is the [100] direction, which is perpendicular to the shock direction. For shock in the <100> orientation with eight activated slip systems, Shockley partial

dislocation loops are nucleated on four {111} planes behind the shock wave front [13]. Shockley partial dislocation loops above a critical size [16] expand, and pairs of Shockley partial dislocations propagate through the sample behind the shock wave front. Then, these Shockley partial dislocations create stacking faults with a cross-hatch pattern (Figure 3.4), which is consistent with observations in previous MD studies [13,14]. In contrast, there are six activated slip systems on three {111} planes for shock in the <111> orientation, which results in a triangular pattern of stacking faults (Figure 3.4), in agreement with the observation of Germann et al. [14]. For shock in the <110> orientation with four activated slip systems on two {111} planes, the stacking faults are aligned in two potential <110> lattice orientations with the [100] viewing axis, in agreement with a previous MD study [14]. For shock in the <321> orientation, there is one activated slip system at a particle velocity of 0.4 km/s (immediately above the HEL), resulting in a parallel pattern of stacking faults (Figure 3.4). However, for particle velocities between 0.5 and 0.8 km/s, secondary slip systems are activated, leading to a more complicated stacking fault pattern, as shown in Figure 3.5(a). Finally, for particle velocities above 0.8 km/s, several slip systems are activated leading to a triangular stacking fault pattern similar to that of <111> shock loading (Figure 3.5(b)).

Twinning deformation is observed behind the shock wave front for shock in the <100> direction (Figure 3.4) and the <321> direction (Figure 3.5(a)). Several experimental studies have observed twinning after shock of monocrystalline Cu in the <100> [5,6,8,18], <431> [5] and <221> [8] orientations. In addition, Seif et al. [38] observed twining during shock of single crystal Cu in the <100> orientation using MD simulations. In the present work, the twinning deformation is observed behind the shock wave front of single crystal Cu in the <100> shock orientation for the entire range of particle velocities studied. However, the thickness of twin

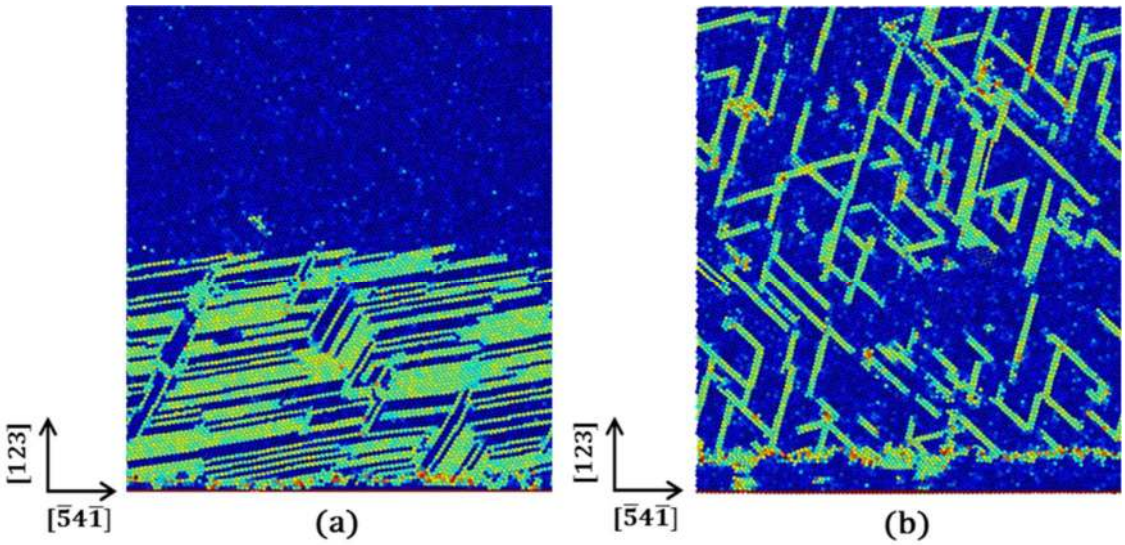

Figure 3.5: Stacking fault pattern behind the shock wave front at t=12 ps (after impact) for shock in the <321> orientation at particle velocities of (a) 0.7 km/s and (b) 1.0 km/s (colored by the centrosymmetry parameter). The viewing axis is perpendicular to the shock direction.

defects decreases for higher particle velocities due to high stacking fault density. For shock in the <321> direction, the twinning deformation is observed for particle velocities between 0.4 and 0.9 km/s (Figure 3.5(a)).

When a metallic material is subjected to shock loading above the HEL, the sample initially undergoes a uniaxial (1D) state of stress; this state of stress evolves during the plastic relaxation regime to reach a hydrostatic state of stress. To quantify plastic relaxation, the DXA method is used to calculate dislocation density. This method is potentially more accurate than centrosymmetry-based methods and can categorize the dislocation segments based on their Burgers vectors. Figure 3.6 shows the evolution of the dislocation density during the plastic relaxation regime for shock in the <321>, <111> and <110> orientations for all types of dislocations (total dislocation density). For shock in the <100> orientation, Figure 3.7 shows both the evolutions of total dislocation density and Shockley partial dislocation density. The

pressure is computed as the average of the virial stress in the X-, Y-, and Z-directions after removing the Z-component of shock wave velocity. The pressures and dislocation densities are calculated over the entire simulation cell based on the current volume of the simulation cell. The time origin is set at the precise time the elastic shock wave reaches the back surface of the sample. The relaxation simulation is run until the difference between the magnitude of the dislocation density and the prior value (at a given pressure) reaches less than 5%, and this convergence criterion is consistent for all shock orientations. The dislocation density takes 140 ps, 120 ps, and 140 ps to converge after applying the absorbing wall boundary condition for a shock in the <321>, <111> and <110> orientations, respectively. For the <100> shock direction, the convergence time for plastic relaxation is approximately 80 ps after applying the absorbing wall boundary condition. This is in agreement with the reported plastic relaxation in less than 100 ps (after impact) for a single particle velocity of 0.75 km/s by Bringa et al. [20].

For shock in the <321>, <111> and <110> orientations, Shockley partial dislocations comprise greater than 70% of the total dislocation density at each particle velocity, and there is no significant difference between the evolutions of total dislocation density and Shockley partial dislocation density. The difference between the maximum dislocation density and the converged dislocation density increases with increasing particle velocity for shock in the <321>, <111> and <110> orientations (Figure 3.6). This difference is more significant than in the <100> shock orientation (Figure 3.7(a)). The dislocation densities at t=20 ps are greater than at time t=0 ps for nearly all particle velocities of shock in the <110> orientation and particle velocities below 1.0 km/s for shock in the <321> orientation. This is due to the existence of an elastic precursor wave with velocity much larger than the plastic wave, and it is consistent with observations in Figure 3.2. The standard deviation error for the points in Figure 3.6 is less than 5.0% except the points

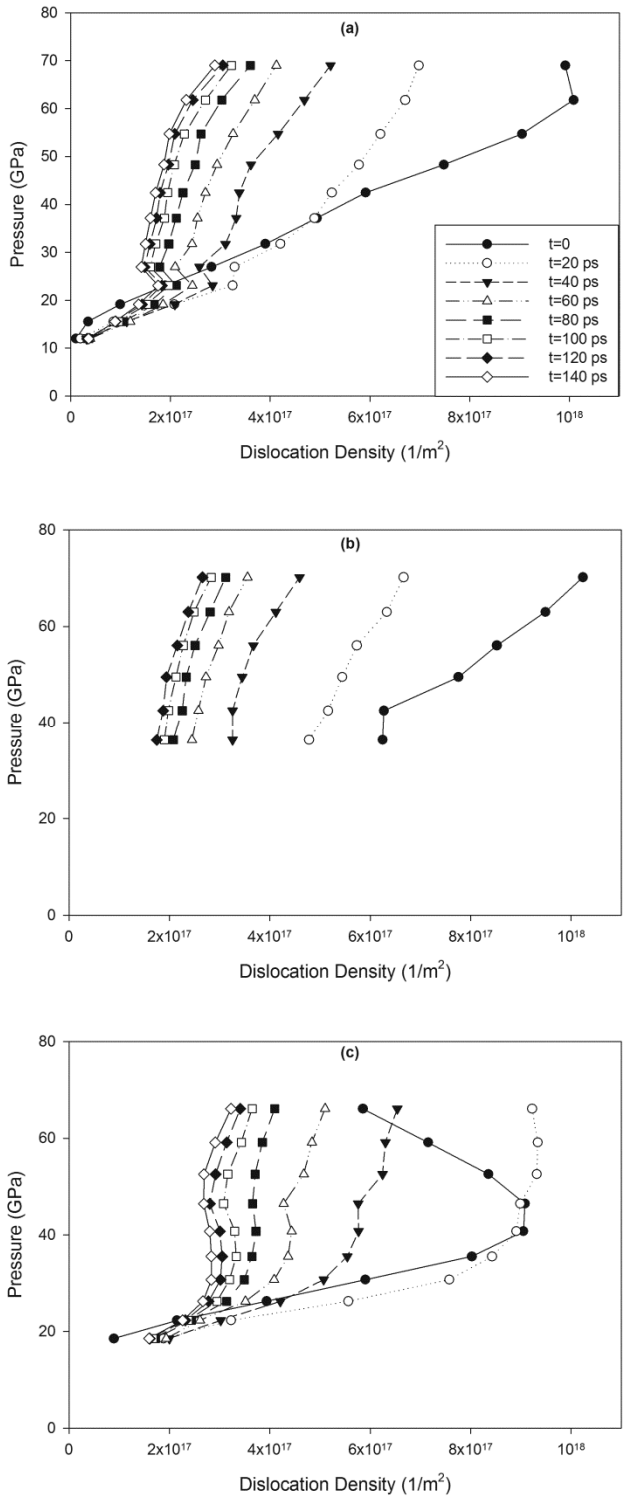

Figure 3.6: Evolution of dislocation density for shock in the (a) <321> (b) <111> and (c) <110> orientations. The time origin is set to the precise time at which the absorbing wall boundary condition is applied.

immediately above the HEL, as discussed previously. The exception to this is for shock in the <321> orientation, points with the particle velocities between 0.4 to 0.8 km/s have a maximum standard deviation error of 20.0% due to twinning (Figure 3.5(a)).

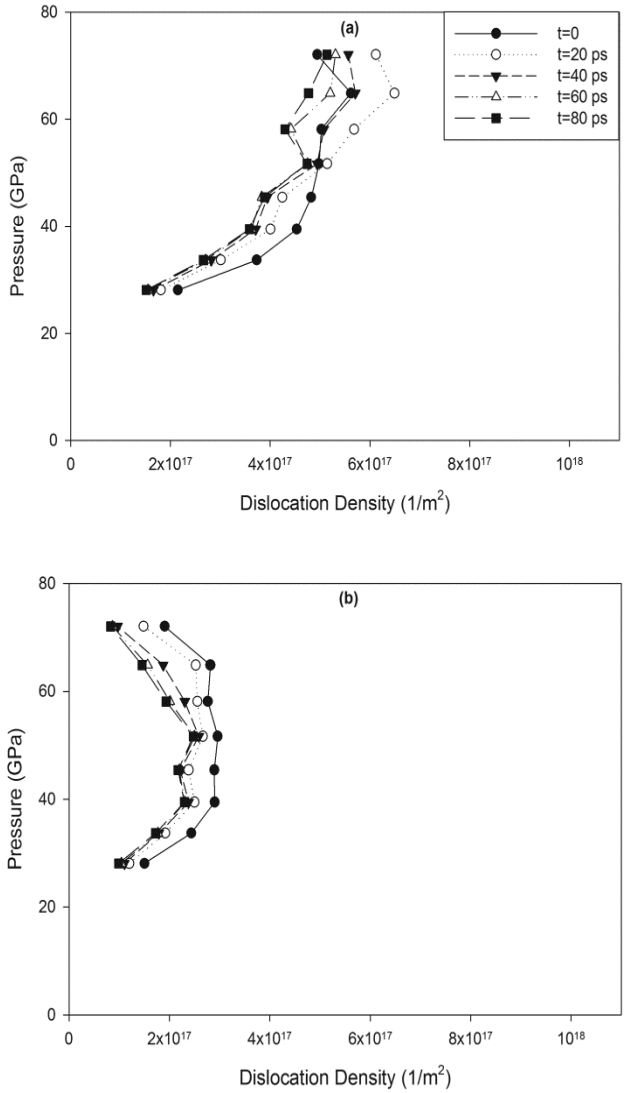

Figure 3.7: Evolution of (a) total dislocation density and (b) Shockley partial dislocation density for shock in the <100> orientation. The time origin is set to the precise time at which the absorbing wall boundary condition is applied.

Even though the total dislocation density generally increases with increasing particle velocity for shock in the <100> orientation (Figure 3.7(a)), the Shockley partial dislocation density reaches a maximum around 1.1 km/s (Figure 3.7(b)). Plastic relaxation occurs for Shockley partial dislocation for the entire range of the particle velocities. In contrast, the magnitude of total dislocation density at 20 ps after the absorbing wall boundary condition is activated is more than at time t=0 ps for the particle velocities higher than 1.1 km/s. Since there is no elastic precursor for <100> shock (Figure 3.2), a different mechanism must be causing this behavior. For <100> shock, the DXA method identifies dislocations with Burgers vectors of 1/3<100> with a higher frequency than other shock orientations. The fraction of this type of dislocation is less than 10% of the total dislocation density for particle velocities less than 1.1 km/s. Then, it increases remarkably and reaches a fraction of approximately 31% at time t=0 ps and 51% at t=80 ps for a particle velocity of 1.4 km/s. Kaiser and Khodos [41] observed edge sessile dislocations with Burgers vectors of 1/6<110> and 1/3<100> at stacking fault intersections due to Shockley partial dislocation reactions during epitaxially growth of cubic SiC films on Si (110). The fraction of stacking faults in the <100> model may be approximated by analyzing the fraction of atoms in a HCP structure. Common neighbor analysis with adaptive cutoff distance [42] identifies 34 at.% HCP structure at t=0 ps and 42 at.% HCP structure at t=80 ps for a particle velocity of 1.1 km/s. HCP structure reaches a fraction of 52 at.% at t=0 ps and 82 at.% at t=80 ps for a particle velocity of 1.4 km/s. Because the fraction of Shockley partial dislocation density decreases for particle velocities higher than 1.1 km/s (Figure 3.7(b)), the nucleation of dislocations with Burgers vector of 1/3<100> is mainly due to reaction of Shockley partial dislocations at the stacking fault intersections, similar to that observed by Kaiser and Khodos [41].

Zhu et al. [43] showed through dislocation reactions that 1/3<100> and 1/6<110> stair-rod dislocations may occur at the intersection of Shockley partial dislocations and twin boundaries, which the DXA method also identifies in the present work. The fraction of dislocations with Burgers vectors of 1/3<100> increases with increasing particle velocity; however, the fraction of 1/6<110> dislocations has a maximum of approximately 8% at a particle velocity of 0.7 km/s, and then decreases to be negligible at a particle velocity of 1.4 km/s. This implies that the nucleation of dislocations with Burgers vectors of 1/6<110> at lower particle velocities is mainly due to the reaction between Shockley partial dislocations and twin boundaries. The 1/3<100> and 1/6<110> dislocations are sessile and thus restrict significant plastic relaxation from occurring. Because of these complicated mechanisms for shock in the <100> orientation, the variation of total dislocation density is greater than other shock orientations. The standard deviation error for the points associated with the particle velocities less than 1.4 km/s is less than 10% except at the highest particle velocity of 1.4 km/s where error reaches a maximum of 16%.

Figure 3.8 shows a comparison between dislocation density after reaching equilibrium for shock of single crystal Cu in the <100> orientation with previous MD data [22], MDDP data [22], analytical data [18] and experimental data [19]. The magnitudes of dislocation density from the experimental study are less than the computational/analytical methods because a fraction of the dislocations are relaxed due to the tension waves at the free surfaces and during the recovery process [20]. The analytical model and the MDDP simulations used dislocation mobilities from experiments at low strain rates [22], and thus the predicted dislocation densities are lower than those predicted by the MD simulations at high strain rates. Interestingly, the present MD approach predicts slightly higher dislocation densities compared to the previous MD data. In the previous MD study, dislocation density was computed using a centrosymmetry range

corresponding to Shockley partial dislocations [22]. Then, it was assumed that all disordered atoms within the selected range are along a dislocation line, separated by the mean atomic separation at the shock pressure [22]. Shehadeh et al. [22] speculated that the calculated dislocation densities would be an upper limit for the partial dislocation densities. In the present study, the DXA method identifies all possible dislocation segments based on their specific Burgers vectors. Consequently, the magnitudes of dislocation density based on the DXA method are more inclusive than the centrosymmetric-based method. For example, at a particle velocity right above the HEL, which the DXA method indicates the fraction of dislocation density due to Shockley partials is approximately 66%, the dislocation densities based on both methods are very close as shown in Figure 3.8. However, at higher particle velocities where the fraction of dislocation density due to Shockley partial dislocations decreases (Figure 3.7(b)), the DXA method predicts greater total dislocation density magnitudes.

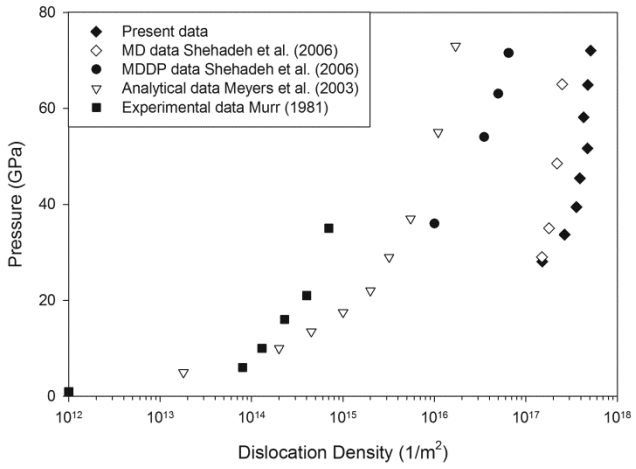

Figure 3.8: Comparison of the total dislocation densities after equilibrium for shock of single crystal Cu in the <100> orientation with previous studies.

Figure 3.9 shows total dislocation density after equilibrium for a shock of single crystal Cu in the <100>, <111>, <110> and <321> orientations. For shock in the <100> orientation, the dislocation densities are larger than the other orientations studied for the shock pressures greater than approximately 34 GPa. This is mainly due to dislocation reactions that occur at the intersection between Shockley partial dislocations and twin boundaries at lower particle velocities, as well as the increase in the fraction of dislocations with Burgers vectors of 1/3<100> at higher particle velocities. For particle velocities above the HEL in the <111> orientation, the dislocation densities are close to the corresponding values for the shock in the <321> orientation due to the similar dislocation structures that are formed in this particle velocity range (Figures 3.4 and 3.5(b)). For the particle velocities above 1.1 km/s, the dislocation density for shock in the <110> converges towards the dislocation densities for shock in the <111> and <321> orientations. This is additional evidence of reduced plastic anisotropy at the higher particle velocities (except <100> shock orientation), which can also be observed in Figure 3.2. There is a sharp increase in the dislocation density between 0.4 and 0.7 km/s for shock in the <321> orientation, in agreement with the sharp increase in the plastic wave velocity within the same range of particle velocities in Figure 3.2.

Finally, in addition dislocation nucleation and twinning, uniaxial compression from the FCC to the BCC crystal structure can occur behind the shock wave front for shock in the <100> orientation (along the Bain path). Bolesta and Fomin [44] recently reported a FCC to BCC structure transformation behind the shock wave front in nanocrystalline Cu using the MD simulations. Providing more depth, Sichani and Spearot [45] explored the role of grain orientation, grain size and particle velocity on compression of FCC Cu into the BCC structure behind the shock wave in nanocrystalline Cu using the MD simulations. In this work, uniaxial

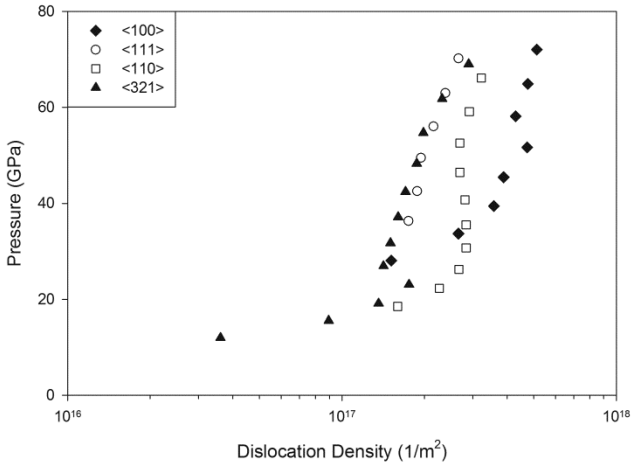

Figure 3.9: Comparison of the dislocation densities after equilibrium for shock of single crystal Cu in the <100>, <111>, <110> and <321> orientations.

compression of FCC Cu to the BCC structure is observed behind the shock wave front, and is most significant at the highest particle velocities studied. For example, data points at a particle velocity of 1.5 km/s are not shown in Figure 3.7, because identification of BCC structure at t=0 ps is strong, complicating the identification of dislocations via DXA. The uniaxially compressed BCC structure behind the shock wave front is energetically unstable and quickly returns to the FCC structure accompanied by defects as the stress state begins to transition from uniaxial to hydrostatic. The role of the FCC to BCC structure compression on the nucleation of dislocations and twinning behind the <100> shock wave front in single crystal Cu is beyond the scope of the present work, and will be the focus of a forthcoming manuscript.

3.4 Conclusions

The molecular dynamics simulation method is used to investigate the role of crystal orientation and shock pressure on the evolution of dislocation density in single crystal Cu. Four different shock directions <100>, <110>, <111> and <321> are selected to study the role of the crystal orientation on dislocation generation immediately behind the shock front and plastic relaxation as the system reaches the hydrostatic state. Simulations are performed for particle velocities between u_{pHEL} to a maximum of 1.5 km/s for these four shock orientations. The DXA method is used to calculate the dislocation density behind the shock wave front, allowing for a detailed investigation based on Burgers vectors of nucleated dislocations. An absorbing wall boundary condition is used to provide a sufficient time for plastic relaxation while avoiding extremely large simulation sizes.

Generally, total dislocation density increases with increasing particle velocity for all shock orientations. Plastic relaxation for shock in <321>, <111> and <110> directions is primarily due to a reduction in Shockley partial dislocation density. In addition, plastic anisotropy is reduced for particle velocities above 1.1 km/s for these three shock orientations. For shock in the <100> orientation, plastic relaxation is limited compared to other three shock orientations. This is partially due to the emergence of sessile stair-rod dislocations with Burgers vectors of 1/6<110> and 1/3<100>. The nucleation of 1/6<110> dislocations at lower particle velocities is mainly due to the reaction between Shockley partial dislocations and twin boundaries. On the other hand, for the particle velocities above 1.1 km/s, the nucleation of 1/3<100> dislocations is predominantly due to reaction between Shockley partial dislocations at the stacking fault intersections. The complicated plastic relaxation behavior for shock in the <100> orientation, results in greater

dislocation densities after relaxation for shock pressures above 34 GPa compared to other three shock orientations.

Acknowledgments

Support of the 21st Century Professorship in Mechanical Engineering and the Department of Mechanical Engineering at the University of Arkansas is greatly appreciated. Simulations in this work were performed on high performance computing equipment supported in part by National Science Foundation grants ARI #0963249, MRI #0959124, EPS #0918970, and a grant from the Arkansas Science and Technology Authority, managed by the University of Arkansas, Arkansas High Performance Computing Center.

References

[1] T. Hatano, "Dislocation nucleation in shocked fcc solids: Effects of temperature and preexisting voids," *Phys. Rev. Lett.*, vol. 93, no. 8, pp. 1–4, 2004.

[2] O. Kum, "Orientation effects in shocked nickel single crystals via molecular dynamics," *J. Appl. Phys.*, vol. 93, no. 6, pp. 3239–3247, 2003.

[3] H. N. Jarmakani, E. M. Bringa, P. Erhart, B. A. Remington, Y. M. Wang, N. Q. Vo, and M. A. Meyers, "Molecular dynamics simulations of shock compression of nickel: From monocrystals to nanocrystals," *Acta Mater.*, vol. 56, no. 19, pp. 5584–5604, Nov. 2008.

[4] B. Cao, E. M. Bringa, and M. A. Meyers, "Shock Compression of Monocrystalline Copper: Atomistic Simulations," *Metall. Mater. Trans. A*, vol. 38, no. 11, pp. 2681–2688, Jul. 2007.

[5] M. S. Schneider, B. K. Kad, M. A. Meyers, F. Gregori, D. Kalantar, and B. A. Remington, "Laser-induced shock compression of copper: Orientation and pressure decay effects," *Metall. Mater. Trans. A*, vol. 35, no. 9, pp. 2633–2646, 2004.

[6] F. Cao, I. J. Beyerlein, F. L. Addessio, B. H. Sencer, C. P. Trujillo, E. K. Cerreta, and G.

T. Gray III, “Orientation dependence of shock-induced twinning and substructures in a copper bicrystal,” *Acta Mater.*, vol. 58, no. 2, pp. 549–559, 2010.

[7] A. M. Podurets, V. A. Raevskii, V. G. Khanzhin, A. I. Lebedev, O. N. Aprelkov, V. V. Igonin, I. N. Kondrokhina, A. N. Balandina, M. I. Tkachenko, J. Petit, and M. A. Zocher, “Twin structures in copper after shock and Shockless high-rate loading,” *Combust. Explos. Shock Waves*, vol. 47, no. 5, pp. 606–614, 2011.

[8] B. Cao, D. H. Lassila, C. Huang, Y. Xu, and M. A. Meyers, “Shock compression of monocrystalline copper: Experiments, characterization, and analysis,” *Mater. Sci. Eng. A*, vol. 527, no. 3, pp. 424–434, 2010.

[9] K. Kadau, F. J. Cherne, R. Ravelo, and T. C. Germann, “Shock-induced phase transformations in gallium single crystals by atomistic methods,” *Phys. Rev. B*, vol. 88, no. 14, p. 144108, Oct. 2013.

[10] A. M. He, P. Wang, J. L. Shao, S. Q. Duan, F. P. Zhao, and S. N. Luo, “Solid-liquid phase transitions in single crystal Cu under shock and release conditions,” *J. Appl. Phys.*, vol. 115, no. 14, p. 143503, Apr. 2014.

[11] N. Gunkelmann, E. M. Bringa, D. R. Tramontina, C. J. Ruestes, M. J. Suggit, A. Higginbotham, J. S. Wark, and H. M. Urbassek, “Shock waves in polycrystalline iron: Plasticity and phase transitions,” *Phys. Rev. B*, vol. 89, no. 14, p. 140102, 2014.

[12] K. Kadau, T. C. Germann, P. S. Lomdahl, R. C. Albers, J. S. Wark, A. Higginbotham, and B. L. Holian, “Shock Waves in Polycrystalline Iron,” *Phys. Rev. Lett.*, vol. 98, no. 13, p. 135701, Mar. 2007.

[13] B. L. Holian and P. S. Lomdahl, “Plasticity Induced by Shock Waves in Nonequilibrium Molecular-Dynamics Simulations,” *Science*, vol. 280, no. 5372, pp. 2085–2088, Jun. 1998.

[14] T. C. Germann, B. L. Holian, P. S. Lomdahl, and R. Ravelo, “Orientation Dependence in Molecular Dynamics Simulations of Shocked Single Crystals,” *Phys. Rev. Lett.*, vol. 84, no. 23, pp. 5351–5354, Jun. 2000.

[15] T. C. Germann, B. L. Holian, P. S. Lomdahl, D. Tanguy, M. Mareschal, and R. Ravelo, “Dislocation structure behind a shock front in fcc perfect crystals: Atomistic simulation results,” *Metall. Mater. Trans. A*, vol. 35, no. 9, pp. 2609–2615, 2004.

[16] D. Tanguy, M. Mareschal, P. S. Lomdahl, T. C. Germann, B. L. Holian, and R. Ravelo, “Dislocation nucleation induced by a shock wave in a perfect crystal: Molecular dynamics simulations and elastic calculations,” *Phys. Rev. B*, vol. 68, no. 14, p. 144111, Oct. 2003.

[17] D. Tanguy, M. Mareschal, T. C. Germann, B. L. Holian, P. S. Lomdahl, and R. Ravelo, “Plasticity induced by a shock wave: large scale molecular dynamics simulations,” *Mater. Sci. Eng. A*, vol. 387–389, no. 1–2 SPEC. ISS., pp. 262–265, Dec. 2004.

[18] M. A. Meyers, F. Gregori, B. K. Kad, M. S. Schneider, D. H. Kalantar, B. A. Remington,

G. Ravichandran, T. Boehly, and J. S. Wark, “Laser-induced shock compression of monocrystalline copper: characterization and analysis,” *Acta Mater.*, vol. 51, no. 5, pp. 1211–1228, Mar. 2003.

[19] L. E. Murr, *Shock Waves and High-Strain-Rate Phenomena in Metals*. New York, 1981.

[20] E. M. Bringa, K. Rosolankova, R. E. Rudd, B. A. Remington, J. S. Wark, M. Duchaineau, D. H. Kalantar, J. Hawreliak, and J. Belak, “Shock deformation of face-centred-cubic metals on subnanosecond timescales,” *Nat. Mater.*, vol. 5, no. 10, pp. 805–809, Oct. 2006.

[21] M. A. Shehadeh, H. M. Zbib, and T. D. De La Rubia, “Multiscale dislocation dynamics simulations of shock compression in copper single crystal,” *Int. J. Plast.*, vol. 21, no. 12, pp. 2369–2390, 2005.

[22] M. A. Shehadeh, E. M. Bringa, H. M. Zbib, J. M. McNaney, and B. A. Remington, “Simulation of shock-induced plasticity including homogeneous and heterogeneous dislocation nucleations,” *Appl. Phys. Lett.*, vol. 89, no. 17, p. 171918, 2006.

[23] A. Loveridge-Smith, A. Allen, J. Belak, T. Boehly, A. Hauer, B. Holian, D. Kalantar, G. Kyrala, R. W. Lee, P. Lomdahl, M. A. Meyers, D. Paisley, S. Pollaine, B. Remington, D. C. Swift, S. Weber, and J. S. Wark, “Anomalous elastic response of silicon to uniaxial shock compression on nanosecond time scales,” *Phys. Rev. Lett.*, vol. 86, no. 11, pp. 2349–2352, 2001.

[24] P. A. Rigg and Y. M. Gupta, “Multiple x-ray diffraction to determine transverse and longitudinal lattice deformation in shocked lithium fluoride,” *Phys. Rev. B*, vol. 63, no. 9, p. 94112, Feb. 2001.

[25] K. Rosolankova, *Shock Compression of Condensed Matter*. New York, 2003.

[26] J. P. Hirth and J. Lothe, *Theory of Dislocations*. New York: Wiley, 1982.

[27] A. Stukowski and K. Albe, “Extracting dislocations and non-dislocation crystal defects from atomistic simulation data,” *Model. Simul. Mater. Sci. Eng.*, vol. 18, no. 8, p. 85001, 2010.

[28] S. Plimpton, “Fast Parallel Algorithms for Short-Range Molecular Dynamics,” *J. Comp. Phys.*, vol. 117, no. 1, pp. 1–19, 1995.

[29] Y. M. Mishin, M. Mehl, D. Papaconstantopoulos, A. F. Voter, and J. Kress, “Structural stability and lattice defects in copper: Ab initio, tight-binding, and embedded-atom calculations,” *Phys. Rev. B*, vol. 63, no. 22, p. 224106, May 2001.

[30] M. A. Tschopp, D. E. Spearot, and D. L. McDowell, “Atomistic simulations of homogeneous dislocation nucleation in single crystal copper,” *Model. Simul. Mater. Sci. Eng.*, vol. 15, no. 7, pp. 693–709, Oct. 2007.

[31] A. Bolesta, L. Zheng, D. Thompson, and T. Sewell, “Molecular dynamics simulations of shock waves using the absorbing boundary condition: A case study of methane,” *Phys.*

Rev. B, vol. 76, no. 22, p. 224108, Dec. 2007.

[32] A. Stukowski, "Visualization and analysis of atomistic simulation data with OVITO–the Open Visualization Tool," *Model. Simul. Mater. Sci. Eng.*, vol. 18, no. 1, p. 15012, Jan. 2010.

[33] E. M. Bringa, J. U. Cazamias, P. Erhart, J. Stölken, N. Tanushev, B. D. Wirth, R. E. Rudd, and M. J. Caturla, "Atomistic shock Hugoniot simulation of single-crystal copper," *J. Appl. Phys.*, vol. 96, no. 7, p. 3793, 2004.

[34] A. C. Mitchell and W. J. Nellis, "Shock compression of aluminum, copper, and tantalum," *J. Appl. Phys.*, vol. 52, no. 5, pp. 3363–3374, 1981.

[35] S. Ogata, J. Li, and S. Yip, "Ideal Pure Shear Strength of Aluminum and Copper," *Science*, vol. 298, no. 5594, pp. 807–811, 2002.

[36] D. E. Spearot, K. I. Jacob, and D. L. McDowell, "Nucleation of dislocations from [001] bicrystal interfaces in aluminum," *Acta Mater.*, vol. 53, no. 13, pp. 3579–3589, Aug. 2005.

[37] D. E. Spearot, M. A. Tschopp, K. I. Jacob, and D. L. McDowell, "Tensile strength of ⟨100⟩ and ⟨110⟩ tilt bicrystal copper interfaces," *Acta Mater.*, vol. 55, no. 2, pp. 705–714, Jan. 2007.

[38] D. Seif, G. Po, R. Crum, V. Gupta, and N. M. Ghoniem, "Shock-induced plasticity and the Hugoniot elastic limit in copper nano films and rods," *J. Appl. Phys.*, vol. 115, no. 5, p. 54301, Feb. 2014.

[39] D. E. Spearot, *Atomistic Calculations of Nanoscale Interface Behavior in FCC Metals*. 2005.

[40] C. L. Kelchner, S. J. Plimpton, and J. C. Hamilton, "Dislocation nucleation and defect structure during surface indentation," *Phys. Rev. B*, vol. 58, no. 17, pp. 11085–11088, Nov. 1998.

[41] U. Kaiser and I. I. Khodos, "On the determination of partial dislocation Burgers vectors in fcc lattices and its application to cubic SiC films," *Philos. Mag. A*, vol. 82, no. 3, pp. 541–551, Feb. 2002.

[42] A. Stukowski, "Structure identification methods for atomistic simulations of crystalline materials," *Model. Simul. Mater. Sci. Eng.*, vol. 20, no. 4, p. 45021, Jun. 2012.

[43] Y. T. Zhu, X. Z. Liao, and X. L. Wu, "Deformation twinning in nanocrystalline materials," *Prog. Mater. Sci.*, vol. 57, no. 1, pp. 1–62, 2012.

[44] A. V. Bolesta and V. M. Fomin, "Phase transition behind a shock front in polycrystalline copper," *Dokl. Phys.*, vol. 59, no. 6, pp. 249–253, Jul. 2014.

[45] M. M. Sichani and D. E. Spearot, "A molecular dynamics study of the role of grain size and orientation on compression of nanocrystalline Cu during shock," *Comput. Mater. Sci.*,

vol. 108, pp. 226–232, 2015.

Appendix 3.1

Copyright and Permission to Reuse AIP Material FAQ

Q: May I include my AIP Publishing article in my thesis or dissertation?

AIP Publishing permits authors to include their published articles in a thesis or dissertation. It is understood that the thesis or dissertation may be published in print and/or electronic form and offered for sale on demand, as well as included in a university's repository. Formal permission from AIP Publishing is not needed. If the university requires written permission, however, we are happy to supply it.

Chapter 4: Assessment of the Embedded-Atom Interatomic Potential and Common Neighbor Analysis for Shock of Single Crystal Cu

Mehrdad M. Sichani[1] and Douglas E. Spearot[2]

[1] Department of Mechanical Engineering, University of Arkansas, Fayetteville, Arkansas 72701

[2] Department of Mechanical & Aerospace Engineering, University of Florida, Gainesville, Florida 32611

Abstract

The molecular dynamics simulation method is used to simulate shock wave propagation along the <100> lattice orientation in single crystal Cu. Shock simulations are performed using particle velocities between 0.5 and 1.7 km/s for samples with initial temperatures of 5, 300 and 600 K. The focus of this work is on the ability of the embedded-atom method (EAM) interatomic potential and common neighbor analysis (CNA) to predict and identify defects and crystal structures that form behind the shock front. Initially, CNA indicates that FCC Cu is uniaxially compressed towards the BCC structure behind the shock wave front; this process is more favorable at higher shock pressures and temperatures. For particle velocities between the Hugoniot elastic limit and 0.9 km/s, CNA indicates that uniaxially compressed Cu quickly relaxes back into a FCC structure with a dislocation and twinning network. However, for particle velocities above 0.9 km/s, CNA indicates that regions of HCP crystal structure nucleate from uniaxially compressed Cu. Free energy calculations of <100> uniaxially compressed Cu and hydrostatically compressed FCC and HCP Cu confirm that for compressions characteristic of particle velocities less than 0.9 km/s, the FCC structure is the lowest energy structure. However, for larger compressions, several EAM potentials predict that the hydrostatically compressed HCP

phase has a lower energy than the FCC phase, with energy difference on the meV level. Thus, the nucleation of HCP Cu from uniaxially compressed Cu for particle velocities above 0.9 km/s is likely an artifact of the EAM interatomic potential.

4.1 Introduction

Important deformation phenomena may occur in metallic materials subjected to shock loading above a critical shock strength, including dislocation generation [1–4], twinning [5–8] and phase transformations [9–12]. Non-equilibrium molecular dynamics (NEMD) simulation is a powerful computational tool to study deformation phenomena with nm length scale and ns time scale resolution, including martensitic (diffusionless) phase transformations in shocked single crystal [9–22] and nanocrystalline [23–26] metallic materials. For example, Kadau et al. [9] reported a BCC to HCP phase transformation in single crystal Fe subjected to <100> shock. They observed nucleation of HCP grains behind the shock wave front above a critical shock strength, resulting in the formation of a phase transformation wave behind the elastic precursor wave for lower particle velocities, and an overdriven phase transformation wave for greater particle velocities. To explore the orientation dependence of phase transformations in shocked single crystal Fe, Kadau et al. [10] studied shock wave propagation in <100>, <110> and <111> directions. They reported that the BCC to HCP/FCC (closed-pack material) phase transformation during <100> shock is a shuffle dominant mechanism; conversely, the phase transformation during <110> and <111> shock included a large shear contribution. Zong et al. [22] studied the HCP (α) to hexagonal (ω) phase transformation in single crystal Ti during shock in the $[0001]$, $[10\bar{1}0]$ and $[12\bar{1}0]$ lattice orientations. For shock loading in $[10\bar{1}0]$ and $[12\bar{1}0]$, they reported

that there is a 90 degree lattice rotation before the phase transformation occurs, caused by a combined shuffle and shear mechanism.

Recently, using NEMD simulations and a structure factor based method to identify crystal structure, Bolesta and Fomin [27] reported a FCC to BCC phase transformation behind the shock wave front in nanocrystalline Cu. Around the same time, Sichani and Spearot [28] used NEMD simulations and the adaptive common neighbor analysis method [29] to study the role of grain orientation, nanocrystalline grain size and particle velocity on uniaxial compression of Cu towards the BCC structure during shock. The stability of the BCC phase of Cu has been debated in the literature. Some researchers have reported that BCC Cu is unstable mechanically [30,31] and energetically [30,32], while other researchers have argued that under specific deformation constraints, BCC Cu can be mechanically [33] and energetically [34,35] stable. For example, Wang and Sob [35] showed that if the FCC to BCC transformation occurs along the trigonal phase transformation path and the lattice is compressed volumetrically, the BCC phase of Cu can be lower energy than the FCC phase. In addition, Mei et al. [33] used ab initio calculations to show that for hydrostatic pressures above 7.5 GPa, the BCC phase of Cu is mechanically stable. Importantly, the combined influence of temperature and pressure on uniaxial compression of Cu towards the BCC structure during shock has not been explored.

More recently, using NEMD simulations and the common neighbor analysis, Wen et al. [36] reported a twinned HCP microstructure behind the <100> shock wave front in single crystal Cu above 75 GPa pressure. However, to the best knowledge of the authors, there is no experimental evidence for stable formation of HCP structure in single crystal or polycrystalline Cu during shock. For example, Murphy et al. [37] performed <100> shock experiments for Cu up to 100

GPa pressure and did not observe a twinned HCP microstructure in their post shock analysis. Thus, the objective of this work is to assess the ability of the embedded-atom method (EAM) interatomic potential to predict defects and phase transformations behind the shock front at high shock pressures. In addition, the ability of the common neighbor analysis (CNA) method with adaptive cutoff distance to identify crystal structures behind the shock front is assessed. Molecular dynamics simulations of <100> shock in single crystal Cu are performed for particle velocities from 0.5 to 1.7 km/s, and initial sample temperatures of 5, 300 and 600 K. To explain the observation of different Cu crystal structures that dynamically form during shock and remain at the Hugoniot state (the equilibrium state behind the shock wave front), free energy calculations are also employed in this study.

4.2 Methodology

The molecular dynamics method within LAMMPS [38] is used to simulate <100> shock wave propagation and the Hugoniot state in single crystal Cu. Primarily, the embedded-atom method potential for Cu developed by Mishin et al. [39] is used as the interatomic potential. This interatomic potential has been shown in prior shock studies to accurately capture the Hugoniot curve (the relationship between shock velocity and particle velocity) [40], dislocation generation/relaxation in single crystal Cu [4,41] and uniaxial compression of FCC Cu towards the BCC structure in nanocrystalline Cu [27,28]. The ability of this interatomic potential (and others) to predict crystal structures behind the shock front at high shock pressures will be evaluated in the result section. Single crystal Cu models have lengths of 21.69, 21.69 and 108.45 nm in the X-, Y- and Z-directions, respectively, containing 4,320,000 atoms. The simulations are

performed for initial temperatures of 5, 300 and 600 K and employ particle velocities between 0.5 to 1.7 km/s. Detailed information regarding boundary conditions, simulation equilibration and simulation validation can be found in Chapter 3. Briefly, shock is created via a momentum mirror technique [1] and at the precise time the shock wave reaches the end of the model, an absorbing wall boundary condition[42] is applied, and the simulation continues for an additional 100 ps to reach the Hugoniot state. Simulations are performed three independent times for each combination of particle velocity and initial temperature, using different random seeds to create the Gaussian velocity distribution associated with the given initial temperature.

The common neighbor analysis [43] is a computational tool to recognize crystal structures in solid materials. To determine the local crystal structure, the CNA algorithm searches the nearest neighbors of each atom within a cutoff distance. In this work, to identify the atomic fraction of crystal structures behind the shock wave front, the CNA method with an adaptive cutoff distance [29] in OVITO [44] is used, which is more suitable for multi-phase systems than a fixed cutoff distance [29]. The adaptive CNA method has been used in prior shock studies [23,28,36,45]. It is important to note that the CNA method may identify an atom as belonging to a given crystal structure even if that atom is under deformation; the effect of this on crystal structure prediction behind the shock wave front will be evaluated in this work. All CNA based calculations in this study are averages over three independent simulations at each combination of initial temperature and particle velocity. Mean values of the structure fractions behind the shock wave front are presented for all data, with error bars for data at the Hugoniot state based on normalized standard deviation.

4.3 Results and Discussion

Figure 4.1 shows the relationship between temperature and pressure at the Hugoniot state for particle velocities from 0.5 to 1.7 km/s and three different initial model temperatures. The temperatures are computed after removing the Z-component of the velocity (the velocity in the direction of the shock loading). The pressures are computed as the average of the virial stress in the X-, Y-, and Z-directions after removing the Z-component of the shock wave velocity. There is no significant difference between the pressures at the Hugoniot state for samples with the same particle velocity and three different initial temperatures; the maximum relative pressure difference is 4.8%. Generally, the Hugoniot pressures at a given particle velocity increase modestly with decreasing initial temperature. At higher temperatures, more dislocation annihilation and plastic relaxation is expected leading to this result.

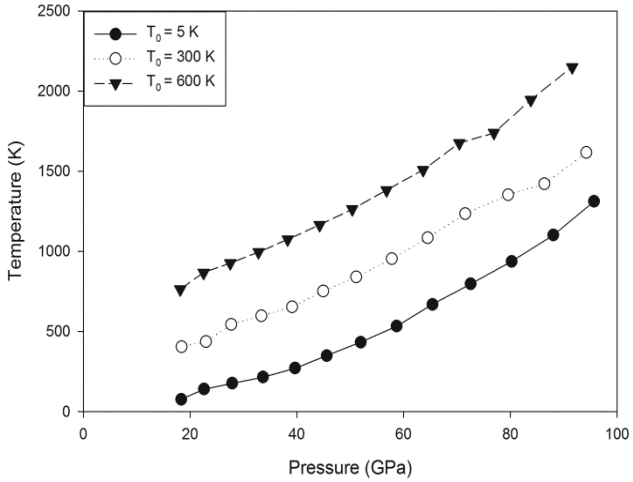

Figure 4.1: Relationship between temperature and pressure at the Hugoniot state for initial temperatures of 5, 300 and 600 K and particle velocities from 0.5 to 1.7 km/s.

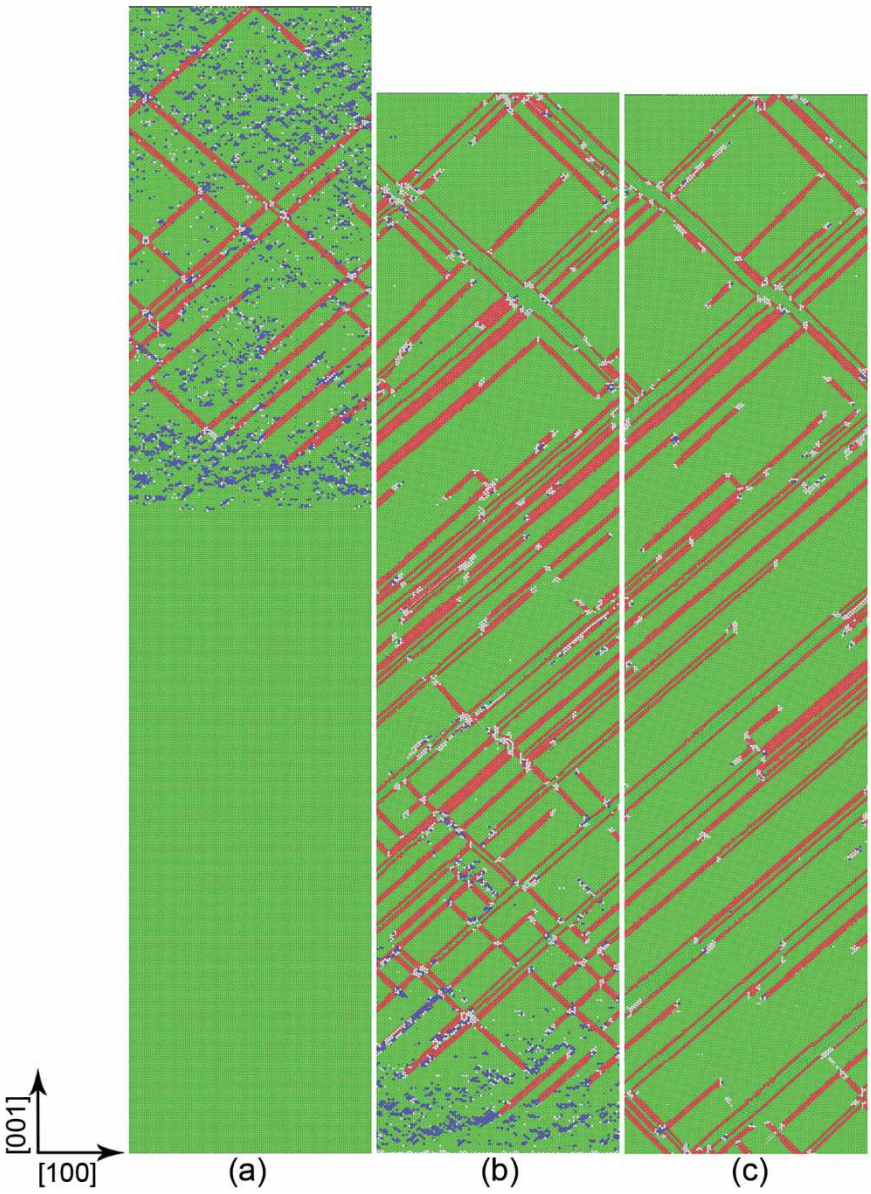

Figure 4.2: Evolution of defects behind the shock wave front for a model with initial temperature of 300 K and particle velocity of 0.7 km/s. Figures (a) to (c) correspond to t=10 ps (after impact), and t=0 ps and t=100 ps (after applying the absorbing wall boundary condition), respectively. The FCC, HCP, BCC and unidentified structures are colored by green, red, blue and white, respectively.

For particle velocities between the Hugoniot elastic limit and 0.9 km/s, the deformation response is dominated by dislocation plasticity and twinning, in agreement with recent studies [4,36,41]; an example of this is shown in Figure 4.2 for a particle velocity of 0.7 km/s and an initial temperature of 300 K. The FCC lattice is uniaxially compressed towards the BCC structure behind the shock wave front, identified via adaptive CNA, and quickly relaxes into a faulted FCC crystal, including stacking faults and twin boundaries. The intersecting configuration of stacking faults is due to the generation of Shockley partial dislocations on four {111} close-packed planes and the growth of twins, as discussed in detail in prior work by Sichani and Spearot [4]. The Hugoniot elastic limit (HEL), above which generation of dislocations and other defects is observed, occurs between particle velocities of 0.6 and 0.7 km/s for <100> shock of single crystal Cu at initial temperatures of 300 and 600 K. The HEL occurs at a particle velocity of 0.5 km/s in the model with an initial temperature of 5 K. From Figure 4.2(c), the fraction of atoms identified as HCP structure at the Hugoniot state is less than that at the precise time of applying the absorbing wall boundary condition (Figure 4.2(b)). This is due to plastic relaxation of defects in the model, which leads to a reduction in dislocation density as confirmed previously by Sichani and Spearot [4].

Figure 4.3 shows the computed FCC, HCP and BCC atomic fractions behind the shock wave front for three different initial temperatures and for different particle velocities; these atomic fractions are calculated using the adaptive CNA over the volume of shocked material only. The atomic fraction of unidentified structure is not shown in Figure 4.3. Generally, unidentified structure is a small fraction of the data; for example, the atomic percentage of unidentified structure for a model with a particle velocity of 1.0 km/s and an initial temperature of 300 K at the Hugoniot state is 6.0 at.%. The time origin for the data in Figure 4.3 is set at the initiation of

the shock wave via the infinite mass wall. The Hugoniot state data corresponds to the equilibrium that is achieved at 100 ps after the absorbing wall boundary conditions is activated, where convergence is observed in the CNA data. This convergence time was confirmed in a previous study [4] and is in agreement with Bringa et al. [46] using an extremely large MD model.

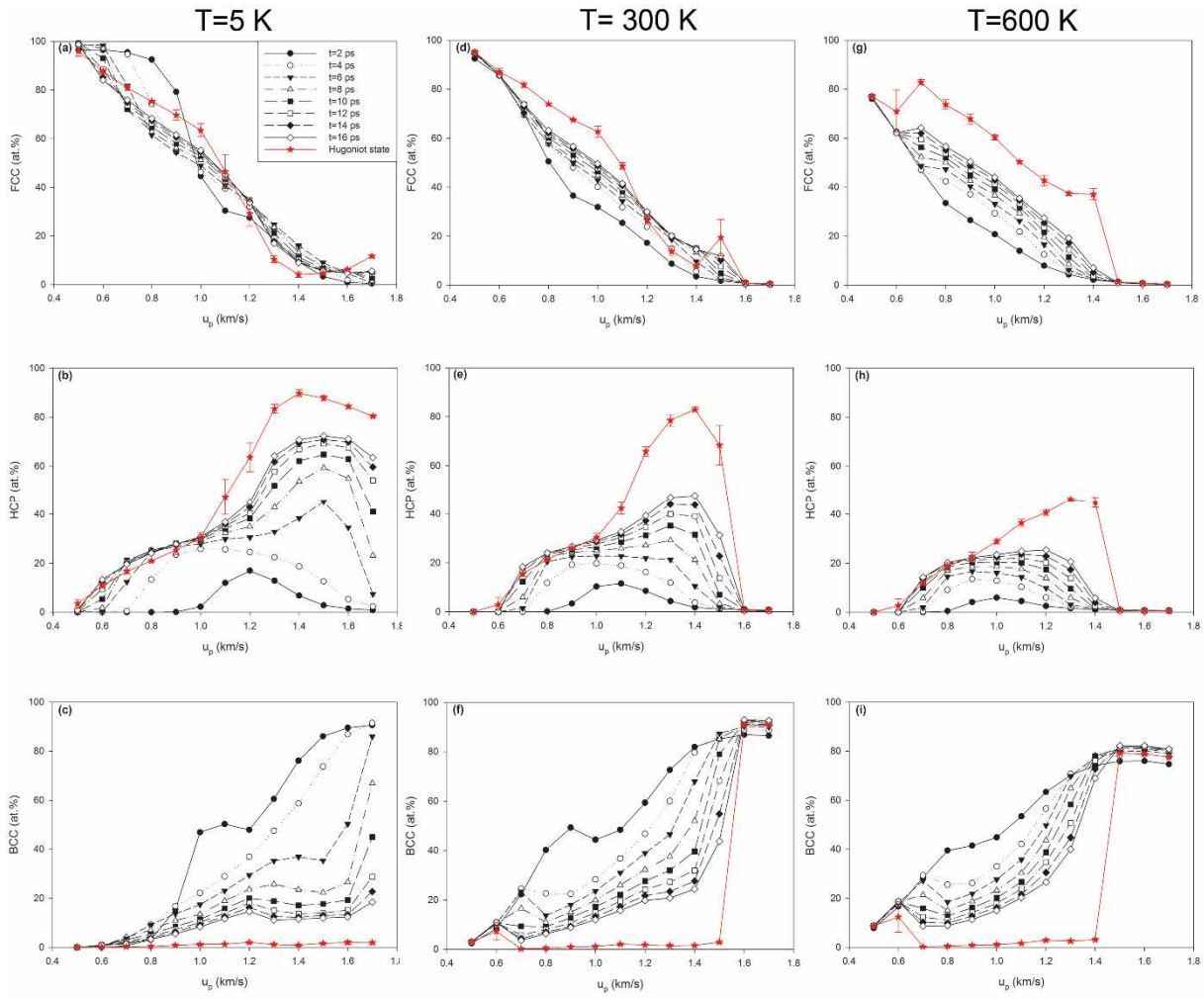

Figure 4.3: Evolution of atomic fractions of FCC, HCP and BCC structures for particle velocities from 0.5 to 1.7 km/s. The error bars are based on the normalized standard deviation and they are shown only for the Hugoniot state (red stars).

Before conclusions are drawn from Figure 4.3, the capability of adaptive CNA for identification of local atomic structure behind the shock wave front must be assessed. Additional calculations are performed where a small FCC Cu model (10 x 10 x 10 unit cells) is uniaxially compressed at 0 K along the [001] crystal orientation (c-axis) with zero strain in [100] and [010] orientations (a-axis). Adaptive CNA method identifies the uniaxially compressed structure as FCC until a compression of c/a=0.79 with an atomic volume of 9.32 Å^3/atom, and then identifies atoms in the structure as BCC with continued compression. Note, perfect BCC Cu structure is achieved at c/a=0.7 and atomic volume of 8.35 Å^3/atom, in agreement with Bain path [39]. This confirms that the CNA method may identify an atom as belonging to a cubic crystal structure even if that atom is under deformation. The process of uniaxial compression is reversible as a structure starting in BCC is identified as BCC structure until it is stretched to an atomic volume of 9.32 Å^3/atom.

Returning to Figure 4.3, at particle velocities from 0.5 to 0.7 km/s, the competition between elastic compression and dislocation activity (identified via HCP structure from stacking faults) is temperature dependent. The fraction of structure identified as BCC for a model with an initial temperature of 5 K and particle velocity of 0.5 km/s is 0.0 at.% at the Hugoniot state (Figure 4.3(c)). On the other hand, the fraction of structure identified as BCC for models with initial temperatures of 300 and 600 K at a particle velocity of 0.5 km/s is 3.0 and 8.7 at.% at the Hugoniot state (Figures 4.3(f) and 4.3(i)), respectively. The elastic compression is a temperature dependent phenomenon, and is preferential at higher temperatures. Thus, compression of the lattice towards the BCC structure for models with initial temperatures of 300 and 600 K at particle velocity of 0.5 km/s is more prominent, delaying dislocation nucleation and promoting a higher HEL (which occurs at 0.5 km/s for the model with initial temperature of 5 K). For a

particle velocity of 0.6 km/s, during the embryonic dislocation nucleation process, the fraction of structure identified as BCC is 7.2 and 12.4 at.% at the Hugoniot state for models with initial temperatures of 300 and 600 K, respectively. At this particle velocity, dislocation nucleation is not significant yet, and elastic compression is the primary deformation mechanism. For particle velocity of 0.7 km/s (above the HEL), dislocation nucleation mechanisms are preferential to lattice compression, leading to a significant drop in BCC identification (0.2 at.%) at the Hugoniot state for models with initial temperatures of 300 and 600 K.

The observation of higher levels of elastic uniaxial compression at higher initial temperatures remains valid at higher particle velocities. For example, CNA predicts 11.5, 24.3 and 68.9 at.% BCC structure at a particle velocity of 1.4 km/s at t=16 ps (before applying the absorbing wall boundary condition) for initial temperatures of 5, 300 and 600 K, respectively (Figure 4.3). Similarly, the elastic compression Cu towards the BCC structure is more favorable at higher uniaxial strains (higher shock pressures). For example, CNA predicts 15.7, 24.3 and 92.5 at.% BCC structure at an initial temperature of 300 K at t=16 ps and particle velocities of 1.1, 1.4 and 1.7 km/s, respectively (Figure 4.3). However, the uniaxially compressed Cu does not relax back into FCC and HCP structures, and remains at the Hugoniot state at initial temperatures of 600 and 300 K and particle velocities greater than 1.4 and 1.5 km/s (Figure 4.3), respectively. This implies the preference for the elastic compression at higher temperatures and uniaxial strains. Figure 4.4(a) shows that the uniaxial compression of Cu at the Hugoniot state at a particle velocity of 1.6 km/s and initial temperature of 600 K is less than atomic volume of 9.32 $Å^3$/atom leading to BCC identification. Figures 4.4(b) and 4.4(c) show the crystal structure of models at the Hugoniot state and initial temperature of 5K at particle velocities of 1.1 and 1.6 km/s, respectively. In Figure 4.4(b), the crystal structure includes a combination of FCC (accompanied

by stacking faults) and HCP structures. In Figure 4.4(c), the crystal structure is predominantly HCP according to CNA; the explanation of this observation will be discussed in following paragraphs.

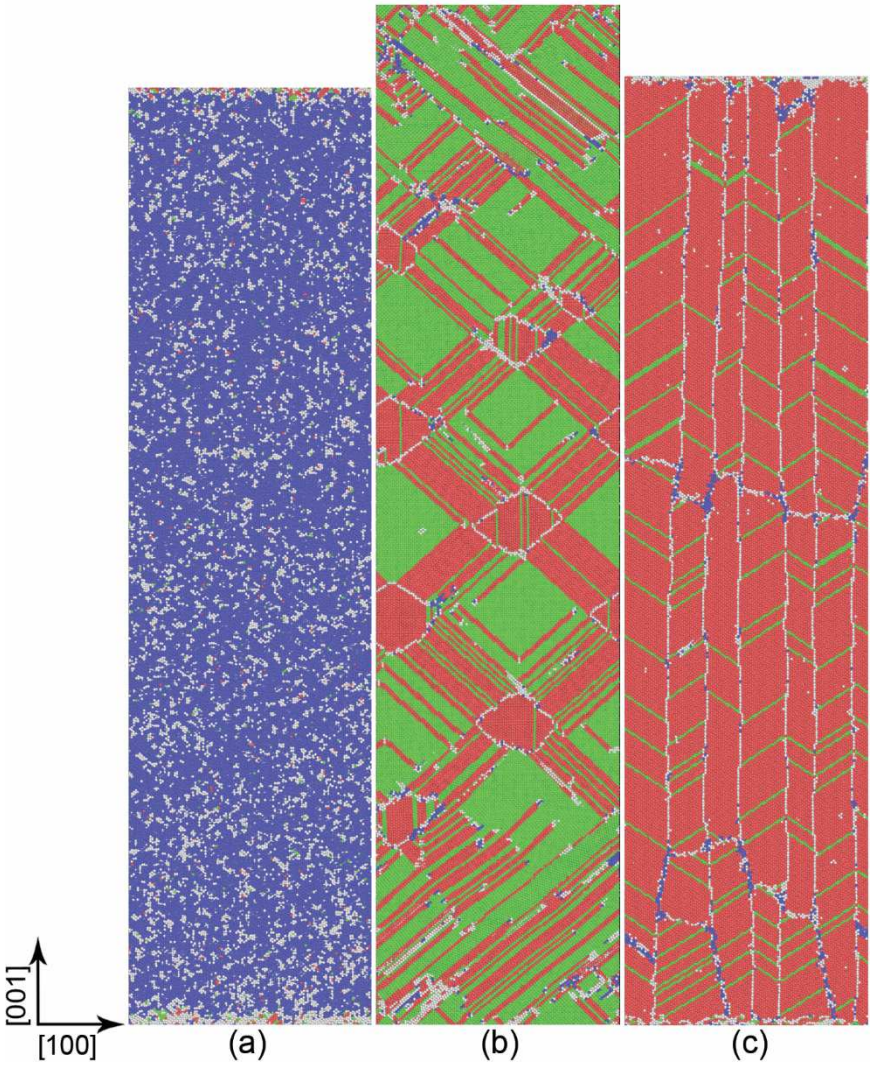

Figure 4.4: Crystal structures predicted by CNA at the Hugoniot state of shock. Figure (a) corresponds to a model with initial temperature of 600 K and particle velocity of 1.6 km/s. Figures (b) and (c) correspond to models with initial temperature of 5 K and particle velocities of 1.1 and 1.6 km/s, respectively. The FCC, HCP, BCC and unidentified structures are colored by green, red, blue and white, respectively.

For particle velocities above 0.9 km/s, the FCC lattice is initially compressed towards the BCC structure at all temperatures; the compressed Cu subsequently relaxes into closed-packed HCP and FCC structures accompanied by stacking faults. CNA identifies that the atomic fraction of HCP structure at the Hugoniot state is greater than that at t=16 ps for particle velocities above 0.9 km/s (Figures 4.3(b), 4.3(e) and 4.3(h)). This implies that there is a fraction of HCP structure created which is not due to generation of Shockley partial dislocations and stacking faults. Sichani and Spearot [4] reported that the dislocation density associated with Shockley partial dislocations decreases after a particle velocity of 1.1 km/s for <100> shock of Cu during plastic relaxation. Instead, HCP clusters are nucleated from the elastically compressed Cu for particle velocities above 0.9 km/s.

Even though the transformation of BCC to HCP Cu under the right conditions is possible, a comprehensive assessment is required to justify the formation and growth of HCP Cu within the elastically compressed region during <100> shock of single crystal Cu. Some researchers have reported phase transformation of BCC to HCP Cu numerically [47] and experimentally [48]. For example, Wormeester et al. [48] observed a BCC to HCP structure transformation during epitaxial growth of Cu on W (100), and reported that larger volume fractions of the HCP phase are created at lower substrate temperatures. Motivated by the HCP structure observed in experiments, Jona et al. [49] used first-principles calculations to explore phase transformation pathways leading to HCP Cu. Confirming the epitaxy experiments, Jona et al. [49] showed that the HCP structure could be stabilized through lattice confinement. Using MD simulations, Xie et al. [47] reported FCC to BCC and BCC to HCP phase transformations in Cu nanowires under uniaxial tension at high strain rates and low temperatures. In addition, Togo and Tanaka [50] showed via first principles calculations that under the right pathway, BCC Cu can transform to

the HCP structure. However, to date, no experimental study performed using the same shock strengths [37] has shown large regions of HCP material behavior, as shown in Figures 4.4(b) and 4.4(c). Thus, the observation of HCP during shock is either a metastable phenomenon unique to loading conditions in MD simulations, or an artifact of the EAM potential.

To assess the validity of the HCP dominant structure that appears during <100> shock of single crystal Cu, free energy calculations are performed. Figure 4.5 shows free energies of Cu during <100> uniaxial compression of Cu and hydrostatic compression of FCC and HCP Cu at 0 K. For uniaxial <100> compression, starting from the FCC structure, the model is compressed in [001] crystal orientation (c-axis) with zero strain in [100] and [010] orientations (a-axis). The procedure is similar to tetragonal path (Bain path) described in previous study [39], but the volume of model is not conserved in the <100> uniaxial compression path. This path is expected to be analogous to the strain state during <100> shock in single crystal Cu (without considering the temperature effects). During uniaxial <100> compression, CNA identifies the crystal structure starting at BCC Cu at c/a=0.79 corresponding to atomic volume of 9.32 $Å^3$/atom, which is comparable with emergence of BCC structure at c/a=0.7 during Bain path [39].

The free energy calculations in Figure 4.5 show that uniaxially compressed Cu can relax to lower energy FCC or HCP structures as the stress state evolves to hydrostatic compression at Hugoniot equilibrium. The free energies of hydrostatically compressed FCC and HCP structures in Figure 4.5 are very similar. Thus, Figure 4.6 shows the difference between free energies of hydrostatically compressed FCC and HCP structures with meV precision. The cohesive energy of FCC Cu is lower than the HCP structure at the equilibrium state (atomic volume=11.81 $Å^3$/atom), which is in agreement with the validation provided in the original publication of the

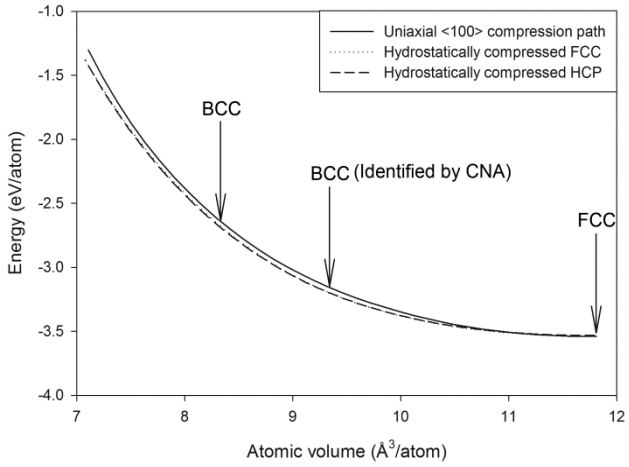

Figure 4.5: Comparison of free energies for the uniaxial <100> compression path, hydrostatically compressed FCC Cu and hydrostatically compressed HCP Cu. In the uniaxial <100> compression path, starting from the FCC structure at atomic volume of 11.81 Å3/atom, CNA identifies the structure as BCC starting at an atomic volume of 9.32 Å3/atom. Upon continued compression, perfect BCC Cu is achieved at atomic volume of 8.35 Å3/atom.

interatomic potential [39], and this trend continues until atomic volume of approximately 9.4 Å^3/atom. However, for atomic volumes range between 6.6 and 9.4 Å^3/atom, HCP structure is predicted to have a lower energy than the FCC structure of Cu (Figure 4.6). Two other EAM interatomic potentials [51,52] are assessed (Figure 4.6), and results are in agreement. This means the observation of HCP structure as a lower energy structure in this range of hydrostatic compressions at 0 K temperature is likely an artifact of the EAM formulation.

Connecting these free energy calculation results to the shock simulation observations, <100> shock particle velocities of 0.9 km/s and below create a compression at the Hugoniot state that results in atomic volumes greater than 9.85 Å^3/atom. Free energy calculations show that

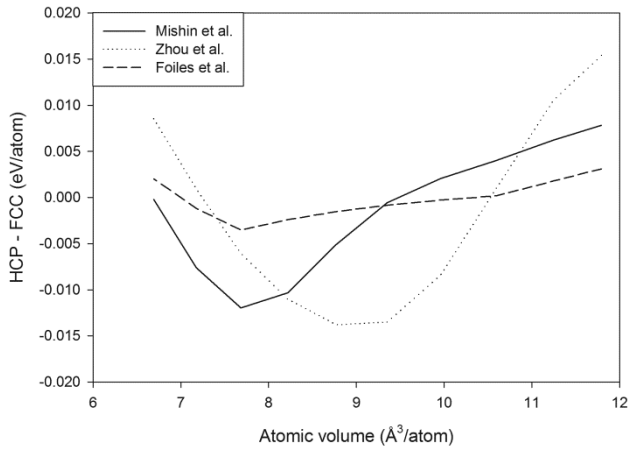

Figure 4.6: Comparison of free energy differences between hydrostatically compressed HCP and FCC structures for EAM interatomic potentials developed by Mishin et al. [39], Zhou et al. [52] and Foiles et al. [51]. Positive values indicate that the FCC structure is lower in energy.

hydrostatically compressed FCC Cu has a lower energy for atomic volumes greater than 9.4 Å^3/atom. Thus, relaxation of the uniaxially compressed structure into a FCC lattice with stacking faults and twins is justified. On the other hand, at particle velocities greater than 0.9 km/s, <100> shock creates a hydrostatic compression that results in atomic volumes less than 9.73 Å^3/atom. Free energy calculations show that hydrostatically compressed HCP Cu is lower energy for compressions with atomic volumes less than 9.4 Å^3/atom. Note, unlike the free energy calculations at 0 K, the influence of temperature on atomic volumes must be considered in the shock simulations. Thus, at the same compression level of shock simulations and free energy calculations, the atomic volume at the Hugoniot state of shock is greater than in the free energy calculations. Combined, observation of HCP cluster nucleation within the uniaxially compressed

Cu behind the shock front at particle velocities greater than 0.9 km/s is likely an artifact of the EAM formulation.

4.4 Conclusions

The molecular dynamics simulation method with the adaptive CNA identifies several crystal structures during <100> shock in single crystal Cu. Initially, the FCC Cu structure is uniaxially compressed towards the BCC structure behind the shock wave front; this process is more favorable at higher shock pressures and temperatures. For particle velocities between the Hugoniot elastic limit (HEL) and 0.9 km/s, compressed Cu quickly relaxes back into a faulted FCC structure including dislocations, stacking faults and twinning. The competition between <100> uniaxial elastic compression of Cu and the nucleation/motion of dislocations is a temperature dependent phenomenon. For particle velocities greater than 0.9 km/s, simulations show that uniaxial compression of Cu can promote the nucleation of HCP and faulted FCC structures. Free energy calculations of uniaxially compressed Cu, along a stress path similar to that during shock, and hydrostatically compressed FCC and HCP Cu show that for particle velocities of 0.9 km/s and below, FCC Cu is the lowest energy crystal structure. However, for atomic volumes between 6.6 and 9.4 $Å^3$/atom, the HCP structure of Cu is predicted by the EAM potential to have a lower energy with differences on the meV energy level. Since HCP Cu is not observed experimentally during shock at high pressures, the nucleation and growth of HCP clusters behind the <100> shock wave front for particle velocities above 0.9 km/s is likely an artifact of EAM interatomic potentials.

Acknowledgments

Support of the 21st Century Professorship in Mechanical Engineering and the Department of Mechanical Engineering at the University of Arkansas is greatly appreciated. Simulations in this work were performed on high performance computing equipment supported in part by National Science Foundation grants ARI #0963249, MRI #0959124, EPS #0918970, and a grant from the Arkansas Science and Technology Authority, managed by the University of Arkansas, Arkansas High Performance Computing Center.

References

[1] B. L. Holian and P. S. Lomdahl, "Plasticity Induced by Shock Waves in Nonequilibrium Molecular-Dynamics Simulations," *Science*, vol. 280, no. 5372, pp. 2085–2088, Jun. 1998.

[2] T. C. Germann, B. L. Holian, P. S. Lomdahl, and R. Ravelo, "Orientation Dependence in Molecular Dynamics Simulations of Shocked Single Crystals," *Phys. Rev. Lett.*, vol. 84, no. 23, pp. 5351–5354, Jun. 2000.

[3] T. C. Germann, B. L. Holian, P. S. Lomdahl, D. Tanguy, M. Mareschal, and R. Ravelo, "Dislocation structure behind a shock front in fcc perfect crystals: Atomistic simulation results," *Metall. Mater. Trans. A*, vol. 35, no. 9, pp. 2609–2615, 2004.

[4] M. M. Sichani and D. E. Spearot, "A molecular dynamics study of dislocation density generation and plastic relaxation during shock of single crystal Cu," *J. Appl. Phys.*, vol. 120, no. 4, p. 45902, Jul. 2016.

[5] M. S. Schneider, B. K. Kad, M. A. Meyers, F. Gregori, D. Kalantar, and B. A. Remington, "Laser-induced shock compression of copper: Orientation and pressure decay effects," *Metall. Mater. Trans. A*, vol. 35, no. 9, pp. 2633–2646, 2004.

[6] F. Cao, I. J. Beyerlein, F. L. Addessio, B. H. Sencer, C. P. Trujillo, E. K. Cerreta, and G. T. Gray III, "Orientation dependence of shock-induced twinning and substructures in a copper bicrystal," *Acta Mater.*, vol. 58, no. 2, pp. 549–559, 2010.

[7] A. M. Podurets, V. A. Raevskii, V. G. Khanzhin, A. I. Lebedev, O. N. Aprelkov, V. V. Igonin, I. N. Kondrokhina, A. N. Balandina, M. I. Tkachenko, J. Petit, and M. A. Zocher, "Twin structures in copper after shock and Shockless high-rate loading," *Combust.*

Explos. Shock Waves, vol. 47, no. 5, pp. 606–614, 2011.

[8] B. Cao, D. H. Lassila, C. Huang, Y. Xu, and M. A. Meyers, "Shock compression of monocrystalline copper: Experiments, characterization, and analysis," *Mater. Sci. Eng. A*, vol. 527, no. 3, pp. 424–434, 2010.

[9] K. Kadau, T. C. Germann, P. S. Lomdahl, and B. L. Holian, "Microscopic View of Structural Phase Transitions Induced by Shock Waves," *Science*, vol. 296, no. 5573, pp. 1681–1684, May 2002.

[10] K. Kadau, T. C. Germann, P. S. Lomdahl, and B. L. Holian, "Atomistic simulations of shock-induced transformations and their orientation dependence in bcc Fe single crystals," *Phys. Rev. B*, vol. 72, no. 6, p. 64120, Aug. 2005.

[11] K. Kadau, F. J. Cherne, R. Ravelo, and T. C. Germann, "Shock-induced phase transformations in gallium single crystals by atomistic methods," *Phys. Rev. B*, vol. 88, no. 14, p. 144108, Oct. 2013.

[12] H. Zong, X. Ding, T. Lookman, J. Li, J. Sun, E. K. Cerreta, A. P. Escobedo, F. L. Addessio, and C. A. Bronkhorst, "Collective nature of plasticity in mediating phase transformation under shock compression," *Phys. Rev. B*, vol. 89, no. 22, p. 220101, Jun. 2014.

[13] X. Cui, W. Zhu, H. He, X. Deng, and Y. Li, "Phase transformation of iron under shock compression: Effects of voids and shear stress," *Phys. Rev. B*, vol. 78, no. 2, p. 24115, Jul. 2008.

[14] J. M. D. Lane and A. P. Thompson, "Molecular dynamics simulation of shock-induced phase transition in germanium," *AIP Conference Proceedings*, vol. 1195. pp. 1157–1160, 2009.

[15] W. Pang, P. Zhang, G. Zhang, A. Xu, and X. Zhao, "Morphology and growth speed of hcp domains during shock-induced phase transition in iron.," *Sci. Rep.*, vol. 4, p. 3628, Jan. 2014.

[16] W. Pang, P. Zhang, G. Zhang, A. Xu, and X. Zhao, "Nucleation and growth mechanisms of hcp domains in compressed iron.," *Sci. Rep.*, vol. 4, p. 5273, 2014.

[17] J. L. Shao, S. Q. Duan, A. M. He, P. Wang, and C. S. Qin, "Microscopic dynamics of structural transition in iron with a nanovoid under shock loading.," *J. Phys. Condens. Matter*, vol. 22, no. 35, p. 355403, 2010.

[18] K. Wang, S. Xiao, H. Deng, W. Zhu, and W. Hu, "An atomic study on the shock-induced plasticity and phase transition for iron-based single crystals," *Int. J. Plast.*, vol. 59, pp. 180–198, 2014.

[19] B. T. Wang, J. L. Shao, G. C. Zhang, W. D. Li, and P. Zhang, "Nucleation of hcp and fcc phases in bcc iron under uniform compression: classical molecular dynamics simulations.," *J. Phys. Condens. Matter*, vol. 22, no. 43, p. 435404, 2010.

[20] B. T. Wang, J. L. Shao, G. C. Zhang, W. D. Li, and P. Zhang, "Molecular dynamics simulations of hcp/fcc nucleation and growth in bcc iron driven by uniaxial compression.," *J. Phys. Condens. Matter*, vol. 21, no. 49, p. 495702, 2009.

[21] S. J. Wang, M. L. Sui, Y. T. Chen, Q. H. Lu, E. Ma, X. Y. Pei, Q. Z. Li, and H. B. Hu, "Microstructural fingerprints of phase transitions in shock-loaded iron.," *Sci. Rep.*, vol. 3, p. 1086, 2013.

[22] H. Zong, T. Lookman, X. Ding, S. N. Luo, and J. Sun, "Anisotropic shock response of titanium: Reorientation and transformation mechanisms," *Acta Mater.*, vol. 65, pp. 10–18, Feb. 2014.

[23] N. Gunkelmann, E. M. Bringa, K. Kang, G. J. Ackland, C. J. Ruestes, and H. M. Urbassek, "Polycrystalline iron under compression: Plasticity and phase transitions," *Phys. Rev. B*, vol. 86, no. 14, p. 144111, Oct. 2012.

[24] N. Gunkelmann, E. M. Bringa, D. R. Tramontina, C. J. Ruestes, M. J. Suggit, A. Higginbotham, J. S. Wark, and H. M. Urbassek, "Shock waves in polycrystalline iron: Plasticity and phase transitions," *Phys. Rev. B*, vol. 89, no. 14, p. 140102, 2014.

[25] N. Gunkelmann, D. R. Tramontina, E. M. Bringa, and H. M. Urbassek, "Interplay of plasticity and phase transformation in shock wave propagation in nanocrystalline iron," *New J. Phys.*, vol. 16, no. 9, p. 93032, Sep. 2014.

[26] K. Kadau, T. C. Germann, P. S. Lomdahl, R. C. Albers, J. S. Wark, A. Higginbotham, and B. L. Holian, "Shock Waves in Polycrystalline Iron," *Phys. Rev. Lett.*, vol. 98, no. 13, p. 135701, Mar. 2007.

[27] A. V. Bolesta and V. M. Fomin, "Phase transition behind a shock front in polycrystalline copper," *Dokl. Phys.*, vol. 59, no. 6, pp. 249–253, Jul. 2014.

[28] M. M. Sichani and D. E. Spearot, "A molecular dynamics study of the role of grain size and orientation on compression of nanocrystalline Cu during shock," *Comput. Mater. Sci.*, vol. 108, pp. 226–232, 2015.

[29] A. Stukowski, "Structure identification methods for atomistic simulations of crystalline materials," *Model. Simul. Mater. Sci. Eng.*, vol. 20, no. 4, p. 45021, Jun. 2012.

[30] L. G. Wang, M. Šob, and Z. Zhang, "Instability of higher-energy phases in simple and transition metals," *J. Phys. Chem. Solids*, vol. 64, no. 5, pp. 863–872, May 2003.

[31] Y. F. Wen and J. Sun, "Structural stability of higher-energy phases in Cu and Cu–Fe alloy revealed by ab initio calculations," *Comput. Mater. Sci.*, vol. 79, pp. 463–467, Nov. 2013.

[32] T. Kraft, P. M. Marcus, M. Methfessel, and M. Scheffler, "Elastic constants of Cu and the instability of its bcc structure," *Phys. Rev. B*, vol. 48, no. 9, pp. 5886–5890, 1993.

[33] W. Mei, Y. Wen, H. Xing, P. Ou, and J. Sun, "Ab initio calculations of mechanical stability of bcc Cu under pressure," *Solid State Commun.*, vol. 184, pp. 25–28, 2014.

[34] I. A. Morrison, M. H. Kang, and E. J. Mele, “First-principles determination of the bulk phase diagram for body-centered-tetragonal copper: Application to epitaxial growth of Cu on Fe{100},” *Phys. Rev. B*, vol. 39, no. 3, pp. 1575–1580, 1989.

[35] L. G. Wang and M. Šob, “Structural stability of higher-energy phases and its relation to the atomic configurations of extended defects: The example of Cu,” *Phys. Rev. B*, vol. 60, no. 2, pp. 844–850, Jul. 1999.

[36] P. Wen, G. Tao, C. Pang, S. Yuan, and Q. Wang, “A molecular dynamics study of the shock-induced defect microstructure in single crystal Cu,” *Comput. Mater. Sci.*, vol. 124, pp. 304–310, 2016.

[37] W. J. Murphy, A. Higginbotham, G. Kimminau, B. Barbrel, E. M. Bringa, J. Hawreliak, R. Kodama, M. Koenig, W. McBarron, M. A. Meyers, B. Nagler, N. Ozaki, N. Park, B. Remington, S. Rothman, S. M. Vinko, T. Whitcher, and J. S. Wark, “The strength of single crystal copper under uniaxial shock compression at 100 GPa,” *J. Phys. Condens. Matter*, vol. 22, no. 6, p. 65404, Feb. 2010.

[38] S. Plimpton, “Fast Parallel Algorithms for Short-Range Molecular Dynamics,” *J. Comp. Phys.*, vol. 117, no. 1, pp. 1–19, 1995.

[39] Y. M. Mishin, M. Mehl, D. Papaconstantopoulos, A. F. Voter, and J. Kress, “Structural stability and lattice defects in copper: Ab initio, tight-binding, and embedded-atom calculations,” *Phys. Rev. B*, vol. 63, no. 22, p. 224106, May 2001.

[40] E. M. Bringa, J. U. Cazamias, P. Erhart, J. Stölken, N. Tanushev, B. D. Wirth, R. E. Rudd, and M. J. Caturla, “Atomistic shock Hugoniot simulation of single-crystal copper,” *J. Appl. Phys.*, vol. 96, no. 7, p. 3793, 2004.

[41] A. Neogi and N. Mitra, “Evolution of dislocation mechanisms in single-crystal Cu under shock loading in different directions,” *Model. Simul. Mater. Sci. Eng.*, vol. 25, no. 2, p. 25013, Feb. 2017.

[42] A. Bolesta, L. Zheng, D. Thompson, and T. Sewell, “Molecular dynamics simulations of shock waves using the absorbing boundary condition: A case study of methane,” *Phys. Rev. B*, vol. 76, no. 22, p. 224108, Dec. 2007.

[43] J. D. Honeycutt and H. C. Andersen, “Molecular dynamics study of melting and freezing of small Lennard-Jones clusters,” *J. Phys. Chem.*, vol. 91, no. 19, pp. 4950–4963, Sep. 1987.

[44] A. Stukowski, “Visualization and analysis of atomistic simulation data with OVITO–the Open Visualization Tool,” *Model. Simul. Mater. Sci. Eng.*, vol. 18, no. 1, p. 15012, Jan. 2010.

[45] K. Wang, S. Xiao, H. Deng, W. Zhu, and W. Hu, “An atomic study on the shock-induced plasticity and phase transition for iron-based single crystals,” *Int. J. Plast.*, vol. 59, pp. 180–198, Aug. 2014.

[46] E. M. Bringa, K. Rosolankova, R. E. Rudd, B. A. Remington, J. S. Wark, M. Duchaineau, D. H. Kalantar, J. Hawreliak, and J. Belak, "Shock deformation of face-centred-cubic metals on subnanosecond timescales," *Nat. Mater.*, vol. 5, no. 10, pp. 805–809, Oct. 2006.

[47] H. Xie, F. Yin, T. Yu, G. Lu, and Y. Zhang, "A new strain-rate-induced deformation mechanism of Cu nanowire: Transition from dislocation nucleation to phase transformation," *Acta Mater.*, vol. 85, pp. 191–198, 2015.

[48] H. Wormeester, M. E. Kiene, E. Huger, and E. Bauer, "Growth of hcp Cu on W(100)," *Surf. Sci.*, vol. 377–379, pp. 988–991, 1997.

[49] F. Jona, X. Z. Ji, and P. M. Marcus, "Hexagonal close-packed copper: Theory and experiment," *Phys. Rev. B*, vol. 68, no. 17, p. 172101, Nov. 2003.

[50] A. Togo and I. Tanaka, "Evolution of crystal structures in metallic elements," *Phys. Rev. B*, vol. 87, no. 18, p. 184104, May 2013.

[51] S. Foiles, M. Baskes, and M. Daw, "Embedded-atom-method functions for the fcc metals Cu, Ag, Au, Ni, Pd, Pt, and their alloys," *Phys. Rev. B*, vol. 33, no. 12, pp. 7983–7991, Jun. 1986.

[52] X. W. Zhou, H. N. G. Wadley, R. A. Johnson, D. J. Larson, N. Tabat, A. Cerezo, A. K. Petford-Long, G. D. W. Smith, P. H. Clifton, R. L. Martens, and T. F. Kelly, "Atomic scale structure of sputtered metal multilayers," *Acta Mater.*, vol. 49, no. 19, pp. 4005–4015, 2001.

Chapter 5: A Molecular Dynamics Study of the Role of Grain Size and Orientation on Compression of Nanocrystalline Cu during Shock

Mehrdad M. Sichani[1] and Douglas E. Spearot[1, 2]

[1] Department of Mechanical Engineering

[2]Institute for Nanoscience and Engineering

University of Arkansas, Fayetteville, Arkansas 72701

Abstract

The molecular dynamics method is used to investigate the dependence of grain size and grain orientation on deformation in nanocrystalline Cu during shock. Particle velocities from 1.0 to 3.4 km/s are applied to nanocrystalline Cu samples with grain sizes from 6 to 26 nm. Results show that grain size does not significantly influence the temperature and pressure of the Hugoniot state. However, grain size, grain orientation and particle velocity do influence the details by which Cu is uniaxially compressed into a BCC structure at pressures between 100 and 200 GPa behind the shock front. The computed atomic percentage of BCC structure ranges between 3.4 and 9.2% depending on grain diameter at a particle velocity of 1.5 km/s, reaches a maximum between 23.3 to 30.7% at a particle velocity of 2.4 km/s, and then decreases to approximately 0.0% at a particle velocity of 3.2 km/s. At a particle velocity of 2.4 km/s, the atomic percentage of BCC structure observed during shock increases with increasing grain size, while this trend is reversed at a particle velocity of 1.5 km/s. Moreover, the observation of BCC structure strongly depends on grain orientation; grains with <100> directions closely aligned with the shock

loading direction show a higher percentage of BCC structure, implying a tetragonal transformation path (Bain path).

5.1 Introduction

Phase transformations in materials under shock loading can be divided into two distinct categories: solid-liquid phase transformations and solid-solid phase transformations. The Hugoniot state (the equilibrium state behind the shockwave front) and solid-liquid phase transformations have been extensively studied over the last several decades using molecular dynamics (MD) simulations and experimental methods [1–20]. For example, Bringa et al. [3] investigated the Hugoniot state during shock of single crystal copper along several different crystallographic directions for Hugoniot pressures between 2 and 800 GPa and reported that the shock velocity magnitude as a function of particle velocity was anisotropic. To further study anisotropies in the Hugoniot state and melting of Cu, He et al. [18] studied bulk and dynamic local melting of shocked hexagonal columnar nanocrystalline Cu samples and reported that even though the Hugoniot state and bulk melting behavior are independent of shock direction, the local melting is strongly anisotropic due to mechanisms including premelting, superheating, supercooling and recrystallization. To explain observations of melting in shocked Cu samples at temperatures below the expected melting temperature for a given shock pressure, Levitas and Ravelo [13] proposed virtual melting as a relaxation mechanism during states of high deviatoric stresses.

On the other hand, solid-solid phase transformations under shock loading are sometimes observed at pressures below the melting point. Over the last decade, MD simulations and

experimental studies have been performed to explore solid-solid phase transformations in single crystals [21–35]. For example, Kadau et al. [24] identified the role of shockwave strength on structural transformations in Ga single crystals. Cui et al. [21] explored the role of nanovoid size on the BCC to HCP phase transformation in Fe during shock. Comparatively, there are very few studies on solid-solid phase transformations in nanocrystalline materials [36–40]. Gunkelmann et al. [38] investigated the BCC to HCP phase transformation in nanocrystalline Fe during shock and observed dislocation generation at grain boundaries before the phase transformation.

More recently, a FCC to BCC phase transformation behind the shock front in nanocrystalline Cu was reported by Bolesta and Fomin [36]. In their work, nanocrystalline Cu samples were constructed via homogeneous nucleation and growth within a cooled melt at a constant temperature. To study the dynamics of material behind the shock front at longer times, they employed the Hugoniotstat algorithm [11]. For the range of grain diameters from 2 to 12 nm, Bolesta and Fomin reported that grain size does not significantly influence the shock Hugoniot curve, with only a modest (<10%) increase in temperature behind the shock front for the smallest 2 nm grain size model. A FCC to BCC phase transformation was identified behind the shock front between 100 and 200 GPa pressure via application of the structure factor equation. They reported that this phase transformation is possible only at combined states of high temperatures and pressures, and does not occur at room temperature regardless of the applied pressure. Upon unloading of the shock, the BCC lattice reverted back to a FCC lattice below 1150 K and 66 GPa, forming a cellular stacking fault structure. Bolesta and Fomin did not explore the role of grain size and orientation on the extent to which the system undergoes the observed structural transformation behind the shock front.

The observation made by Bolesta and Fomin contributes insight to the thermodynamic and mechanical stability of the BCC phase of Cu. Although some authors have reported that the BCC phase of Cu is unstable energetically [41,42] and mechanically [41,43], other authors have argued that under certain mechanical constraints, the BCC phase of Cu can be lower in energy than the FCC phase [44,45] and mechanically stable [46]. For example, Wang and Sob [45] showed that BCC Cu can be energetically stable if the lattice is restricted to deform along a trigonal deformation path. Also, recent ab initio calculations by Mei et al. [46] showed that BCC Cu under hydrostatic pressure becomes mechanically stable at 7.5 GPa compression, as shown by a change in the sign of the tetragonal shear modulus from negative to positive, and stability continues to increase with increasing hydrostatic compression. Interestingly, some researchers have predicted a double minimum in the total energy per atom of BCC Cu with respect to volume [44,47], while other researchers have predicted a single minimum [48–51]. Ultimately, under the right external constraints, the existence of BCC Cu can be favorable, validating observations of BCC Cu in precipitates and in epitaxially grown thin films [44,52]. Importantly, the combined role of temperature and pressure on the stability of BCC Cu has not been explored; Bolesta and Fomin [36] argued that their observation of BCC Cu during shock deformation is the combined effect of temperature and pressure on phase stability.

The main goal of this work is to determine how the deformation of nanocrystalline FCC Cu during shock depends on particle velocity, grain size and grain orientation using the molecular dynamics method. A wide range of particle velocities from 1.0 to 3.4 km/s (40 GPa to 256 GPa pressures) is applied and uniaxial compression of FCC Cu into the BCC structure is observed for pressures between 100 and 200 GPa, in agreement with observations of Bolesta and Fomin [36]. Four different grain diameters (6, 11, 16 and 26 nm) are selected to study the influence of grain

size on the Hugoniot state and the details of the deformation response in Cu. The effect of each grain orientation on Cu compression is also studied to provide more depth to the observation of BCC structure during shock of nanocrystalline FCC Cu. Results show that grains with a <100> direction closely aligned with the shock loading direction have a higher tendency for uniaxial compression into the BCC structure, implying a tetragonal deformation path (Bain path).

5.2 Methodology

The molecular dynamics method with the LAMMPS software [53] is used to simulate the shock and the Hugoniot state in nanocrystalline Cu. The embedded-atom method (EAM) potential for Cu developed by Mishin et al. [54] is used as the interatomic potential. The Voronoi method is implemented to construct a random distribution of grain orientations for four different grain diameters (6, 11, 16 and 26 nm) within fully periodic simulation cells. Figure 5.1 shows a representative schematic of the simulation cell for the nanocrystalline Cu samples. Table 5.1 contains information related to the simulation cell size for each grain diameter.

Table 5.1: Physical dimensions and number of atoms in each nanocrystalline model.

Grain diameter (nm)	Number of grains	Number of atoms	X length (nm)	Y length (nm)	Z length (nm)
6	800	~ 5,600,000	23.86	23.86	116.37
11	240	~ 10,700,000	33.0	33.0	115.86
16	73	~ 10,000,000	32.0	32.0	115.82
26	45	~ 26,500,000	52.0	52.0	115.87

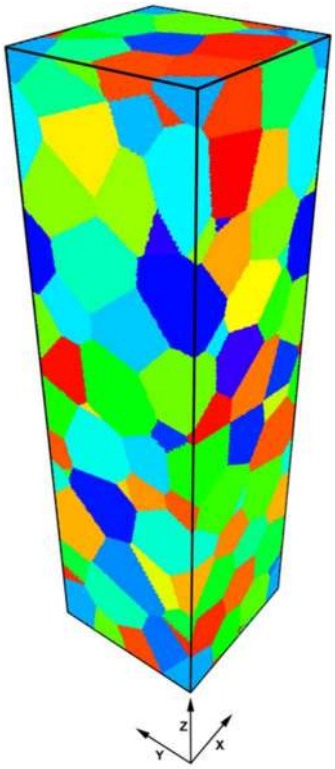

Figure 5.1: Schematic of the nanocrystalline Cu sample with 73 grains and a grain diameter of 16 nm (colored by grain number).

Initially, the microstructure is equilibrated to a desired temperature and pressure of 300 K and 1 bar using the constant pressure-temperature (NPT) method and 3D periodic boundary conditions. Then, the periodic boundary condition in the z-direction is removed, exposing free surfaces in this direction. Shock is induced in the microstructure using the momentum mirror technique [55] under periodic boundary conditions in the x- and y-directions. In the z-direction, shock is created by assigning each atom in the microstructure a particle velocity of $-u_p$, impacting the sample with a stationary infinite mass wall. The shockwave is generated in the opposite direction at the interface between the sample and the wall. At the precise time the shockwave reaches the end of the sample, an absorbing wall condition [56] is activated. The simulation

continues for 100 ps to achieve the Hugoniot state. The equations of motion are integrated with the velocity-Verlet method with a time step of 1 fs for all simulations. To study the structure of nanocrystalline Cu before and after shock, and the fraction of the system that undergoes structure transformation during shock, the common neighbor analysis (CNA) method with an adaptive cutoff distance [57] in OVITO [58] is used.

5.3 Results and Discussion

Figure 5.2 shows the temperature-pressure relationship at the Hugoniot state for particle velocities from 1.0 to 3.4 km/s applied to each nanocrystalline Cu sample. The temperatures in Figure 5.2 are computed after removing the z-component of the velocity (the velocity in the direction of the shock loading). Pressures are computed using the virial definition for stress with the z-component of the velocity removed. The pressures in Figure 5.2 are the average of the pressures in x-, y-, and z-directions. The hydrostatic melting curve in Figure 5.2 is extracted from the theoretical calculations of Moriarty [59] for single crystal Cu. The Hugoniot state occurs when the system is at thermodynamic equilibrium; Figures 5.3(a) and 5.3(b) show that the system has achieved thermodynamic equilibrium behind the shock front.

The Hugoniot graph (Figure 5.2) provides a clear method to differentiate between partial melting and bulk melting based on the temperature and pressure of the microstructure at the Hugoniot state. This figure can be divided into three main regions: solid, partial melting and liquid. The points under the hydrostatic melting curve are in the solid state, the points above the hydrostatic melting curve are in the liquid state and the points which approximately coincide with the hydrostatic melting curve indicate partial melting of the nanocrystalline sample. Partial

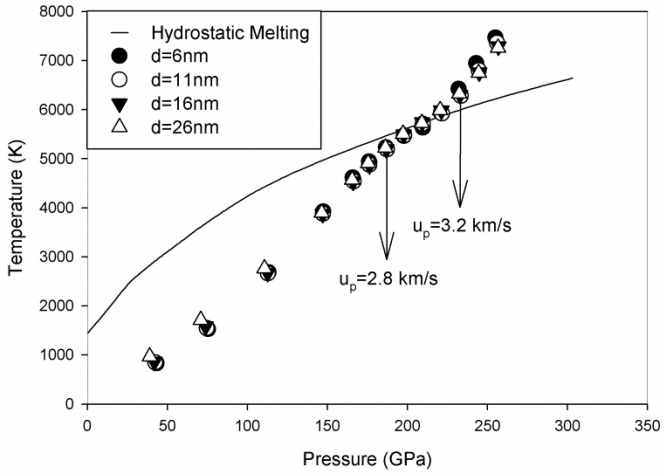

Figure 5.2: The temperature-pressure relationship at the Hugoniot state in nanocrystalline Cu at different particle velocities and different grain diameters. The hydrostatic melting data is taken from [59].

melting occurs within the pressure range between 186 and 220 GPa (particle velocities from 2.8 to 3.1 km/s). This range is in reasonable agreement with previous MD work for a columnar nanocrystalline Cu sample with a grain size of 26 nm which showed a partial melting range of 197 to 257 GPa [18], and also previous experimental work for polycrystalline Cu with a partial melting range of 232 to 265 GPa [60]. Bulk melting occurs at pressures above 220 GPa (3.1 km/s particle velocity), which agrees very well with previous MD works for polycrystalline [36] and single crystal Cu [1,3,6,15,20]. Results in Figure 5.2 show that the grain size does not have a significant influence on the pressure or the temperature at the Hugoniot state for the range of particle velocities from 1.0 to 3.4 km/s and the range of the grain diameters from 6 to 26 nm. This conclusion is in agreement with Bolesta and Fomin [36], which was done for a range of grain diameters from 2 to 12 nm. Although nanocrystalline samples contain a high fraction of

atoms at grain boundaries, the shock intensity is sufficiently large that grain size does not appreciably effect the initiation of partial melting during shock.

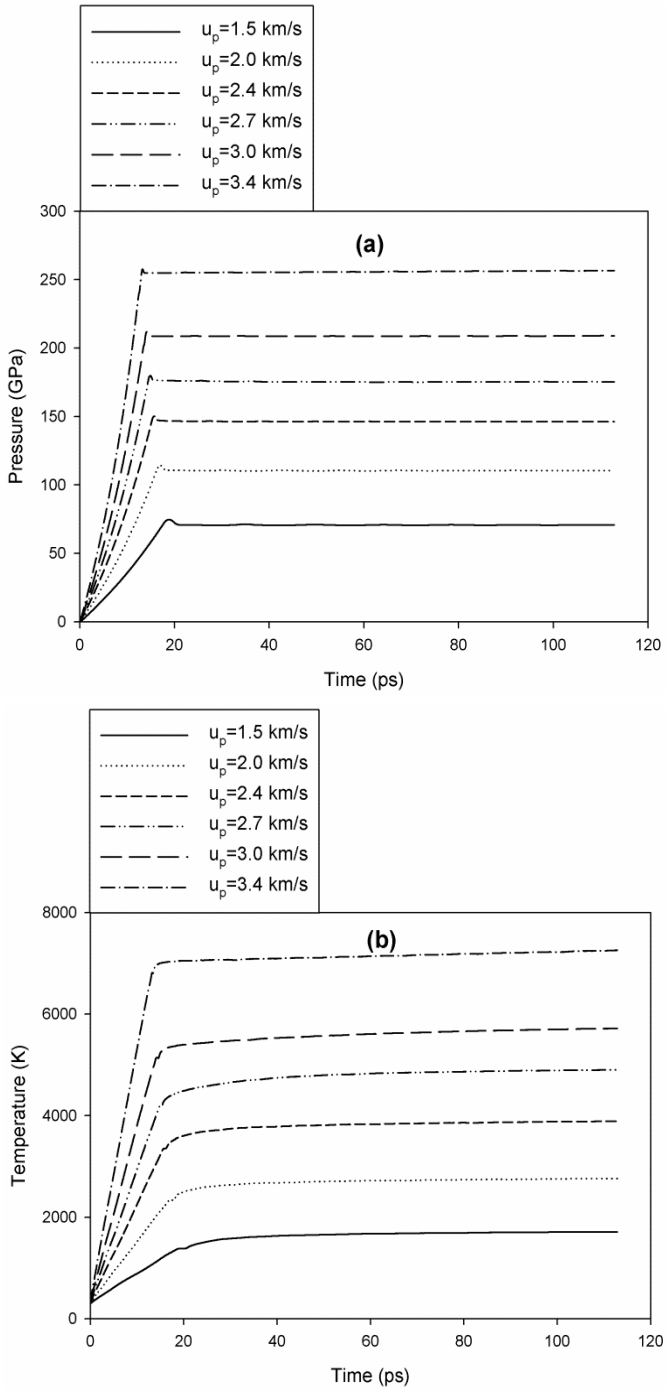

Figure 5.3: (a) The pressure evolution of shocked nanocrystalline Cu reaching the Hugoniot state, (b) the temperature evolution of shocked nanocrystalline Cu reaching the Hugoniot state.

Figure 5.4 shows a nanocrystalline Cu sample with 16 nm average grain diameter subjected to a shock particle velocity of 2.0 km/s (corresponding to a pressure of 113 GPa and a temperature of 2680 K). Based on CNA, a portion of the nanocrystalline Cu sample is identified as BCC structure. This observation is in agreement with Bolesta and Fomin [36]. To investigate if the existence of the BCC structure behind the shock front is an artifact of the interatomic potential employed, two additional interatomic potentials are used [61,62] and in both cases the BCC structure is observed during shock loading. Note, Belonoshko et al. [63] performed equilibrium MD simulations studying single crystal Cu behavior during hydrostatic compression up to 200 GPa and temperatures up to 1400 K, and did not observe a FCC to BCC transformation. To extend these equilibrium (NPT) simulations to temperatures characteristic of those observed behind the shock front in Figure 5.3(b), supplemental simulations are performed in the current work using 3D periodic boundary conditions for hydrostatic pressures between 50 and 200 GPa and temperatures up to 3000 K. The BCC structure is not observed in any of these equilibrium single crystal Cu simulations. However, a significant percentage of BCC structure is identified using CNA (~ 87at.% BCC) behind the shock front at a Hugoniot pressure and temperature of 120 GPa and 2300 K in single crystal Cu shocked along the [001] direction, with periodic boundary conditions in the [100] and [010] directions. Therefore, observation of BCC structure occurs during dynamic uniaxial deformation produced during shock loading and not during an equilibrium hydrostatic loading.

Figure 5.5 shows the atomic percentage of the nanocrystalline Cu sample that is identified as BCC structure at the Hugoniot state for different grain sizes (6 to 26 nm) and particle velocities (1.0 to 3.2 km/s). At 2.4 km/s (147 GPa), the atomic percentage of the sample that has a BCC structure increases with increasing grain size (most significantly in the range between 6 to 16

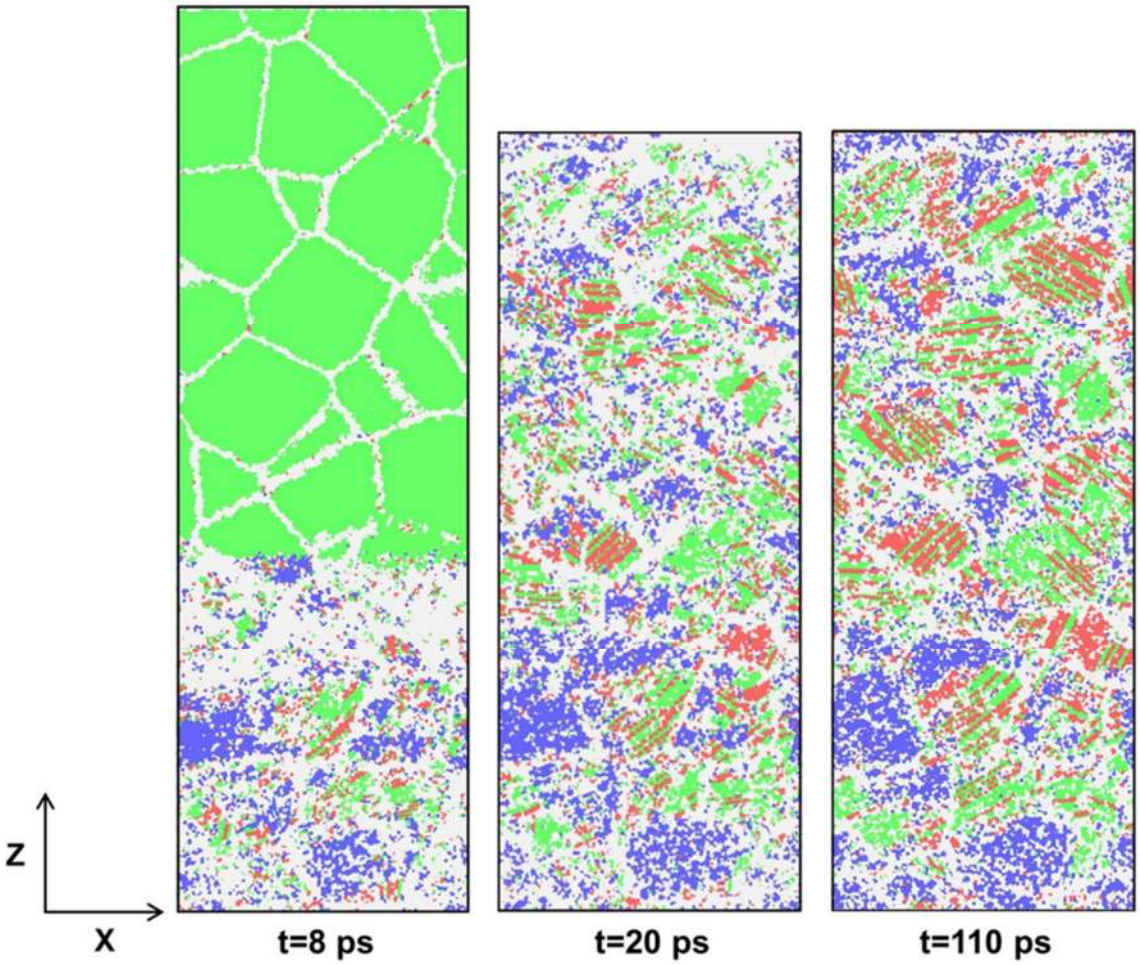

Figure 5.4: Structure evolution for a shocked nanocrystalline Cu sample with 73 grains, grain diameter of 16 nm and particle velocity of 2.0 km/s based on CNA (the green, red, blue and white colors are associated with the FCC, HCP, BCC and unidentified structures, respectively).

nm). In samples with larger grains, a larger fraction of atoms are originally in the FCC phase, thus the potential of Cu compression into a BCC structure increases. For particle velocities from 2.8 to 3.1 km/s, partial melting occurs and a portion of the FCC phase is transformed to the liquid phase instead of the BCC structure. CNA indicates that the microstructure at 2.8 km/s particle velocity includes a combination of BCC structure and unidentified structure associated with disordered grain boundaries and virtual melting [13]. For particle velocities more than 3.1

km/s the FCC to BCC structural transformation is not observed; instead, the microstructure undergoes a solid-liquid phase transformation.

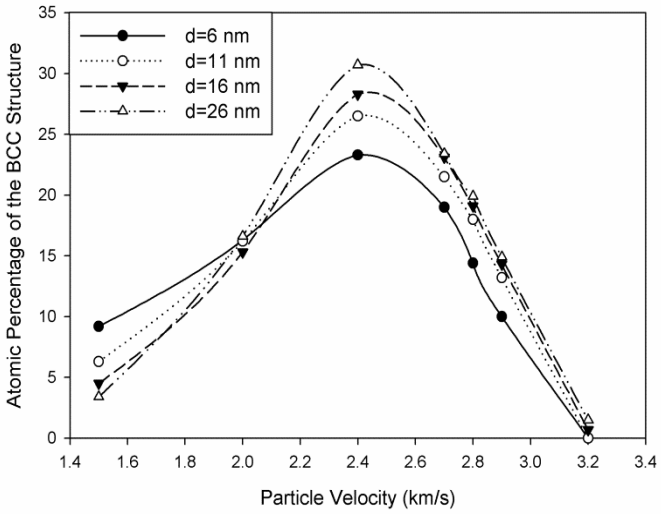

Figure 5.5: Variation of the atomic percentage of BCC structure at the Hugoniot state as a function of grain diameter and particle velocity.

Unexpectedly, at a particle velocity of 1.5 km/s, the atomic percentage of the BCC structure increases with decreasing grain size. To investigate if the number of grains influences this observation, a nanocrystalline sample with 240 grains and average grain diameter of 6 nm is created and subjected to shock with particle velocities of 1.5, 2.0, and 2.4 km/s. CNA results show that the atomic percentage of BCC structure is nearly identical to the nanocrystalline sample with 800 grains and average grain diameter of 6 nm shown in Figure 5.5. Thus, it is hypothesized that the behavior at 1.5 km/s is due to the difficulty of dislocation nucleation in the smallest nanocrystalline samples, demanding that a uniaxial compression to the BCC structure occurs to accommodate the shock deformation. These calculations are repeated for three different realizations of the microstructure for grain diameters from 6 to 26 nm and particle

velocities of 1.5, 2.0 and 2.4 km/s. The role of grain size on atomic percentage of BCC structure observed in Figure 5.5 is consistent. Specifically, the difference between the atomic percentage of the BCC structure for a specific grain size and particle velocity, and corresponding average atomic percentage of the BCC structure is less than +/-1.35%.

The ability of the FCC Cu lattice to compress into the BCC structure has a noticeable dependence on the orientation of grains within the nanocrystalline Cu sample. The dependence of solid-solid phase transformations on the crystallographic orientation of shock have been investigated through MD simulations for single crystal Fe [23,28], Ti [29] and Nb [22]. Interestingly, Kadau et al. [40] observed a BCC to HCP phase transformation during shock of nanocrystalline Fe accompanied by the observation of metastable FCC structure. The HCP/FCC ratio depended on shock intensity and grain orientation and this ratio within a grain decreased as the shock direction deviated from [001]. The research done by Kadau et al. [40] revealed that an unexpected phase transformation can occur during shock which depends on grain orientation.

Recall, Figure 5.4 shows that the compression of Cu into the BCC structure occurs readily in some grains, while other grains deform by other plastic-deformation mechanisms, implying that grain orientation (and potentially grain neighborhood and grain boundary geometry) is a significant factor in the compression of Cu into the BCC structure. To study the orientation dependence of deformation during shock, the Euler angles of every grain are cross-referenced against the fraction of BCC structure identified via CNA. In the Voronoi construction code used in this work, grain orientation is determined by a randomly selected set of three Euler angles: The first rotation is around the original x-axis, the second rotation is around the new y-axis and the third rotation is around the new z-axis. Figure 5.6 shows the three-dimensional Euler space

for one nanocrystalline Cu sample with 45 grains and an average grain diameter of 26 nm. The grains with the largest atomic percentage of BCC structure during shock are generally associated with the largest magnitude of the second component of the Euler rotation sequence. Four simulations with a grain size of 26 nm and two simulations with a grain size of 16 nm with different microstructure realizations are analyzed to confirm that this result is consistent for all models studied.

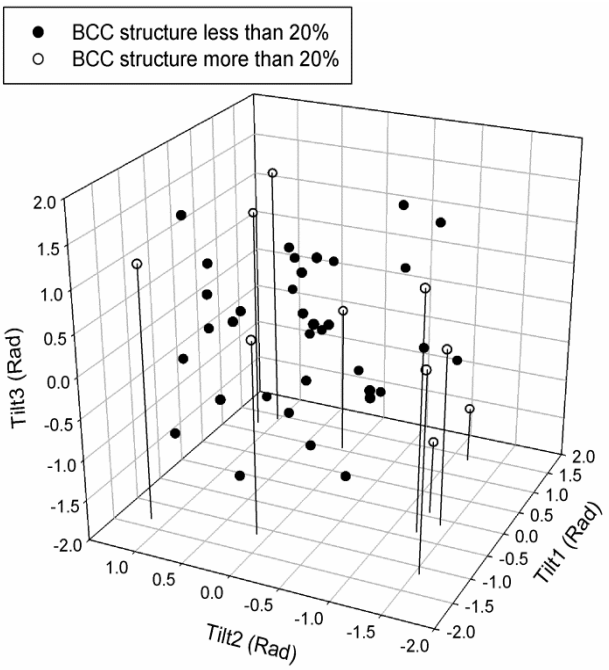

Figure 5.6: Variation of the atomic percentage of BCC structure at the Hugoniot state as a function of grain diameter and particle velocity.

The tetragonal path (Bain path) is the simplest phase transformation path between the FCC and the BCC phases. Considering the [001] direction as the c-axis, the tetragonal path is a compression or expansion along the [001] direction until the c/a ratio associated with each phase is reached, where a is the lattice parameter of the cubic crystal lattice [64]. An alternative

transformation path is possible along the [111] direction called the trigonal path. Selecting the [111] direction as the c-axis, the trigonal path is a compression and expansion along [111] until the c/a ratio associated with each phase is reached [64]. For both transformation paths, the FCC to BCC phase transformation occurs by compression. Additional details on the tetragonal and trigonal phase transformation paths in copper can be obtained in [45].

Figure 5.7 shows a grain-by-grain analysis highlighting which grains have <100> or <111> lattice orientations closely aligned with the shock loading direction (z direction). Figure 5.7(a) shows nanocrystalline Cu deformation during shock at a particle velocity of 2.0 km/s. Grains with a higher atomic percentage of BCC structure have a member of the <100> direction within 25 degrees ($\cos(\theta) < 0.9$) of the z-axis implying that the tetragonal deformation path is activated. In addition, for grains with a higher percentage of the BCC structure, there is no member of the <111> aligned close to the shock loading direction, as shown in Figure 5.7(b). This indicates that the trigonal deformation path is not activated, likely due to the existence of a much higher energy barrier along the trigonal path [45]. This analysis is repeated using two different microstructure realizations with an average grain size of 16 nm and four different microstructure realizations with an average grain size of 26 nm; the tetragonal phase transformation path is consistently observed in the grains with a higher percentage of the BCC structure.

This analysis is repeated for particle velocities of 1.5 and 2.4 km/s and two different grain sizes of 16 nm and 26 nm. Generally, grains with a higher atomic percentage of BCC structure at a particle velocity of 1.5 km/s are the same grains that show BCC structure at a particle velocity of 2.0 km/s. However, at a particle velocity of 2.4 km/s, some grains which had a lower atomic percentage of BCC structure at the particle velocities of 1.5 and 2.0 km/s have a higher BCC

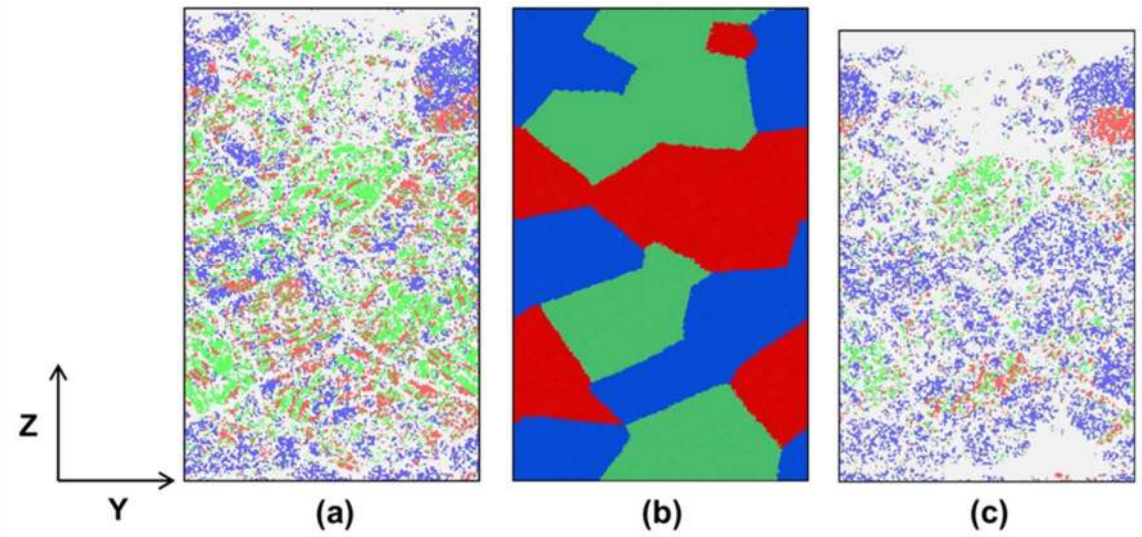

Figure 5.7: CNA for a model with 45 grains, grain diameter of 26 and particle velocity of 2.0 km/s at t=20 ps (the green, red, blue and white colors are associated with the FCC, HCP, BCC and unidentified structures, respectively), (b) blue, red and green colors are grains with angle between <100> directions and z-axis less than 25 degrees, grains with angle between <111> directions and z-axis less than 25 degrees, grains without angle between <100> or <111> directions and z-axis less than 25 degree, respectively (c), CNA at particle velocity of 2.4 km/s, color scheme is the same as in (a).

atomic percentage. These grains have a member of the <111> direction close to the shock loading direction as shown in Figures 5.7(b) and 5.7(c). This implies that the trigonal phase transformation path can occur at a particle velocity of 2.4 km/s, overcoming the higher energy barrier along the trigonal phase transformation path [45]. Note, the temperature at a particle velocity of 2.4 km/s is higher than 2.0 km/s and this may contribute to the increased stability of the BCC structure. Finally, there are a few grains which have <100> or <111> orientations closely aligned with the shock loading direction that do not show BCC structure. This implies that the location of grains as well as the orientation of neighbor grains could be important.

5.4 Conclusions

The molecular dynamics method is used to study the role of grain size and grain orientation on deformation during shock of nanocrystalline Cu. A range of particle velocities from 1.0 to 3.4 km/s are applied to nanocrystalline Cu samples with grain sizes from 6 to 26 nm. The grain size of nanocrystalline Cu does not appreciably influence the temperature and the pressure of the Hugoniot state. CNA identifies BCC structure at pressures between 100 and 200 GPa behind the shock front, which depends on grain size, grain orientation and particle velocity. The atomic percentage of the BCC structure ranges between 3.4 and 9.2% depending on grain diameter at a particle velocity of 1.5 km/s, reaches a maximum between 23.3 to 30.7% at a particle velocity of 2.4 km/s, and then decreases to approximately 0.0% at a particle velocity of 3.2 km/s. At 2.4 km/s, the atomic percentage of BCC structure increases with increasing grain size. In larger grains, a larger fraction of atoms are originally in the FCC phase, and the potential for compression of FCC Cu into BCC structure increases. This trend is reversed at a particle velocity of 1.5 km/s and it is hypothesized that the difficulty of dislocation nucleation in the smaller grain size sample leads to this observation.

Moreover, compression of FCC Cu into the BCC structure strongly depends on grain orientation. At a particle velocity of 2.0 km/s, grains with a <100> direction closely aligned with the shock loading direction show higher propensity for compression into the BCC structure. This implies that the transformation path is tetragonal (Bain). However, at a particle velocity of 2.4 km/s, some grains which showed a lower atomic percentage of BCC structure at particle velocities of 1.5 and 2.0 km/s, have a higher BCC atomic percentage. These grains have a <111> direction closely aligned with the direction of shock, implying that at higher shock velocities, the trigonal deformation path may be active despite the larger energy barrier. Finally, there are a few

grains which are properly oriented for tetragonal or trigonal transformation that do not compress from FCC Cu to BCC structure within the time scale of the simulation. This implies that the locations of grains as well as orientation of neighbor grains and grain boundary structure are also important factors in the prediction of structural transformations.

Acknowledgements

The authors acknowledge support of the 21st Century Professorship in Mechanical Engineering at the University of Arkansas. DES would like to thank Dr. Saryu Fensin of Los Alamos National Laboratory for fruitful discussions related to this work.

References

[1] Q. An, S. N. Luo, L. B. Han, L. Zheng, and O. Tschauner, "Melting of Cu under hydrostatic and shock wave loading to high pressures," *J. Phys. Condens. Matter*, vol. 20, no. 9, p. 95220, Mar. 2008.

[2] L. S. Dubrovinsky and A. B. Belonoshko, "Shock Wave-Induced Melting in Argon by Atomistic Simulation," *Science (New York, N.Y.)*, vol. 278, no. 5342. pp. 1474–1476, 1997.

[3] E. M. Bringa, J. U. Cazamias, P. Erhart, J. Stölken, N. Tanushev, B. D. Wirth, R. E. Rudd, and M. J. Caturla, "Atomistic shock Hugoniot simulation of single-crystal copper," *J. Appl. Phys.*, vol. 96, no. 7, p. 3793, 2004.

[4] M. M. Budzevich, V. V. Zhakhovsky, C. T. White, and I. I. Oleynik, "Shock-induced phase transitions in metals: Recrystallization of supercooled melt and melting of overheated solids," *AIP Conference Proceedings*, vol. 1426. pp. 1267–1270, 2012.

[5] F. J. Cherne, M. I. Baskes, T. C. Germann, R. J. Ravelo, and K. Kadau, "Shock Hugoniot and Melt Curve for a Modified Embedded Atom Method Model of Gallium," *AIP Conference Proceedings*, vol. 706. pp. 281–284, 2004.

[6] A. M. He, S. Duan, J. L. Shao, P. Wang, and C. Qin, "Shock melting of single crystal

copper with a nanovoid: Molecular dynamics simulations," *J. Appl. Phys.*, vol. 112, no. 7, p. 74116, 2012.

[7] Y. Ju, Q. Zhang, Z. Gong, G. Ji, and L. Zhou, "Molecular dynamics simulation of shock melting of aluminum single crystal," *J. Appl. Phys.*, vol. 114, no. 9, p. 93507, 2013.

[8] K. Kadau, T. C. Germann, P. S. Lomdahl, and B. L. Holian, "Atomistic simulations of shock-induced melting in Fe," *AIP Conference Proceedings*, vol. 845. pp. 236–239, 2006.

[9] Z. L. Liu, J. H. Yang, Z. G. Zhao, L. C. Cai, and F. Q. Jing, "The anisotropy of shock-induced melting of Pt observed in molecular dynamics simulations," *Phys. Lett. A*, vol. 374, no. 13–14, pp. 1579–1584, Mar. 2010.

[10] D. V. Minakov, P. R. Levashov, K. V. Khishchenko, and V. E. Fortov, "Quantum molecular dynamics simulation of shock-wave experiments in aluminum," *J. Appl. Phys.*, vol. 115, no. 22, p. 223512, Jun. 2014.

[11] R. Ravelo, B. L. Holian, T. C. Germann, and P. S. Lomdahl, "Constant-stress Hugoniostat method for following the dynamical evolution of shocked matter," *Phys. Rev. B*, vol. 70, no. 1, p. 14103, Jul. 2004.

[12] R. Ravelo, B. L. Holian, T. C. Germann, and P. Lomdahl, "Directional-dependence in shock-induced melting of FCC metals," *AIP Conference Proceedings*, vol. 845. pp. 270–273, 2006.

[13] V. I. Levitas and R. Ravelo, "Virtual melting as a new mechanism of stress relaxation under high strain rate loading.," *Proc. Natl. Acad. Sci. U. S. A.*, vol. 109, no. 33, pp. 13204–7, Aug. 2012.

[14] M. M. Budzevich, V. V. Zhakhovsky, C. T. White, and I. I. Oleynik, "Evolution of Shock-Induced Orientation-Dependent Metastable States in Crystalline Aluminum," *Phys. Rev. Lett.*, vol. 109, no. 12, p. 125505, Sep. 2012.

[15] A. M. He, P. Wang, J. L. Shao, S. Q. Duan, F. P. Zhao, and S. N. Luo, "Solid-liquid phase transitions in single crystal Cu under shock and release conditions," *J. Appl. Phys.*, vol. 115, no. 14, p. 143503, Apr. 2014.

[16] M. Mahnama, R. Naghdabadi, and M. R. Movahhedy, "Atomistic investigation of phase transition in solid argon induced by shock wave transmission," *Phase Transitions*, vol. 86, no. 8, pp. 838–853, Aug. 2013.

[17] N. Zhao, M. Sugiyama, and T. Ruggeri, "Phase transition induced by a shock wave in hard-sphere and hard-disk systems.," *J. Chem. Phys.*, vol. 129, no. 5, p. 54506, Aug. 2008.

[18] A. M. He, S. Q. Duan, J. L. Shao, P. Wang, and S. N. Luo, "Local and bulk melting of shocked columnar nanocrystalline Cu: Dynamics, anisotropy, premelting, superheating, supercooling, and re-crystallization.," *J. Chem. Phys.*, vol. 139, no. 7, p. 74502, Aug. 2013.

[19] G. D. Stevens, S. S. Lutz, B. R. Marshall, W. D. Turley, L. R. Veeser, R. S. Hixson, B. J. Jensen, P. A. Rigg, and M. D. Wilke, "Surface specularity as an indicator of shock-induced solid-liquid phase transitions in tin," *AIP Conference Proceedings*, vol. 955. pp. 201–204, 2007.

[20] J. W. Jeong and K. J. Chang, "Molecular-dynamics simulations for the shock Hugoniot meltings of Cu, Pd and Pt," *Journal of Physics: Condensed Matter*, vol. 11, no. 19. pp. 3799–3806, 17-May-1999.

[21] X. Cui, W. Zhu, H. He, X. Deng, and Y. Li, "Phase transformation of iron under shock compression: Effects of voids and shear stress," *Phys. Rev. B*, vol. 78, no. 2, p. 24115, Jul. 2008.

[22] T. C. Germann, "Large-scale classical molecular dynamics simulations of shock-induced plasticity in bcc niobium," *AIP Conference Proceedings*, vol. 1195. pp. 761–764, 2009.

[23] K. Kadau, T. C. Germann, P. S. Lomdahl, and B. L. Holian, "Atomistic simulations of shock-induced transformations and their orientation dependence in bcc Fe single crystals," *Phys. Rev. B*, vol. 72, no. 6, p. 64120, Aug. 2005.

[24] K. Kadau, F. J. Cherne, R. Ravelo, and T. C. Germann, "Shock-induced phase transformations in gallium single crystals by atomistic methods," *Phys. Rev. B*, vol. 88, no. 14, p. 144108, Oct. 2013.

[25] J. M. D. Lane and A. P. Thompson, "Molecular dynamics simulation of shock-induced phase transition in germanium," *AIP Conference Proceedings*, vol. 1195. pp. 1157–1160, 2009.

[26] Y. Lin, R. Perriot, V. V. Zhakhovsky, X. Gu, C. T. White, and I. I. Oleynik, "Shock-induced phase transition in diamond," *AIP Conference Proceedings*, vol. 1426. pp. 1171–1174, 2012.

[27] W. Pang, P. Zhang, G. Zhang, A. Xu, and X. Zhao, "Morphology and growth speed of hcp domains during shock-induced phase transition in iron.," *Sci. Rep.*, vol. 4, p. 3628, Jan. 2014.

[28] K. Wang, S. Xiao, H. Deng, W. Zhu, and W. Hu, "An atomic study on the shock-induced plasticity and phase transition for iron-based single crystals," *Int. J. Plast.*, vol. 59, pp. 180–198, Aug. 2014.

[29] H. Zong, T. Lookman, X. Ding, S. N. Luo, and J. Sun, "Anisotropic shock response of titanium: Reorientation and transformation mechanisms," *Acta Mater.*, vol. 65, pp. 10–18, Feb. 2014.

[30] H. Zong, X. Ding, T. Lookman, J. Li, J. Sun, E. K. Cerreta, A. P. Escobedo, F. L. Addessio, and C. A. Bronkhorst, "Collective nature of plasticity in mediating phase transformation under shock compression," *Phys. Rev. B*, vol. 89, no. 22, p. 220101, Jun. 2014.

[31] Y. Fang, C. Meng, W. Zhu, D. He, G. Du, and J. Jiang, “Shock-induced phase transitions of α-Ce3Al,” *J. Appl. Phys.*, vol. 113, no. 10, p. 103507, 2013.

[32] J. Hu, X. Zhou, C. Dai, H. Tan, and J. Li, “Shock-induced bct-bcc transition and melting of tin identified by sound velocity measurements,” *J. Appl. Phys.*, vol. 104, no. 8, p. 83520, 2008.

[33] H. Kishimura and H. Matsumoto, “Effect of phase transition in shock-recovered silicon,” *J. Appl. Phys.*, vol. 103, no. 2, p. 23505, 2008.

[34] Y. Ren, F. Wang, S. Wang, C. Tan, X. Yu, J. Jiang, and H. Cai, “Mechanical response and effects of β-to-α" phase transformation on the strengthening of Ti–10V–2Fe–3Al during one-dimensional shock loading,” *Mater. Sci. Eng. A*, vol. 562, pp. 137–143, Feb. 2013.

[35] E. Zaretsky, “High-temperature phase transformations: The properties of the phases under shock loading,” *AIP Conference Proceedings*, vol. 1426. pp. 1553–1558, 2012.

[36] A. V. Bolesta and V. M. Fomin, “Phase transition behind a shock front in polycrystalline copper,” *Dokl. Phys.*, vol. 59, no. 6, pp. 249–253, Jul. 2014.

[37] N. Gunkelmann, E. M. Bringa, K. Kang, G. J. Ackland, C. J. Ruestes, and H. M. Urbassek, “Polycrystalline iron under compression: Plasticity and phase transitions,” *Phys. Rev. B*, vol. 86, no. 14, p. 144111, Oct. 2012.

[38] N. Gunkelmann, E. M. Bringa, D. R. Tramontina, C. J. Ruestes, M. J. Suggit, A. Higginbotham, J. S. Wark, and H. M. Urbassek, “Shock waves in polycrystalline iron: Plasticity and phase transitions,” *Phys. Rev. B*, vol. 89, no. 14, p. 140102, 2014.

[39] N. Gunkelmann, D. R. Tramontina, E. M. Bringa, and H. M. Urbassek, “Interplay of plasticity and phase transformation in shock wave propagation in nanocrystalline iron,” *New J. Phys.*, vol. 16, no. 9, p. 93032, Sep. 2014.

[40] K. Kadau, T. C. Germann, P. S. Lomdahl, R. C. Albers, J. S. Wark, A. Higginbotham, and B. L. Holian, “Shock Waves in Polycrystalline Iron,” *Phys. Rev. Lett.*, vol. 98, no. 13, p. 135701, Mar. 2007.

[41] L. G. Wang, M. Šob, and Z. Zhang, “Instability of higher-energy phases in simple and transition metals,” *J. Phys. Chem. Solids*, vol. 64, no. 5, pp. 863–872, May 2003.

[42] T. Kraft, P. M. Marcus, M. Methfessel, and M. Scheffler, “Elastic constants of Cu and the instability of its bcc structure,” *Phys. Rev. B*, vol. 48, no. 9, pp. 5886–5890, 1993.

[43] Y. F. Wen and J. Sun, “Structural stability of higher-energy phases in Cu and Cu – Fe alloy revealed by ab initio calculations,” *Comput. Mater. Sci.*, vol. 79, pp. 463–467, 2013.

[44] I. A. Morrison, M. H. Kang, and E. J. Mele, “First-principles determination of the bulk phase diagram for body-centered-tetragonal copper: Application to epitaxial growth of Cu on Fe{100},” *Phys. Rev. B*, vol. 39, no. 3, pp. 1575–1580, 1989.

[45] L. G. Wang and M. Šob, “Structural stability of higher-energy phases and its relation to

the atomic configurations of extended defects: The example of Cu," *Phys. Rev. B*, vol. 60, no. 2, pp. 844–850, Jul. 1999.

[46] W. Mei, Y. Wen, H. Xing, P. Ou, and J. Sun, "Ab initio calculations of mechanical stability of bcc Cu under pressure," *Solid State Commun.*, vol. 184, pp. 25–28, 2014.

[47] M. H. Kang, B. C. Tatar, E. J. Mele, and P. Soven, "Real-space formulation of the mixed-basis pseudopotential method: Bulk structural properties of elemental copper," *Phys. Rev. B*, vol. 35, no. 11, 1987.

[48] S. Jeong, "Structural properties of bulk copper: Pseudopotential plane-wave-basis study," *Phys. Rev. B*, vol. 53, no. 21, pp. 13973–13976, 1996.

[49] Z. W. Lu, S. Wei, and A. Zunger, "Absence of volume metastability in bcc copper," *Phys. Rev. B*, vol. 41, no. 5, 1990.

[50] Y. Zhou, W. Lai, and J. Wang, "Calculated electronic structure of metastable of Cu.," *Phys. Rev. B*, vol. 49, no. 7, pp. 4463–4466, 1994.

[51] J. R. Chelikowsky and M.-Y. Chou, "The electronic and structural properties of elemental copper: A pseudopotential–local-orbital calculation," *Phys. Rev. B*, vol. 38, p. 7966, 1988.

[52] Z. Tang, M. Hasegawa, Y. Nagai, and M. Saito, "Density functional study on metastable bcc copper: Electronic structure and momentum density of positron-electron pairs," *Phys. Rev. B*, vol. 65, no. 19, p. 195108, Apr. 2002.

[53] S. Plimpton, "Fast Parallel Algorithms for Short-Range Molecular Dynamics," *J. Comp. Phys.*, vol. 117, no. 1, pp. 1–19, 1995.

[54] Y. M. Mishin, M. Mehl, D. Papaconstantopoulos, A. F. Voter, and J. Kress, "Structural stability and lattice defects in copper: Ab initio, tight-binding, and embedded-atom calculations," *Phys. Rev. B*, vol. 63, no. 22, p. 224106, May 2001.

[55] B. L. Holian and P. S. Lomdahl, "Plasticity Induced by Shock Waves in Nonequilibrium Molecular-Dynamics Simulations," *Science*, vol. 280, no. 5372, pp. 2085–2088, Jun. 1998.

[56] A. Bolesta, L. Zheng, D. Thompson, and T. Sewell, "Molecular dynamics simulations of shock waves using the absorbing boundary condition: A case study of methane," *Phys. Rev. B*, vol. 76, no. 22, p. 224108, Dec. 2007.

[57] A. Stukowski, "Structure identification methods for atomistic simulations of crystalline materials," *Model. Simul. Mater. Sci. Eng.*, vol. 20, no. 4, p. 45021, Jun. 2012.

[58] A. Stukowski, "Visualization and analysis of atomistic simulation data with OVITO–the Open Visualization Tool," *Model. Simul. Mater. Sci. Eng.*, vol. 18, no. 1, p. 15012, Jan. 2010.

[59] J.A. Moriarty, *Shock Waves in Condensed Matter*. New York, 1986.

[60] D. Hayes, R. S. Hixson, and R. G. McQueen, “High pressure elastic properties, solid-liquid phase boundary and liquid equation of state from release wave measurements in shock-loaded copper,” *AIP Conf. Proc.*, vol. 505, pp. 483–488, 2000.

[61] X. W. Zhou, H. N. G. Wadley, R. A. Johnson, D. J. Larson, N. Tabat, A. Cerezo, A. K. Petford-Long, G. D. W. Smith, P. H. Clifton, R. L. Martens, and T. F. Kelly, “Atomic scale structure of sputtered metal multilayers,” *Acta Mater.*, vol. 49, no. 19, pp. 4005–4015, 2001.

[62] S. Foiles, M. Baskes, and M. Daw, “Embedded-atom-method functions for the fcc metals Cu, Ag, Au, Ni, Pd, Pt, and their alloys,” *Phys. Rev. B*, vol. 33, no. 12, pp. 7983–7991, Jun. 1986.

[63] A. Belonoshko, R. Ahuja, O. Eriksson, and B. Johansson, “Quasi ab initio molecular dynamic study of Cu melting,” *Phys. Rev. B*, vol. 61, no. 6, pp. 3838–3844, Feb. 2000.

[64] V. Paidar, L. G. Wang, M. Sob, and V. Vitek, “A study of the applicability of many-body central force potentials in NiAl and TiAl,” *Model. Simul. Mater. Sci. Eng.*, vol. 7, no. 3, pp. 369–381, May 1999.

Appendix 5.1

AUTHOR AND USER RIGHTS

INTRODUCTION

Elsevier requests transfers of copyright, or in some cases exclusive rights, from its journal authors in order to ensure that we have the rights necessary for the proper administration of electronic rights and online dissemination of journal articles, authors and their employers retain (or are granted/transferred back) significant scholarly rights in their work. We take seriously our responsibility as the steward of the online record to ensure the integrity of scholarly works and the sustainability of journal business models, and we actively monitor and pursue unauthorized and unsubscribed uses and re-distribution (for subscription models).

In addition to authors' scholarly rights, anyone who is affiliated with an institution with a journal subscription can use articles from subscribed content under the terms of their institution's license, while there are a number of other ways in which anyone (whether or not an author or subscriber) can make use of content published by Elsevier, which is free at the point of use or accessed under license.

Author Rights

As a journal author, you have rights for a large range of uses of your article, including use by your employing institute or company. These rights can be exercised without the need to obtain specific permission.

How authors can use their own journal articles

Authors publishing in Elsevier journals have wide rights to use their works for teaching and scholarly purposes without needing to seek permission.

Table of Author's Rights

	Preprint version	Accepted Author Manuscript	Published Journal Articles
Use for classroom teaching by author or author's institution and presentation at a meeting or conference and distributing copies to attendees	Yes	Yes	Yes
Use for internal training by author's company	Yes	Yes	Yes

Use in a subsequent compilation of the author's works	Yes	Yes	Yes
Inclusion in a thesis or dissertation	Yes	Yes	Yes
Reuse of portions or extracts from the article in other works	Yes	Yes with full acknowledgement of final article	Yes with full acknowledgement of final article
Preparation of derivative works (other than for commercial purposes)	Yes	Yes with full acknowledgement of final article	Yes with full acknowledgement of final article
Preprint servers	Yes	Yes with the specific written permission of Elsevier	No
Voluntary posting on open web sites operated by author or author's institution for scholarly purposes	Yes (author may later add an appropriate bibliographic citation, indicating subsequent publication by Elsevier and journal title)	Yes, with appropriate bibliographic citation and a link to the article once published	Only with the specific written permission of Elsevier
Mandated deposit or deposit in or posting to subject-oriented or centralized repositories	Yes under specific agreement between Elsevier and the repository	Yes under specific agreement between Elsevier and the repository**	Yes under specific agreement between Elsevier and the repository
Use or posting for commercial gain or to substitute for services provided directly by journal	Only with the specific written permission of Elsevier	Only with the specific written permission of Elsevier	Only with the specific written permission of Elsevier

** Voluntary posting of Accepted Author Manuscripts in the arXiv subject repository is permitted.

Chapter 6: Characterization of Unshocked Nanocrystalline and Shocked Single Crystal Cu by Virtual Diffraction Simulations

Abstract

Simulated x-ray diffraction line profiles and SAED patterns are presented for unshocked nanocrystalline Cu models at 0 K temperature with different grain diameters and number of grains. The Williamson-Hall analysis is used to characterize the x-ray diffraction line profiles and predict the microstrain and the mean grain diameter of the nanocrystalline models. This analysis is applied for six models containing 20 and 50 grains with mean grain diameters of 5, 10 and 15 nm. For simulations containing the same number of grains, the values of the microstrain decrease with increasing the grain diameter. This is due to a smaller fraction of atoms are distorted by grain boundaries for models with larger grains. To extend the virtual diffraction data to shock simulations, x-ray diffraction line profiles are created for <100> shock models of single crystal Cu at the Hugoniot state. For these shock simulations, a range of particle velocities from 0.7 to 1.0 km/s is performed with initial temperatures of 5, 300 and 600 K. Generally, peak broadening in the x-ray diffraction line profiles increases with increasing particle velocity, which is partially due to the increase in dislocation density.

6.1 Introduction

X-ray diffraction (XRD) is a powerful technique to characterize plastic deformations in solid materials. There are several methods [1–3] to quantify the microscopic properties of materials, such as grains size and microstrain, based on x-ray diffraction line profile data. For example,

Williamson and Hall [1] developed an analysis method based on peak broadenings and peak locations of the x-ray diffraction line profile to determine an approximation for average grain size and microstrain inside the microstructure. Even though the implementation of this method is easy, the Williamson-Hall analysis only considers the width of peaks instead of the whole peaks profile shape in the x-ray diffraction line profile. To include the information of whole peaks profile shape, Warren and Averbach [2] developed an analysis to obtain grain size and microstrain based on the Fourier transforms of the peak profiles. However, extracting more reliable information related to the plastic deformations of microstructure, such as dislocation density and planar defect densities, by using these basic characterization analyses is impossible. Thus, more advanced analyses [4,5] are necessary to quantify the microscopic properties of materials based on x-ray diffraction line profile data. For example, Ribarik et al. [5] proposed the Convolutional Multiple Whole Profile (CMWP) analysis to fit x-ray diffraction line profile with theoretical ab initio functions to obtain grain size, dislocation density and planar defect densities (stacking faults and twin boundaries).

For shock in solid materials, several experimental studies have been done to characterize macroscopic properties of shocked solid materials using XRD method, including phase transformation [6–8] and strength of materials subjected to shock loading [9–11]. However, there are very few studies that quantify microscopic plastic properties of shocked solid materials using XRD method, including calculation of dislocation density [10,12], microstrain [13] and polycrystalline grain size [8,10]. For example, Turneaure et al. [13] used a real-time x-ray diffraction method to obtain microstructural information for <100> shock in single crystal Al up to 7.1 GPa pressure using plate impact loading. They used the Williamson-Hall and the Profile Synthesis [14] methods to analyze the x-ray diffraction line profile and determine the microstrain

behind the shock front. In addition, Ahn et al. [10] obtained the grain size and dislocation density of shocked ultrafine copper after analyzing the x-ray diffraction line profile by CMWP method.

On the other hand, Rosolankova et al. [15] calculated dislocation density behind the <100> shock wave front of single crystal Cu using simulated x-ray diffraction method based on a large MD simulation done by Bringa et al. [16]. There were two preexisting prismatic sources of dislocation (heterogeneous dislocation nucleation) in their MD model. They performed a single particle velocity of 0.75 km/s (above the HEL) with 50 ps ramp loading time to create shock wave in a MD model with 256 million atoms. To calculate the dislocation density with analyzing the simulated x-ray diffraction data, they compared the results from the second and the fourth diffraction orders. However, they calculated dislocation density behind the shock front only at 0.75 km/s particle velocity, and they did not calculate the twin boundary density.

The objective for Chapter 6 is to perform the virtual (simulated) diffraction method developed by Coleman et al. [17], and produce x-ray diffraction line profile and selected area electron diffraction (SAED) data for several nanocrystalline models at 0 K temperature. To analyze the x-ray diffraction line profile data and obtain the grain size and the microstrain inside the microstructures, the Williamson-Hall analysis is applied. Note, these results are extracted from the research paper [18] which was collaborative with Shawn P. Coleman, but they were done by the author of this dissertation. To extend the diffraction results for shock simulations, the virtual x-ray diffraction is performed for MD results of <100> shock of single crystal Cu at particle velocities from 0.7 to 1.0 km/s and initial temperatures of 5, 300, and 600 K at the Hugoniot state. Analysis of these data by CMWP method can predict the dislocation density and the planar defect densities behind the shock front. While XRD plots will be provided in this

work, the complete analysis of this data for contributions of dislocation density, twin density and temperature effects is beyond the scope of this dissertation.

6.2 Methodology

X-ray diffraction line profiles and SAED patterns are created for nanocrystalline Cu samples with different grain diameters and number of grains using the virtual diffraction method [17]. The different nanocrystalline samples are constructed using the Voronoi method to create a random distribution of grain orientations within fully periodic, cubic simulation cells. The Voronoi method requires the user to specify a target mean grain size and uses this value to determine the number and distribution of grain centers within the simulation cell. There is no guarantee that the true mean grain diameter resulting from the Voronoi construction algorithm will be exactly equal to the user-defined target value. Within each nanocrystalline sample, the atomic interactions are modeled using the Cu EAM potential parameterized by Mishin et al. [19]. Before computing the virtual diffraction patterns, the atomic structures are relaxed at 0 K temperature using a non-linear conjugate gradient method in LAMMPS [20].

In addition, the virtual x-ray diffraction is performed for MD results of <100> shock of single crystal Cu at particle velocities from 0.7 to 1.0 km/s and initial temperatures of 5, 300 and 600 K at the Hugoniot state. Single crystal Cu models have lengths of 21.69, 21.69 and 108.45 nm in the X-, Y- and Z-directions, respectively, containing 4,320,000 atoms. Detailed information regarding boundary conditions, simulation equilibration and simulation validation is provided in Chapter 3.

6.3 Results and Discussion

6.3.1 Nanocrystalline Models

X-ray diffraction line profiles are constructed for each nanocrystalline Cu sample using a mesh resolution of approximately 4.7 x 10^7 reciprocal lattice points per $Å^{-3}$. Figure 6.1 shows a representative x-ray diffraction line profile for a nanocrystalline sample containing 300 grains with a target mean grain diameter of 5 nm. Four peaks are observed at 2θ locations 43.29°, 50.43°, 74.15° and 89.96° which correspond to the interplanar distances associated with {111}, {200}, {220} and {311} planes, respectively. These peak locations are a close match to the predicted locations computed using Bragg's Law for single crystal Cu with a lattice parameter of 3.615 Å [19], indicating that there is no net tensile or compressive strain in the nanocrystalline samples after the Voronoi construction and energy minimization procedures.

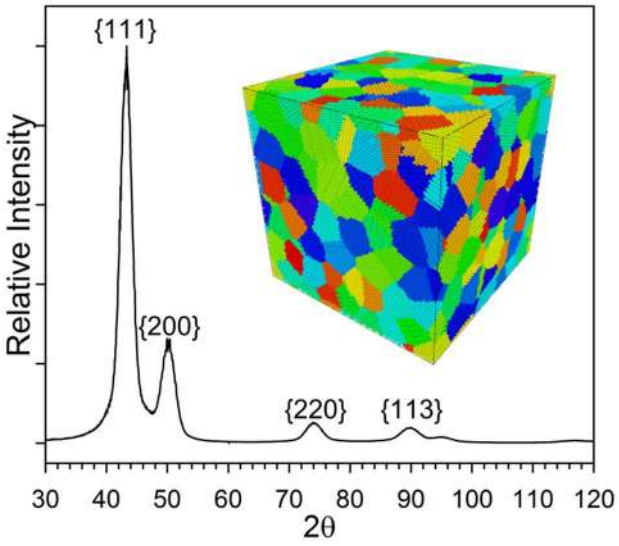

Figure 6.1: XRD pattern for a nanocrystalline Cu sample with 300 grains and 5 nm mean grain diameter [18]. The nanocrystalline sample is shown in the inset colored by grain number.

Peak locations and broadening from the virtual x-ray diffraction line profiles are used to perform a Williamson-Hall analysis to predict microstrain in the lattice due to the grain boundaries as well as the true mean grain diameter of the nanocrystalline samples. This analysis is performed for six samples containing 20 and 50 grains with target mean grain diameters of 5, 10 and 15 nm. Both Lorentzian and Lorentzian-Gaussian distributions are fit to the x-ray diffraction peaks using the Fityk software [21], which provides peak location and peak broadening information. It is found that the Lorentzian-Gaussian distribution provides a closer approximation to the peak maxima and shapes through minimization of the residuals between the computed diffraction data and each fitted distribution. Figure 6.2 shows a Williamson-Hall plot using the Lorentzian-Gaussian fit to the virtual diffraction data.

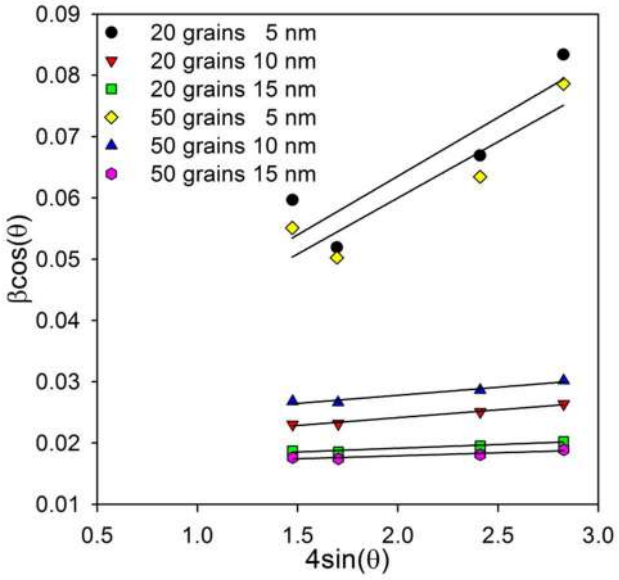

Figure 6.2: Williamson-Hall analysis for six different samples using Lorentzian-Gaussian fitting of the diffraction peaks [18].

The true mean grain diameter and the microstrain are extracted via a linear fit and are reported in Table 6.1 for the six different samples using both Lorentzian and Lorentzian-Gaussian fittings. For the 5 nm model, the true mean grain diameter is larger than the target grain diameter used during Voronoi construction and the microstrain within each nanocrystalline model is non-homogeneous as evident by the non-linearity of the data. On the other hand, for the 10 and 15 nm samples, the true mean grain diameter predicted with the Lorentzian-Gaussian distribution is smaller than the target grain diameter and data is linear, implying that the root-mean-squared microstrain is isotropic. These observations are consistent with work of Derlet et al. [22]. For simulations containing the same number of grains, the magnitude of the microstrain decreases in models built with increasing target grain diameter. This is attributed to the smaller fraction of atoms within the larger nanocrystalline samples whose lattice positions are distorted by the grain boundaries. Models constructed with the same target mean grain diameter show negligible dependence of the microstrain on the number of grains.

Table 6.1**:** True mean grain diameter (nm) and microstrain predicted from the Williamson-Hall analysis using different peak fitting functions [18].

Target Grain	**20 grains**				**50 grains**			
Diameter	**Microstrain**		**True Diameter**		**Microstrain**		**True Diameter**	
5 nm	0.0188[a],	0.0192[b]	6.64[a],	6.12[b]	0.0186[a],	0.0183[b]	7.79[a],	6.59[b]
10 nm	0.0040[a],	0.0026[b]	10.85[a],	8.11[b]	0.0040[a],	0.0026[b]	8.43[a],	6.85[b]
15 nm	0.0020[a],	0.0012[b]	11.01[a],	9.23[b]	0.0018[a],	0.0010[b]	11.59[a],	9.70[b]

[a] X-ray diffraction peaks fit to a Lorentzian distribution.
[b] X-ray diffraction peaks fit to a Lorentzian-Gaussian distribution.

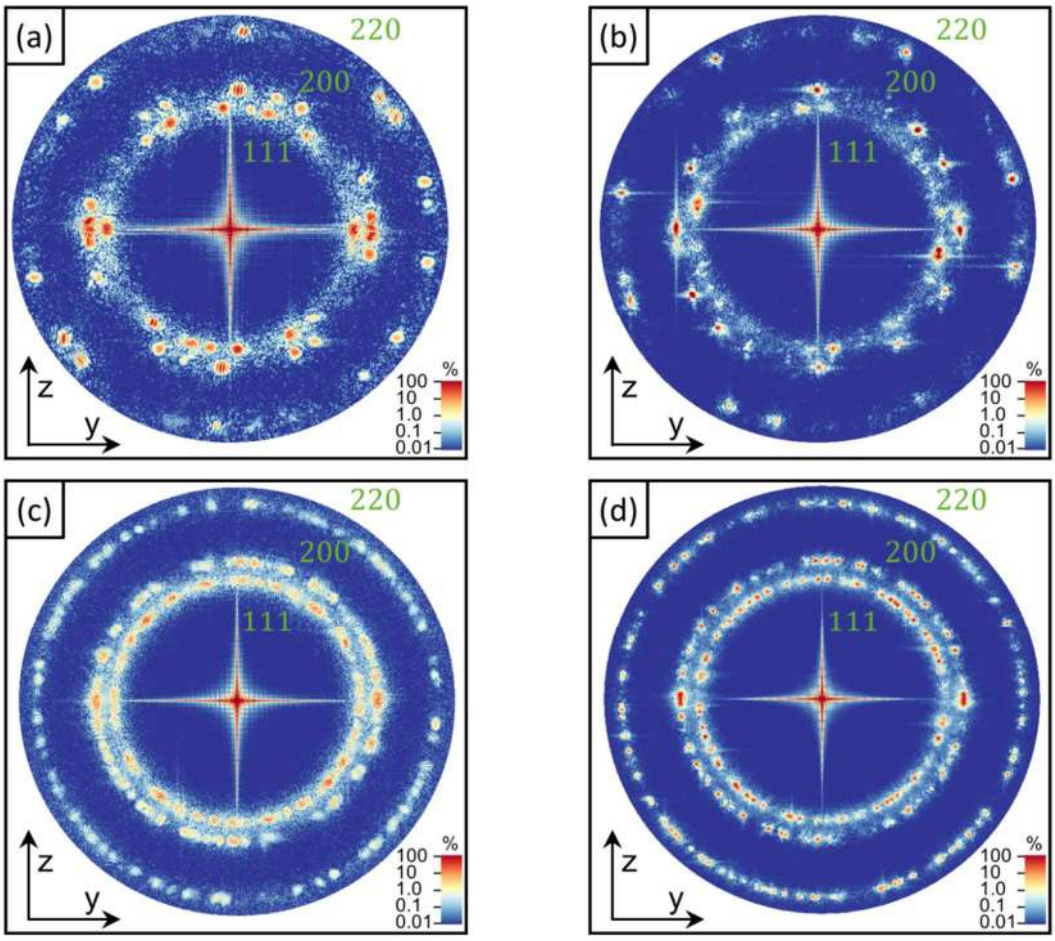

Figure 6.3: SAED pattern for nanocrystalline Cu models containing 50 grains having (a) 5 nm and (b) 10 nm grain diameter as well as 400 grain models with (c) 5 nm and (d) 10 nm grain diameter [18].

Figure 6.3 shows SAED patterns generated with zone-axes oriented along the [100] direction for simulations containing 50 and 400 grains using target mean grain diameters of 5 and 10 nm. Each SAED pattern contains three rings associated with the {111}, {200} and {220} planes, as expected from experimental results which were performed on a thin copper film containing 45 nm grains [23]. In the 400 grain models the rings are more complete as compared with the 50 grain models implying that models with a larger number of grains are statistically more representative of nanocrystalline samples with random grain orientations. In addition, the rings in

the 10 nm samples are thinner than the rings in the 5 nm samples because of microstrain effects, analogous to the role of microstrain on peak broadening in the x-ray diffraction line profiles.

6.3.2 Single Crystal Shock Models

To extend the diffraction data for <100> shock simulations, x-ray diffraction line profiles are constructed for each shocked single crystal Cu model at the Hugoniot state using a mesh resolution of approximately 2.14 x 10^8 reciprocal lattice points per $Å^{-3}$. These MD models are corresponding to <100> shock with particle velocities range from 0.7 to 1.0 km/s and initial temperatures of 5, 300 and 600 K. Figure 6.4 shows a x-ray diffraction line profile for a model with particle velocity of 0.8 km/s and initial temperature of 300 K. In Figure 6.4, the first four peaks are observed at 2θ locations 45.87°, 52.69°, 78.92° and 96.00° which correspond to the interplanar distances associated with {111}, {200}, {220} and {311} planes, respectively. Note, the peak locations and the peak broadenings are obtained through a Lorentzian-Gaussian fitting procedure in Fityk software. Using the Bragg's Law for perfect Cu crystal, the first four peaks should be located at 43.35°, 50.49°, 74.19° and 90.02°. The shift in the location of peaks in x-ray diffraction line profile of shocked models compared to the perfect Cu crystal is due to the compression of microstructure during shock.

Several factors influence the peak broadening in x-ray diffraction line profile, including the existence of grains [22] and crystal defects [24,25] in the microstructure. For example, Derlet et al. [22] simulated a x-ray diffraction line profile for nanocrystalline Ni models with 5 and 12 nm grain size, and reported broader peaks for a model with 5 nm grains size. In addition, experimental researchers reported peak broadening due to the dislocation network during plastic

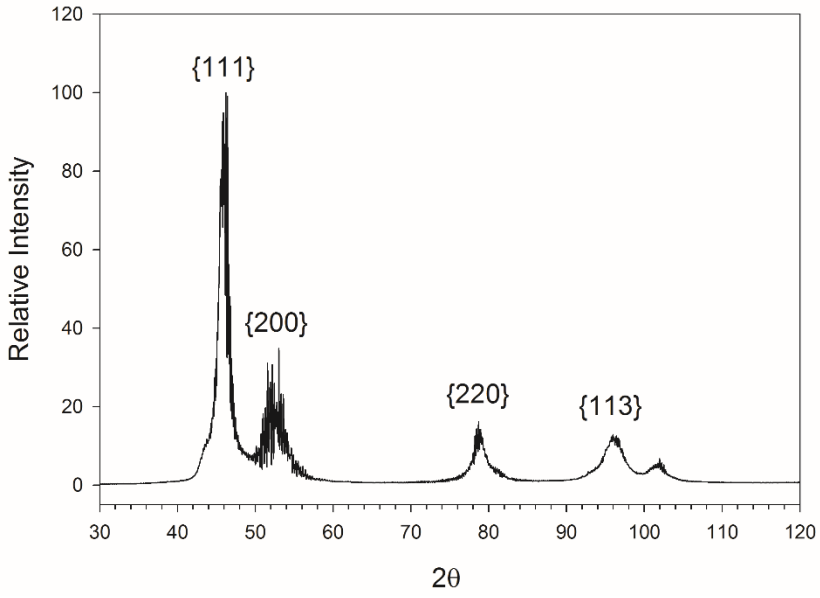

Figure 6.4: XRD pattern for a single crystal Cu during <100> shock at the Hugoniot state with a particle velocity of 0.8 km/s and an initial temperature of 300 K.

deformation of nanocrystalline Ni samples, which was reversible at room temperature [24] and was irreversible at 180 K temperature [25]. Since there is no grain in the shock models of single crystal Cu, the peak broadening in the x-ray diffraction line profiles in the current study is due to the emergence of dislocations, twins and stacking faults behind the <100> shock front. Detailed information regarding the generation of dislocations and other defects behind the <100> shock front was presented in Chapter 3.

Figure 6.5 shows the relationship between integral width and particle velocity of the first three peaks in x-ray diffraction line profiles for several initial temperatures. For particle velocities from 0.7 to 0.9 km/s, the integral width for these three peaks generally increases with increasing particle velocity. This increase in integral width partially can be justified by increase

in dislocation density, which was discussed in Chapter 3. The integral widths associated with particle velocity of 1.0 km/s are generally smaller than values at 0.9 km/s. This can be correlated with the observation of large regions of HCP crystal, which is an artifact of the EAM interatomic potential (Chapter 4). However, the plastic deformation behind the <100> shock is complicated due to the emergence of several dislocation types, twins and stacking faults as well as the influence of temperature on these defects. Thus, an advanced characterization method (such as CMWP) is necessary to quantify the influence of each factor on the peak broadening of x-ray diffraction line profile.

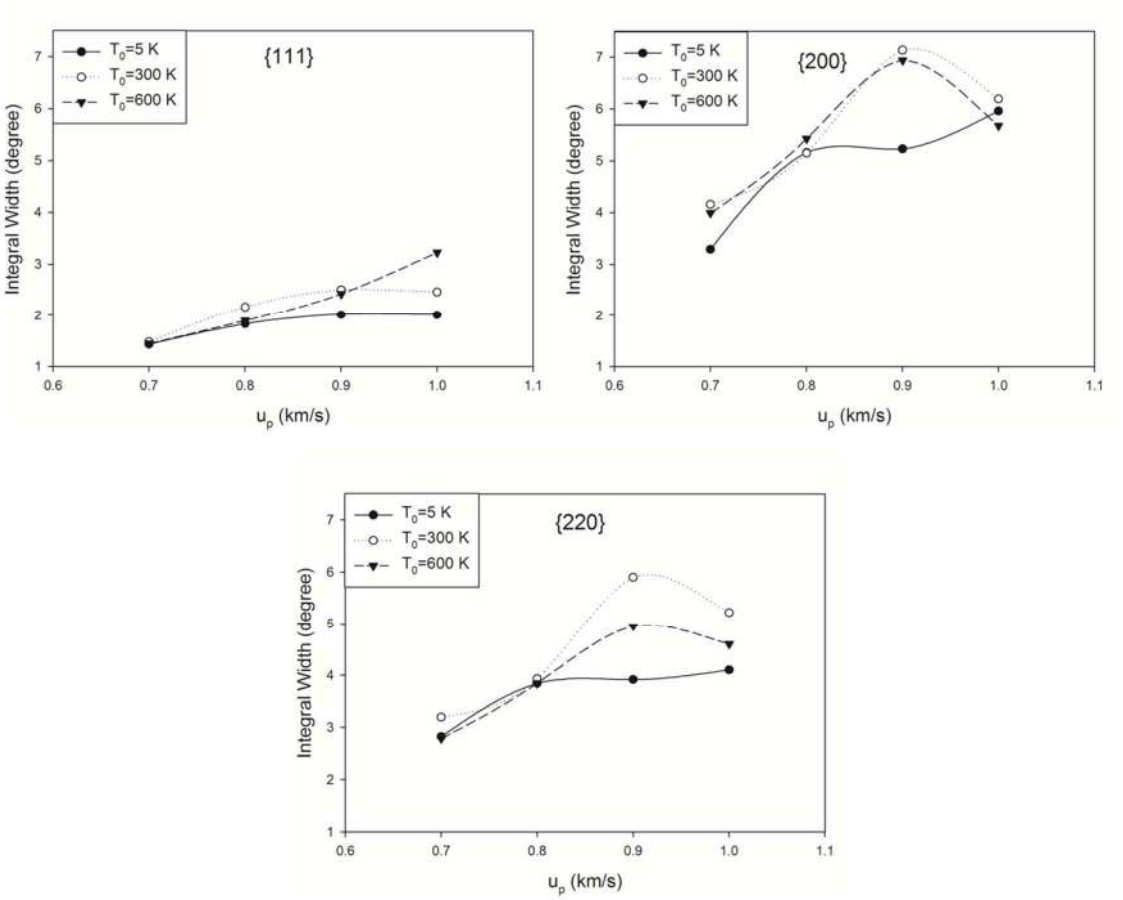

Figure 6.5: Relationship between integral width of peaks in XRD patterns and particle velocity for several initial temperatures.

6.4 Conclusions

X-ray diffraction line profiles and SAED patterns are created for nanocrystalline Cu models containing grains with mean diameters of 5, 10 and 15 nm at 0 K temperature. To analyze the x-ray diffraction line profiles and obtain the microstrain and the mean grain diameter of the microstructure, the Williamson-Hall analysis is applied. The magnitudes of the microstrain decrease with increasing the grain diameter for models with the same number of grains. This can be justified by distortion of a smaller fraction of atoms with grain boundaries for models with larger grains. Each SAED pattern contains three rings associated with the {111}, {200} and {220} planes, and the rings in models with larger grains are thinner because of microstrain effects. This is analogous to the role of microstrain on peak broadening in the x-ray diffraction line profiles. In addition, the x-ray diffraction line profiles are created for <100> shock models of single crystal Cu at the Hugoniot state with particle velocities from 0.7 to 1.0 km/s and initial temperatures of 5, 300 and 600 K. Generally, the peak broadening in the x-ray diffraction line profiles increases with increasing particle velocity, which is partially due to the increase in dislocation density.

Acknowledgments

Support of the 21st Century Professorship in Mechanical Engineering and the Department of Mechanical Engineering at the University of Arkansas is greatly appreciated. Simulations in this work were performed on high performance computing equipment supported in part by National Science Foundation grants ARI #0963249, MRI #0959124, EPS #0918970, and a grant from the

Arkansas Science and Technology Authority, managed by the University of Arkansas, Arkansas High Performance Computing Center.

References

[1] G. K. Williamson and W. H. Hall, "X-ray line broadening from filed aluminium and wolfram," *Acta Metall.*, vol. 1, no. 1, pp. 22–31, Jan. 1953.

[2] B. E. Warren and B. L. Averbach, "The Effect of Cold-Work Distortion on X-Ray Patterns," *J. Appl. Phys.*, vol. 21, no. 6, pp. 595–599, Jun. 1950.

[3] A. J. C. Wilson, "On Variance as a Measure of Line Broadening in Diffractometry General Theory and Small Particle Size," *Proc. Phys. Soc.*, vol. 80, no. 1, pp. 286–294, 1962.

[4] G. Ribárik, T. Ungár, and J. Gubicza, "MWP-fit : a program for multiple whole-profile fitting of diffraction peak profiles by ab initio theoretical functions," *J. Appl. Crystallogr.*, vol. 34, no. 5, pp. 669–676, Oct. 2001.

[5] G. Ribárik, J. Gubicza, and T. Ungár, "Correlation between strength and microstructure of ball-milled Al–Mg alloys determined by X-ray diffraction," *Mater. Sci. Eng. A*, vol. 387–389, no. 1–2 SPEC. ISS., pp. 343–347, Dec. 2004.

[6] D. J. Funk, C. A. Meserole, D. E. Hof, G. L. Fisher, J. Roberts, A. J. Taylor, H. J. Lee, J. Workman, and Q. McCulloch, "An Ultrafast X-Ray Diffraction Apparatus for the Study of Shock Waves," in *AIP Conference Proceedings*, 2004, vol. 706, no. May 2015, pp. 1155–1158.

[7] J. Hawreliak, M. Butterfield, H. Davies, B. El-Dasher, A. Higginbotham, D. Kalantar, G. Kimminau, J. McNaney, D. Milathianaki, W. Murphy, B. Nagler, N. Park, B. Remington, L. Thorton, T. Whitcher, J. Wark, and H. Lorenzana, "IN-SITU PROBING OF LATTICE RESPONSE IN SHOCK COMPRESSED MATERIALS USING X-RAY DIFFRACTION," in *AIP Conference Proceedings*, 2008, vol. 955, pp. 1327–1332.

[8] J. A. Hawreliak, D. H. Kalantar, J. S. Stölken, B. A. Remington, H. E. Lorenzana, and J. S. Wark, "High-pressure nanocrystalline structure of a shock-compressed single crystal of iron," *Phys. Rev. B*, vol. 78, no. 22, p. 220101, Dec. 2008.

[9] A. J. Comley, B. R. Maddox, R. E. Rudd, S. T. Prisbrey, J. A. Hawreliak, D. A. Orlikowski, S. C. Peterson, J. H. Satcher, A. J. Elsholz, H.-S. Park, B. A. Remington, N. Bazin, J. M. Foster, P. Graham, N. Park, P. A. Rosen, S. R. Rothman, A. Higginbotham, M. Suggit, and J. S. Wark, "Strength of Shock-Loaded Single-Crystal Tantalum [100] Determined using In Situ Broadband X-Ray Laue Diffraction," *Phys. Rev. Lett.*, vol. 110,

no. 11, p. 115501, Mar. 2013.

[10] D.-H. Ahn, W. Kim, M. Kang, L. J. Park, S. Lee, and H. S. Kim, “Plastic deformation and microstructural evolution during the shock consolidation of ultrafine copper powders,” *Mater. Sci. Eng. A*, vol. 625, pp. 230–244, Feb. 2015.

[11] W. J. Murphy, A. Higginbotham, G. Kimminau, B. Barbrel, E. M. Bringa, J. Hawreliak, R. Kodama, M. Koenig, W. McBarron, M. A. Meyers, B. Nagler, N. Ozaki, N. Park, B. Remington, S. Rothman, S. M. Vinko, T. Whitcher, and J. S. Wark, “The strength of single crystal copper under uniaxial shock compression at 100 GPa,” *J. Phys. Condens. Matter*, vol. 22, no. 6, p. 65404, Feb. 2010.

[12] A. M. Podurets, M. I. Tkachenko, O. N. Ignatova, A. I. Lebedev, V. V. Igonin, and V. A. Raevskii, “Dislocation density in copper and tantalum subjected to shock compression depending on loading parameters and original microstructure,” *Phys. Met. Metallogr.*, vol. 114, no. 5, pp. 440–447, May 2013.

[13] S. J. Turneaure and Y. M. Gupta, “Real-time microstructure of shock-compressed single crystals from X-ray diffraction line profiles,” *J. Appl. Crystallogr.*, vol. 44, no. 3, pp. 574–584, Jun. 2011.

[14] P. Scardi, M. Leoni, and Y. H. Dong, “Whole diffraction pattern-fitting of polycrystalline fcc materials based on microstructure,” *Eur. Phys. J. B*, vol. 18, no. 1, pp. 23–30, Nov. 2000.

[15] K. Rosolankova, J. S. Wark, E. M. Bringa, and J. Hawreliak, “Measuring stacking fault densities in shock-compressed FCC crystals using in situ x-ray diffraction,” *J. Phys. Condens. Matter*, vol. 18, no. 29, pp. 6749–6757, Jul. 2006.

[16] E. M. Bringa, K. Rosolankova, R. E. Rudd, B. A. Remington, J. S. Wark, M. Duchaineau, D. H. Kalantar, J. Hawreliak, and J. Belak, “Shock deformation of face-centred-cubic metals on subnanosecond timescales,” *Nat. Mater.*, vol. 5, no. 10, pp. 805–809, Oct. 2006.

[17] S. P. Coleman, D. E. Spearot, and L. Capolungo, “Virtual diffraction analysis of Ni [0 1 0] symmetric tilt grain boundaries,” *Model. Simul. Mater. Sci. Eng.*, vol. 21, no. 5, p. 55020, Jul. 2013.

[18] S. P. Coleman, M. M. Sichani, and D. E. Spearot, “A Computational Algorithm to Produce Virtual X-ray and Electron Diffraction Patterns from Atomistic Simulations,” *Jom*, vol. 66, no. 3, pp. 408–416, Jan. 2014.

[19] Y. M. Mishin, M. Mehl, D. Papaconstantopoulos, A. F. Voter, and J. Kress, “Structural stability and lattice defects in copper: Ab initio, tight-binding, and embedded-atom calculations,” *Phys. Rev. B*, vol. 63, no. 22, p. 224106, May 2001.

[20] S. Plimpton, “Fast Parallel Algorithms for Short-Range Molecular Dynamics,” *J. Comp. Phys.*, vol. 117, no. 1, pp. 1–19, 1995.

[21] M. Wojdyr, “Fityk : a general-purpose peak fitting program,” *J. Appl. Crystallogr.*, vol.

43, no. 5, pp. 1126–1128, Oct. 2010.

[22] P. M. Derlet, S. Van Petegem, and H. Van Swygenhoven, “Calculation of x-ray spectra for nanocrystalline materials,” *Phys. Rev. B*, vol. 71, no. 2, p. 24114, Jan. 2005.

[23] S. Simões, R. Calinas, M. T. Vieira, M. F. Vieira, and P. J. Ferreira, “In situ TEM study of grain growth in nanocrystalline copper thin films,” *Nanotechnology*, vol. 21, no. 14, p. 145701, Apr. 2010.

[24] Z. Budrovic, H. V. Swygenhoven, P. M. Derlet, S. V. Petegem, and B. Schmitt, “Plastic Deformation with Reversible Peak Broadening in Nanocrystalline Nickel,” *Science*, vol. 304, no. 5668, pp. 273–276, Apr. 2004.

[25] S. Brandstetter, Ž. Budrović, S. Van Petegem, B. Schmitt, E. Stergar, P. M. Derlet, and V. H. Swygenhoven, “Temperature-dependent residual broadening of x-ray diffraction spectra in nanocrystalline plasticity,” *Appl. Phys. Lett.*, vol. 87, no. 23, p. 231910, Dec. 2005.

Appendix 6.1

SPRINGER LICENSE
TERMS AND CONDITIONS

Mar 21, 2017

This Agreement between Mehrdad Mirzaei Sichani ("You") and Springer ("Springer") consists of your license details and the terms and conditions provided by Springer and Copyright Clearance Center.

License Number	4073790615556
License date	Mar 21, 2017
Licensed Content Publisher	Springer
Licensed Content Publication	JOM Journal of the Minerals, Metals and Materials Society
Licensed Content Title	A Computational Algorithm to Produce Virtual X-ray and Electron Diffraction Patterns from Atomistic Simulations
Licensed Content Author	Shawn P. Coleman
Licensed Content Date	Jan 1, 2013
Licensed Content Volume	66
Licensed Content Issue	3
Type of Use	Thesis/Dissertation
Portion	Excerpts
Author of this Springer article	Yes and you are the sole author of the new work
Order reference number	None
Title of your thesis / dissertation	Characterization of Plastic Deformation Evolution in Single Crystal and Nanocrystalline Cu during Shock by Atomistic Simulations
Expected completion date	May 2017
Estimated size (pages)	200
Total	0.00 USD

Terms and Conditions

Introduction
The publisher for this copyrighted material is Springer. By clicking "accept" in connection with completing this licensing transaction, you agree that the following terms and conditions apply to this transaction (along with the Billing and Payment terms and conditions established by Copyright Clearance Center, Inc. ("CCC"), at the time that you opened your Rightslink account and that are available at any time at http://myaccount.copyright.com).

Limited License
With reference to your request to reuse material on which Springer controls the copyright, permission is granted for the use indicated in your enquiry under the following conditions:

- Licenses are for one-time use only with a maximum distribution equal to the number stated in your request.

- Springer material represents original material which does not carry references to other sources. If the material in question appears with a credit to another source, this permission is not valid and authorization has to be obtained from the original copyright holder.

- This permission
• is non-exclusive
• is only valid if no personal rights, trademarks, or competitive products are infringed.
• explicitly excludes the right for derivatives.

- Springer does not supply original artwork or content.

- According to the format which you have selected, the following conditions apply accordingly:
• Print and Electronic: This License include use in electronic form provided it is password protected, on intranet, or CD-Rom/DVD or E-book/E-journal. It may not be republished in electronic open access.
• Print: This License excludes use in electronic form.
• Electronic: This License only pertains to use in electronic form provided it is password protected, on intranet, or CD-Rom/DVD or E-book/E-journal. It may not be republished in electronic open access.
For any electronic use not mentioned, please contact Springer at permissions.springer@spi-global.com.

- Although Springer controls the copyright to the material and is entitled to negotiate on rights, this license is only valid subject to courtesy information to the author (address is given in the article/chapter).

- If you are an STM Signatory or your work will be published by an STM Signatory and you are requesting to reuse figures/tables/illustrations or single text extracts, permission is granted according to STM Permissions Guidelines: http://www.stm-assoc.org/permissions-guidelines/
For any electronic use not mentioned in the Guidelines, please contact Springer at permissions.springer@spi-global.com. If you request to reuse more content than stipulated in the STM Permissions Guidelines, you will be charged a permission fee for the excess content.

Permission is valid upon payment of the fee as indicated in the licensing process. If permission is granted free of charge on this occasion, that does not prejudice any rights we might have to charge for reproduction of our copyrighted material in the future.

-If your request is for reuse in a Thesis, permission is granted free of charge under the following conditions:

This license is valid for one-time use only for the purpose of defending your thesis and with a maximum of 100 extra copies in paper. If the thesis is going to be published, permission needs to be reobtained.
- includes use in an electronic form, provided it is an author-created version of the thesis on his/her own website and his/her university's repository, including UMI (according to the definition on the Sherpa website: http://www.sherpa.ac.uk/romeo/);
- is subject to courtesy information to the co-author or corresponding author.

Geographic Rights: Scope
Licenses may be exercised anywhere in the world.

Altering/Modifying Material: Not Permitted
Figures, tables, and illustrations may be altered minimally to serve your work. You may not alter or modify text in any manner. Abbreviations, additions, deletions and/or any other alterations shall be made only with prior written authorization of the author(s).

Reservation of Rights
Springer reserves all rights not specifically granted in the combination of (i) the license details provided by you and accepted in the course of this licensing transaction and (ii) these terms and conditions and (iii) CCC's Billing and Payment terms and conditions.

License Contingent on Payment
While you may exercise the rights licensed immediately upon issuance of the license at the end of the licensing process for the transaction, provided that you have disclosed complete and accurate details of your proposed use, no license is finally effective unless and until full payment is received from you (either by Springer or by CCC) as provided in CCC's Billing and Payment terms and conditions. If full payment is not received by the date due, then any license preliminarily granted shall be deemed automatically revoked and shall be void as if never granted. Further, in the event that you breach any of these terms and conditions or any of CCC's Billing and Payment terms and conditions, the license is automatically revoked and shall be void as if never granted. Use of materials as described in a revoked license, as well as any use of the materials beyond the scope of an unrevoked license, may constitute copyright infringement and Springer reserves the right to take any and all action to protect its copyright in the materials.

Copyright Notice: Disclaimer
You must include the following copyright and permission notice in connection with any reproduction of the licensed material:
"Springer book/journal title, chapter/article title, volume, year of publication, page, name(s) of author(s), (original copyright notice as given in the publication in which the material was originally published) "With permission of Springer"

In case of use of a graph or illustration, the caption of the graph or illustration must be included, as it is indicated in the original publication.

Warranties: None
Springer makes no representations or warranties with respect to the licensed material and adopts on its own behalf the limitations and disclaimers established by CCC on its behalf in its Billing and Payment terms and conditions for this licensing transaction.

Indemnity
You hereby indemnify and agree to hold harmless Springer and CCC, and their respective officers, directors, employees and agents, from and against any and all claims arising out of your use of the licensed material other than as specifically authorized pursuant to this license.

No Transfer of License
This license is personal to you and may not be sublicensed, assigned, or transferred by you without Springer's written permission.

No Amendment Except in Writing
This license may not be amended except in a writing signed by both parties (or, in the case of Springer, by CCC on Springer's behalf).

Objection to Contrary Terms
Springer hereby objects to any terms contained in any purchase order, acknowledgment, check endorsement or other writing prepared by you, which terms are inconsistent with these terms and conditions or CCC's Billing and Payment terms and conditions. These terms and conditions, together with CCC's Billing and Payment terms and conditions (which are incorporated herein), comprise the entire agreement between you and Springer (and CCC) concerning this licensing transaction. In the event of any conflict between your obligations established by these terms and conditions and those established by CCC's Billing and Payment terms and conditions, these terms and conditions shall control.

Jurisdiction
All disputes that may arise in connection with this present License, or the breach thereof, shall be settled exclusively by arbitration, to be held in the Federal Republic of Germany, in accordance with German law.

Other conditions:

V 12AUG2015

Questions? customercare@copyright.com or +1-855-239-3415 (toll free in the US) or +1-978-646-2777.

Chapter 7: Conclusions

7.1 Summary of Major Findings

Recall, the four main objectives of this dissertation are (1) to quantify dislocation density and plastic relaxation behind the shock wave front of single crystal Cu with several shock loading directions and particle velocities, (2) to determine the ability of the EAM interatomic potential and the CNA method to predict and identify defects and phase transformations behind the <100> shock wave front of single crystal Cu, (3) to investigate how FCC Cu uniaxially compresses towards the BCC structure in nanocrystalline Cu depends on particle velocity, grain size and grain orientation, and (4) to characterize unshocked nanocrystalline and shocked single crystal Cu models by virtual diffraction simulations. These objectives are addressed directly in Chapters 3 through 6 of this dissertation. The major findings of this work related to these objectives are summarized below.

In Chapter 3, to study the role of crystal orientation and particle velocity on dislocation density generation and plastic relaxation, MD simulations are performed for particle velocities from the HEL to a maximum of 1.5 km/s for different shock directions <100>, <110>, <111> and <321>. These dislocation densities are calculated through the DXA method, which provides the Burgers vector for each dislocation segment. In addition, an absorbing wall boundary condition is used to provide a sufficient time for plastic relaxation while avoiding extremely large simulation sizes. Total dislocation density generally increases with increasing particle velocity for all shock orientations. For shock in <321>, <111> and <110> directions, plastic relaxation is primarily due to a reduction in Shockley partial dislocation density. In addition, plastic anisotropy for shock loading in these orientations is less apparent at particle velocities above 1.1 km/s.

For <100> shock, plastic relaxation is restricted compared to other three shock orientations. This is partially due to the emergence of sessile stair-rod dislocations with Burgers vectors of 1/6<110> and 1/3<100>. The nucleation of 1/6<110> dislocations at lower particle velocities is mainly due to the reaction between Shockley partial dislocations and twin boundaries. On the other hand, for the particle velocities above 1.1 km/s, the nucleation of 1/3<100> dislocations is predominantly due to reaction between Shockley partial dislocations at the stacking fault intersections. Both mechanisms enhance greater dislocation densities at the Hugoniot state for shock pressures above 34 GPa compared to the other three shock orientations.

In Chapter 4, for <100> shock, the FCC lattice is uniaxially compressed towards the BCC structure behind the shock wave front, which is more favorable at higher shock pressures and temperatures. For particle velocities from the HEL to 0.9 km/s, compressed Cu quickly relaxes back into a faulted FCC structure including dislocations, stacking faults and twinning. For particle velocities greater than 0.9 km/s, the CNA indicates that regions of HCP crystal structure nucleate from uniaxially compressed Cu.

Free energy calculations confirm that for compressions corresponding to particle velocities less than 0.9 km/s, the FCC structure is the lowest energy structure. However, for larger compressions, several EAM potentials predict that the hydrostatically compressed HCP phase has a lower energy than the FCC phase, with energy difference on the meV level. Since HCP Cu is not observed experimentally during shock at high pressures, the nucleation and growth of HCP clusters behind the <100> shock wave front for particle velocities above 0.9 km/s is likely an artifact of EAM interatomic potentials.

In Chapter 5, MD simulations are performed for nanocrystalline Cu models with a range of particle velocities from 1.0 to 3.4 km/s and grain sizes from 6 to 26 nm. The grain size of

nanocrystalline Cu does not significantly influence the temperature and the pressure of shocked models at the Hugoniot state. CNA identifies BCC structure at shock pressures between 100 and 200 GPa behind the shock wave front, which depends on grain size, grain orientation and particle velocity. The computed atomic percentage of BCC structure ranges between 3.4 and 9.2% depending on grain diameter at a particle velocity of 1.5 km/s, reaches a maximum between 23.3 to 30.7% at a particle velocity of 2.4 km/s, and then decreases to approximately 0.0% at a particle velocity of 3.2 km/s. At a particle velocity of 2.4 km/s, the atomic percentage of BCC structure observed during shock increases with increasing grain size, while this trend is reversed at a particle velocity of 1.5 km/s. It is hypothesized that the behavior at 1.5 km/s is due to the difficulty of dislocation nucleation in the smallest nanocrystalline models.

Compression of FCC lattice towards the BCC structure strongly depends on grain orientation. At a particle velocity of 2.0 km/s, grains with a <100> direction closely aligned with the shock loading direction have higher tendency for compression towards the BCC structure, implying that the transformation path is tetragonal. However, at a particle velocity of 2.4 km/s, some grains which had a lower atomic percentage of BCC structure at particle velocities of 1.5 and 2.0 km/s, have a higher BCC atomic percentage. These grains have a <111> direction closely aligned with the direction of shock, implying that at higher shock velocities, the trigonal deformation path may be active despite the larger energy barrier. Finally, there are a few grains which are properly oriented for tetragonal or trigonal transformation that do not compress from the FCC lattice towards the BCC structure within the time scale of the simulation. This implies that the locations of grains as well as orientation of neighbor grains and grain boundary structure are also important factors in the prediction of structural transformations.

In Chapter 6, x-ray diffraction line profiles and SAED patterns are created for nanocrystalline Cu models containing grains with mean diameters of 5, 10 and 15 nm at 0 K temperature. To analyze the x-ray diffraction line profiles and obtain the microstrain and the mean grain diameter of the microstructure, the Williamson-Hall analysis is applied. The magnitudes of the microstrain decrease with increasing the grain diameter for models with the same number of grains. This can be justified by distortion of a smaller fraction of atoms with grain boundaries for models with larger grains. Each SAED pattern contains three rings associated with the {111}, {200} and {220} planes, and the rings in models with larger grains are thinner because of microstrain effects. This is analogous to the role of microstrain on peak broadening in the x-ray diffraction line profiles.

X-ray diffraction line profiles are created for <100> shock models of single crystal Cu at the Hugoniot state with particle velocities from 0.7 to 1.0 km/s and initial temperatures of 5, 300 and 600 K. Generally, the peak broadening in the x-ray diffraction line profiles increases with increasing particle velocity, which is partially due to the increase in dislocation density.

In summary, MD simulations are performed for single crystal and nanocrystalline Cu models subjected to shock to understand the plastic deformation mechanisms behind the shock wave front of FCC materials. Several characterization techniques in atomistic simulations are used to quantify the evolution of plastic deformation mechanisms, such as dislocation density, in shocked single crystal and nanocrystalline Cu. These quantitative analyses promote the knowledge for understanding the plastic deformations in shocked FCC materials with ns time scale and nm length scale resolution. The time scale and length scale of MD simulations are perfectly appropriate to characterize the plastic deformations in atomic level quantitatively, which is challenging in experimental studies with longer time scale and larger length scales.

Thus, MD simulations using computational characterization techniques provide valuable knowledge regarding the evolution of plastic deformations in shocked metallic materials.

7.2 Recommendations for Future Work

Chapter 3 presents the dependency of dislocation density generation and plastic relaxation in single crystal Cu during shock on particle velocity and shock orientation. MD simulations for nanocrystalline models can be performed to contribute the influence of grain size and grain orientation on dislocation density generation and plastic relaxation of shocked FCC materials. In addition, several grains with different tilt grain boundaries in the microstructure can be utilized to explore the influence of grain boundary structure and energy on dislocation density generation and plastic relaxation. Finally, MD simulations can be performed to study the influence of dopant modified grain boundaries in nanocrystalline FCC materials on dislocation density generation and plastic relaxation during shock. Nanocrystalline materials are not thermodynamically stable and their grains tend to grow; by adding some kinds of dopants, more stable alloys can be achieved. For example, MD simulations revealed that randomly distribution of Sb on Cu grain boundaries can decrease the grain growth, and make a more stable nanocrystalline model [1]. Thus, it is recommended to dope Sb on Cu grain boundaries to thermodynamically achieve more stable grains, and investigate the influence of these modified grain boundaries on dislocation density generation and plastic relaxation.

In Chapter 6, x-ray diffraction line profiles are created for <100> shock models of single crystal Cu at the Hugoniot state for several particle velocities and initial temperatures. The plastic deformation behind the <100> shock is complicated due to the emergence of several

dislocation types, twins and stacking faults as well as the influence of temperature on these defects. Thus, it is recommended to use an advanced characterization method to quantify the influence of each factor on the peak broadening of x-ray diffraction line profile. Specifically, CMWP analysis [2] can be used to fit the x-ray diffraction line profiles with theoretical ab initio functions, and obtain dislocation density and planar defect densities (stacking faults and twin boundaries).

References

[1] R. K. Rajgarhia, D. E. Spearot, and A. Saxena, "Behavior of dopant-modified interfaces in metallic nanocrystalline materials," *JOM*, vol. 62, no. 12, pp. 70–74, Dec. 2010.

[2] G. Ribárik, J. Gubicza, and T. Ungár, "Correlation between strength and microstructure of ball-milled Al–Mg alloys determined by X-ray diffraction," *Mater. Sci. Eng. A*, vol. 387–389, no. 1–2 SPEC. ISS., pp. 343–347, Dec. 2004.